Adsorption and Diffusion in Zeolites:
A Computational Study

Adsorption and Diffusion in Zeolites: A Computational Study

ACADEMISCH PROEFSCHRIFT

ter verkrijging van de graad van doctor
aan de Universiteit van Amsterdam,
op gezag van de Rector Magnificus
Prof.dr. J.J.M. Franse ten overstaan van een
door het college voor promoties ingestelde commissie,
in het openbaar te verdedigen in de Aula der Universiteit
op donderdag 12 oktober 2000 te 12.00 uur door

Thijs Joseph Henk Vlugt
geboren te Geleen

Promotoren:

- Prof.dr.ir. B. Smit, Universiteit van Amsterdam
- Prof.dr. R. Krishna, Universiteit van Amsterdam

Overige leden:

- Prof.dr.ir. A. Bliek, Universiteit van Amsterdam
- Prof.dr.ir. R.A. van Santen, Technische Universiteit Eindhoven
- Prof.dr. D. Frenkel, Universiteit van Amsterdam
- Prof.dr. F. Kapteijn, Technische Universiteit Delft
- Prof.dr. W.J. Briels, Technische Universiteit Twente
- dr. Th.L.M. Maesen, Zeolyst International (PQ Corp)

The research reported in this thesis was carried out at the Department of Chemical Engineering, Faculty of Natuurwetenschappen, Wiskunde en Informatica, University of Amsterdam (Nieuwe Achtergracht 166, 1018 WV, Amsterdam, The Netherlands) with financial support by the council for chemical sciences of the Netherlands Organization for Scientific Research (NWO-CW). A very large part of the computer resources has been generously provided by SARA (Stichting Academisch Rekencentrum Amsterdam) and EPCC (Edinburgh Parallel Computing Centre). This thesis is also available on the web: http://molsim.chem.uva.nl. The author of this thesis can be contacted by email: tampert@its.chem.uva.nl.

- This document was produced using LaTeX.
- Printed by: Ponsen & Looijen BV, Wageningen.
- Cover design by Thijs J.H. Vlugt. Inspired by “the blue book” of Frank T.J. Mackey.

Contents

1 Introduction 1

1.1 Zeolites 1

1.2 Molecular Simulations 2

1.3 Scope of this thesis 6

2 Configurational-Bias Monte Carlo methods 7

2.1 Introduction 7

2.2 Dual cut-off CBMC 9

2.3 Parallel CBMC 11

2.3.1 Introduction 11

2.3.2 Algorithm 11

2.3.3 Discussion 14

2.3.4 Results and discussion 15

2.4 Generation of trial segments for branched molecules 18

2.5 Conclusions 22

2.6 Appendix A: Model details 22

2.7 Appendix B: Proof of equation 2.21 22

2.8 Appendix C: Alternative parallel algorithm 23

2.9 Appendix D: Growth of isobutane 24

3 Recoil growth algorithm for chain molecules with continuous interactions 25

3.1 Introduction 25

3.2 Description of the algorithm 26

3.2.1 Construction of a chain 26

3.2.2 Detailed balance condition and acceptance probability 27

3.2.3 Comparison with CBMC 29

3.3 Simulations 29

3.3.1 Simulation details 29

3.3.2 Efficiency of RG compared to CBMC 31

3.4 Conclusions 34

3.5 Appendix A: Alternative algorithm to compute the weight 34

3.6 Appendix B: Parallelization 37

3.7 Appendix C: Fixed endpoints 38

4 Adsorption of alkanes in Silicalite 41

4.1 Introduction 41

4.2 Model 42

4.3 Simulation technique 43

4.4 Linear alkanes 44

4.4.1 Heats of adsorption and Henry coefficients . . . 44
4.4.2 Adsorption isotherms . . . 45
4.4.3 Discussion . . . 47
4.5 Branched alkanes . . . 56
4.6 Fitting of simulated isotherms with dual-site Langmuir model . . . 62
4.7 Conclusions . . . 62
4.8 Appendix A: Alkane model . . . 63
4.9 Appendix B: Discussion of the experimental data . . . 64
4.9.1 Heats of adsorption . . . 64
4.9.2 Henry coefficients . . . 67

5 Adsorption of mixtures of alkanes in Silicalite 69
5.1 Introduction . . . 69
5.2 Mixture Isotherms . . . 69
5.3 Consequences for Diffusion . . . 74
5.3.1 The Maxwell-Stefan theory for zeolite diffusion . . . 74
5.3.2 Diffusion of a single component in Silicalite . . . 75
5.3.3 Diffusion of binary mixtures . . . 75
5.4 Conclusions . . . 80

6 Diffusion of Isobutane in Silicalite studied by Transition Path Sampling 81
6.1 Introduction . . . 81
6.2 Transition Path Sampling . . . 82
6.2.1 Introduction . . . 82
6.2.2 Monte Carlo sampling from the distribution $F(x_0, T)$ . . . 84
6.2.3 Transition State Ensemble . . . 86
6.2.4 Integrating the equations of motion . . . 87
6.3 Simulation and model details . . . 87
6.4 Results . . . 89
6.4.1 Calculating the hopping rate . . . 89
6.4.2 Transition state ensemble . . . 91
6.5 Conclusions . . . 93
6.6 Appendix A: Calculation of a free energy profile . . . 93
6.7 Appendix B: Bitwise time-reversible multiple time-step algorithm . . . 94
6.8 Appendix C: Parallel tempering . . . 96
6.8.1 Introduction . . . 96
6.8.2 Application to transition path sampling . . . 97
6.8.3 Model system . . . 97

Bibliography 101

Summary 109

Samenvatting (Summary in Dutch) 113

Curriculum Vitae 117

Published work 119

Acknowledgements 121

Chapter 1

Introduction

1.1 Zeolites

Zeolites are microporous crystalline materials with pores that have about the same size as small molecules like water or n-hexane (pore size is usually 3-12 Å). The structure of a zeolite is based on a covalently bonded TO_4 tetrahedra in which the tetrahedral atom T is usually Silicium or Aluminum. The very famous Löwenstine rule only allows the existence of zeolites with a Silicium / Aluminum ratio of at least 1. As all corners of a tetrahedral have connections to other tetrahedra, a three dimensional pore network of channels and / or cavities is formed. Currently, these are about 100 different zeolite structures [1], several of these can be found in nature. To clarify the topology of a typical zeolite, the pore structure of the zeolite Silicalite [2] is shown in figure 1.1. This zeolite has a three dimensional network of straight and zigzag channels that cross at the intersections.

Because of their special structure, there are several applications of zeolites in industrial processes such as (selective) adsorption, catalysis and ion-exchange [3, 4]. A recent example of the use of zeolites is the catalytic upgrading of lubricating oils [5]. Noble metal loaded AEL-type silicoaluminophosphate molecular sieves selectively absorb the wax-like, long-chain normal paraffins from an oil feed-stock and hydro-convert them selectively into branched paraffins [5–7]. Catalysts based on TON- [8–11] and MTT-type [5, 8, 11–13] zeolites combine a strong affinity for long-chain, normal paraffins with a significantly higher selectivity for hydro-isomerization than for hydro-cracking [5–14]. However, the majority of zeolites that is produced worldwide is used as ion-exchanger in detergents.

A very important characteristic of zeolites is the adsorption isotherm of a given sorbate [15]. An adsorption isotherm describes the amount of adsorbed material as a function of the chemical potential at constant temperature. Using the equation of state of the sorbate one is able to convert this chemical potential to the pressure [16]. At very low pressures, the amount of sorbate will be negligible. The amount of adsorbed material also has a maximum (at high pressure) because the space for guest molecules in a zeolite is limited. A very popular equation to describe adsorption is zeolites is the Langmuir equation:

$$\frac{\theta}{\theta_{max}} = \frac{kp}{1 + kp} \tag{1.1}$$

in which θ is the loading of the zeolite, θ_{max} the maximum loading, p the pressure and k a constant. For low pressures, there is a linear relation between the pressure and the loading (Henry's law):

$$\theta = k\,\theta_{max} p = Kp \tag{1.2}$$

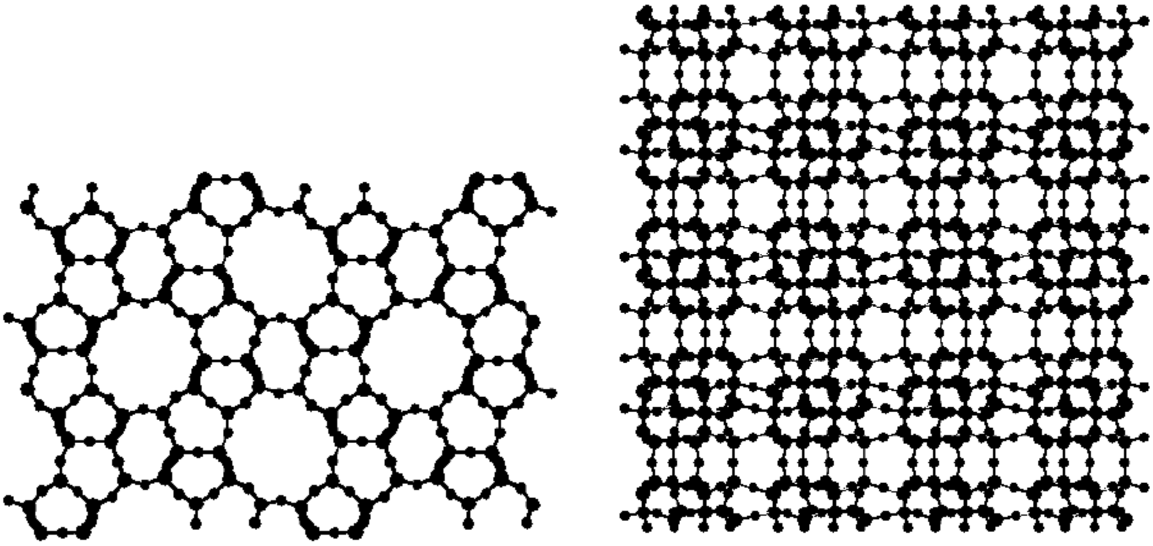

Figure 1.1: Pore structure of the zeolite Silicalite (MFI type framework). Left: projection on the x-z plane. The straight channels are perpendicular to the x-z plane, the zigzag channels are in the x-z plane. Right: projection on the x-y plane. The straight channels are from top to bottom, the zigzag channels are from left to right. The pore size of the channels is slightly larger than 5Å. The dimensions of the rectangular unit cell are 20.1Å × 19.9Å × 13.4Å; multiple unit cells are shown. See also figure 4.1 for a schematic representation of this zeolite.

in which K is the Henry coefficient. The value of K at different temperatures can often be described by the integrated form of the van't Hoff equation

$$K = K_0 \exp\left[-\Delta U/RT\right] \tag{1.3}$$

in which T is the temperature and R the gas constant. The measurement of adsorption isotherms can be quite time consuming (see, for example, ref. [17] and chapter 4 of this thesis). As the number of zeolite structures is rapidly increasing (see, for example, refs. [1, 18, 19]), to design a new zeolite-based petrochemical process one will have to perform much experimental work to find out which zeolite will be best. Therefore, it would save much time (*i.e.* money) if some experiments could be replaced by fast computer simulations. Furthermore, molecular simulations are able to simulate at conditions that are difficult to realize experimentally, for example, at high temperatures or pressures, or multicomponent systems. Another advantage of molecular simulations is that one is able to localize the positions of the molecules in the pores of a zeolite directly. This can provide insight in adsorption mechanisms, for example, the inflections in the isotherms of n-C_6, n-C_7, and i-C_4 in the zeolite Silicalite that have been measured experimentally [20, 21]. For an extensive review of computer simulations of the adsorption, diffusion, phase equilibria and reactions of hydrocarbons in zeolites the reader is referred to refs. [22, 23].

1.2 Molecular Simulations

In this thesis, we will use force field based computational methods. This means that we know exactly all interactions between the atoms of our system. Once we know these interactions, we are able to calculate a variety of static and dynamic properties like heats of adsorption, adsorption isotherms, and diffusion coefficients. In general, there are two methods to obtain a molecular force field:

1. From quantum mechanical calculations. By solving the Schrödinger equation using various approximations, we can obtain forces between different atoms and molecules. These forces can be fitted into a force field. This usually works very well for intra-molecular bonded interactions like bond-stretching, bond-bending, and torsion interactions, but less well for van der Waals interactions. Note that hydrocarbon-zeolite interactions are dominated by van der Waals interactions (see, for example, ref. [24] and chapter 4). Recently, there have been several quantum-mechanical studies of water and methanol in Sodalite [25,26] using the Car-Parrinello technique [27].

2. From experimental data. A force field can be fitted in such a way that experimental data like diffusion coefficients, heats of adsorption, or phase equilibria can be reproduced. This force field can then be used to compute other properties of other molecules.

Once we have a force field, we can calculate dynamic and static properties of our system. In general, there are two classes of methods:

- Molecular Dynamics (MD). The basic concept of Molecular Dynamics is Newton's second law, which states that the second derivative of the position is proportional to the force:

$$\frac{d^2\mathbf{x}_i}{dt^2} = \frac{\mathbf{F}_i}{m_i} \tag{1.4}$$

  in which t is the time, m_i is the mass of particle i, $\mathbf{F}_i$ is the force on particle i, and $\mathbf{x}_i$ is the position of particle i. The velocity $\mathbf{v_i}$ is the time derivative of the position:

$$\mathbf{v}_i = \frac{d\mathbf{x}_i}{dt} \tag{1.5}$$

  Except for a few trivial cases, these equations can only be solved numerically for a system of more than two particles. A popular algorithm to solve these equations of motion is the so called velocity-Verlet algorithm [28,29]:

$$\mathbf{x}_i(t+\Delta t) = \mathbf{x}_i(t) + \mathbf{v}_i(t)\,\Delta t + \frac{\mathbf{F}_i(t)}{2m_i}(\Delta t)^2 \tag{1.6}$$

$$\mathbf{v}_i(t+\Delta t) = \mathbf{v}_i(t) + \frac{\mathbf{F}_i(t+\Delta t) + \mathbf{F}_i(t)}{2m_i}\Delta t \tag{1.7}$$

  in which Δt is the time-step of the integration. Note that this algorithm is time-reversible. The average of a static property A can be calculated from the time average of A:

$$\langle A \rangle = \frac{\int dt\, A(t)}{\int dt} \tag{1.8}$$

  An important dynamic quantity is the self-diffusivity D, which can be computed by evaluating the mean-square displacement, which reads in three dimensions

$$D = \frac{1}{6}\lim_{t'\to\infty} \frac{\left\langle \left| \mathbf{x}\left(t+t'\right) - \mathbf{x}(t) \right|^2 \right\rangle}{t'} \tag{1.9}$$

  or by evaluating the integral of the velocity autocorrelation function

$$D = \frac{1}{3}\int_0^\infty dt' \left\langle \mathbf{v}(t)\cdot\mathbf{v}\left(t+t'\right)\right\rangle \tag{1.10}$$

A typical time-step for MD has to be smaller than any characteristic time in the system. For molecular systems this is in the order of $\Delta t = 10^{-15}$ s. This means that we have to integrate the equations of motion for 10^{15} steps to perform a simulation of our model for one second. In practice, we are limited to simulations of 10^{-6}s due to the limitations of modern computers. This means that using straightforward MD, we cannot obtain static and dynamic properties that have a typical time-scale of 10^{-6}s or larger. A possible way to calculate the occurrence of such infrequent events for a special class of problems is transition state theory [30].

- Monte Carlo (MC). In Monte Carlo algorithms, we do not calculate time averages but phase space averages. For example, in the canonical (NVT) ensemble, the average of a static property A is equal to

$$\langle A \rangle = \frac{\int d\mathbf{x} A(\mathbf{x}) \exp\left[-\beta U(\mathbf{x})\right]}{\int d\mathbf{x} \exp\left[-\beta U(\mathbf{x})\right]} \tag{1.11}$$

in which $\mathbf{x}$ resembles the position of all particles in the system, U is the total energy of the system and $\beta = 1/(k_B T)$, in which k_B is the Boltzmann constant. Because the integrals in equation 1.11 are integrals in many dimensions (usually at least 100) and $\exp\left[-\beta U(\mathbf{x})\right]$ is nearly always zero (*i.e.* only for a small part of $\mathbf{x}$ there is a contribution to the integral), conventional numerical integration techniques are not suited to compute $\langle A \rangle$. Therefore, the only suitable method is MC, in which the ratio of the integrals in equation 1.11 is calculated instead of the integrals themselves. In a MC simulation, we generate a sequence (length N) of coordinates $\mathbf{x_i}$, in such a way that the average of A can be calculated using

$$\langle A \rangle = \lim_{N \to \infty} \frac{\sum_{i=1}^{i=N} A(\mathbf{x}_i)}{N} \approx \frac{\sum_{i=1}^{i=N} A(\mathbf{x}_i)}{N}; \qquad N \gg 1 \tag{1.12}$$

by ensuring that points $\mathbf{x}_i$ in phase space are visited with a probability proportional to $\exp\left[-\beta U(\mathbf{x}_i)\right]$. There is an infinite number of possibilities to generate a sequence of coordinates $\mathbf{x}_i$ for a given system in such a way that this equality holds. However, to calculate $\langle A \rangle$ accurately, some methods will need an astronomical large number of states (for example, $N = 10^{500}$), while other methods need only a few states (for example, $N = 10^5$). This is the charm of MC methods, because one has the freedom to modify the algorithm to obtain an optimal efficiency. In MD simulations there usually is no such freedom.

A simple MC method is the Metropolis MC method, in which $\mathbf{k}$ is generated by adding a random displacement in the interval $[-\Delta, \Delta]$ to $\mathbf{x}_i$. When a uniform distributed random number between 0 and 1 is smaller than $\exp\left[-\beta\left(U(\mathbf{k}) - U(\mathbf{x}_i)\right)\right]$, we choose $\mathbf{x}_{i+1} = \mathbf{k}$, otherwise we choose $\mathbf{x}_{i+1} = \mathbf{x}_i$. The maximum displacement Δ can be adjusted to obtain a certain fraction of accepted trial moves (usually around 50%). One can prove that in this method the phase space density of $\mathbf{x}_i$ is proportional to $\exp\left[-\beta U(\mathbf{x}_i)\right]$ for sufficiently large i [29, 31, 32].

For long chain molecules with strong intra-molecular potentials this algorithm will not be very efficient because a displacement of a single atom will not change the conformation of the molecule very much. Furthermore, there might be high energy barriers (for example torsional barriers) which are not often crossed; this will lead to poor sampling statistics. A possible solution is the use of an algorithm that regrows a chain molecule completely or partially and thus changes the conformation of the molecule significantly. Such algorithms are discussed in chapters 2 and 3 of this thesis.

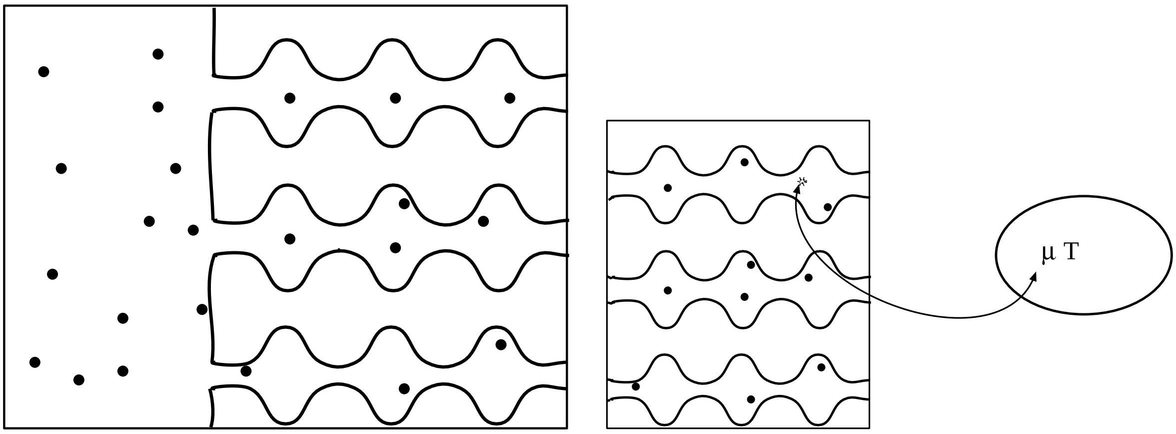

Figure 1.2: Left: Zeolite in direct contact with a gas. Right: Adsorbent in contact with a particle reservoir with a fixed temperature and chemical potential. These figures have been taken from ref. [29] with permission of the authors.

Whether we use either MD or MC depends on the property we would like to calculate. For example, consider the case of a gas that can be adsorbed in a microporous solid; one would like to calculate the Langmuir constants k and θ_{max} (see equation 1.1). In a conventional MD simulation one would have to simulate a gas in contact with the solid. There are three important disadvantages of such a simulation (see figure 1.2):

1. Usually, the gas phase is not very interesting to simulate because thermodynamic properties can usually be obtained quite easily using different methods.

2. This adsorption process is limited by the diffusion of the sorbate in the solid. One may have to simulate for a very long time to reach equilibrium.

3. As there is a gas-solid interface in the system, the size of the solid has to be chosen quite large to suppress surface effects. This will slow down the computation even more.

An alternative would be to perform a grand-canonical MC simulation, in which only the solid is simulated and not the gas phase (see figure 1.2 (right)). In this method, sorbate molecules are exchanged with an imaginary particle reservoir of which the temperature and chemical potential are known. When the number of successful exchanges with the reservoir is large enough, the chemical potential of the reservoir and the solid will be equal and the average loading of can be calculated directly. It is not difficult to insert small molecules in the zeolite. However, when an attempt is made to insert a large molecule with a random orientation in the zeolite, nearly always there will be an overlap with a zeolite atom leading to a very high energy which will result in a rejected trial move. Therefore, special techniques are needed to insert large molecules with a reasonable acceptance rate. Several of such techniques are discussed in chapters 2 and 3 of this thesis. However, when one is interested in the dynamics of such a system one will have to perform a MD simulation. For more information and other examples of molecular simulations, the reader is referred to three standard textbooks on molecular simulations [29, 32, 33]. For a review of applications of molecular simulations in chemical engineering the reader is referred to ref. [34].

1.3 Scope of this thesis

The scope of this thesis is twofold:

1. To study the adsorption and dynamic behavior of linear and branched alkane molecules in zeolites by computer simulation.
2. To develop new computational methods which make these simulations more efficient.

Configurational-Bias Monte Carlo (CBMC) is a well-known technique to perform grand-canonical MC simulations of long chain molecules efficiently. With this technique, a chain molecule is grown segment by segment in such a way that for the insertion of each segment several trial segments are generated; one of these trial segments is selected with a certain probability. In chapter 2, we will discuss several improvements of CBMC as well as a parallel implementation. It turns out that for branched alkanes the CBMC algorithm needs a subtle modification. A disadvantage of CBMC is that the growth of a chain can be stuck; *i.e.* all trial directions are unfavorable. In chapter 3, we will discuss an alternative for CBMC (Recoil Growth, RG), which suffers less from this problem. With this technique, a trial segment is selected when one is able to grow several segments ahead. For long chains and high densities RG is more than an order of magnitude more efficient than CBMC. However, it turns out that RG is less suitable for parallelization. In chapter 4, the CBMC technique in the grand-canonical ensemble is used to study the adsorption of linear and branched alkanes in the zeolite Silicalite. This adsorption can be described very well using a rather simple force field. It turns out that for this zeolite linear and branched alkane have quite different adsorption properties. Linear alkanes can occupy all channels of Silicalite while branched alkanes are preferentially adsorbed at the intersections. Therefore, it would be very interesting to investigate the competitive adsorption of alkane isomers. These simulations are presented in chapter 5, as well as an example how one can use adsorption isotherms of alkane isomers to design a membrane unit to separate these isomers. Chapter 6 deals with diffusion of branched alkanes in Silicalite. Branched alkanes in Silicalite are preferentially located at the intersections. However, sometimes a molecule can jump to another intersection. Because this jump occurs only very rarely, we cannot use conventional MD to calculate a hopping rate because the simulations would be way too long. Therefore, we use a different method (transition path sampling) for the calculation of the hopping rate.

Chapter 2

Configurational-Bias Monte Carlo methods*

2.1 Introduction

Computer simulations help us to relate the macroscopic properties of polymers to the atomic structure of these molecules. Simulations are a useful aid in the interpretation of experimental data and allow us to gain a better insight into the validity of theoretical models. In all many-body simulations, it is essential to perform an adequate sampling of the phase space of the model system. This becomes problematic for systems of long chain molecules, in particular at high densities. In fact, the slow sampling of phase space also occurs for *real* polymers - at high densities the natural ("reptation") dynamics of long polymer chains is very slow. Molecular Dynamics simulations aim to mimic the natural dynamics of a system, and suffer therefore from the same problems. However, in Monte Carlo (MC) simulations, we are not constrained to sample phase space (or actually, the configuration space) using *natural* dynamics. This is why, for dense polymer systems, Monte Carlo methods have the potential to be more efficient than Molecular Dynamics.

Many MC schemes have been proposed to sample the configuration space of both isolated polymers and moderately dense polymeric systems. Among these methods, we should distinguish between *static* Monte Carlo schemes, in which many independent polymer configurations are generated from scratch, and *dynamic* (Markov chain) MC schemes that accept or reject new chain conformations by comparing their "weight" (in the simplest cases: Boltzmann weight) with that of the old configuration. Examples of static MC schemes that can sample configurations of long polymer chains are the single [39] and double scanning [40] methods of Meirovitch and, in particular, the pruned-enriched Rosenbluth (PERM) method of Grassberger [41, 42]. Among the dynamic sampling schemes, the Configurational-Bias Monte Carlo (CBMC) technique [29,43–46] has found many applications. For example, CBMC simulations have been used for the calculation of vapor-liquid equilibria of linear and branched molecules [47–66], cyclic molecules [67,68], the simulation of adsorption of alkanes in porous structures [20,21,36,69–82], the simulation of thin films of alkanes [83, 84], and for the simulation of linear and cyclic peptides [85–87]. The basics of CBMC are summarized below. A more detailed discussion can be found in ref. [29].

In the CBMC scheme it is convenient to split the total potential energy of a trial site into two parts. The first part is the internal, bonded, intra-molecular potential $\left(u^{\text{internal}}\right)$ which is used for the generation of trial orientations. The internal potential for alkane molecules often has the

*This chapter is based on refs. [35–37]. Parts of the introduction have been taken from ref. [38].

form [88,89]

$$u^{\text{internal}}(l,\theta,\phi) = \sum u^{\text{stretch}}(l) + \sum u^{\text{bend}}(\theta) + \sum u^{\text{tors}}(\phi) \tag{2.1}$$

$$u^{\text{stretch}}(l) = \frac{1}{2}k_l[l-l_0]^2 \tag{2.2}$$

$$u^{\text{bend}}(\theta) = \frac{1}{2}k_\theta[\theta-\theta_0]^2 \tag{2.3}$$

$$u^{\text{tors}}(\phi) = C_0 + C_1\cos(\phi) + C_2\cos^2(\phi) + C_3\cos^3(\phi) \tag{2.4}$$

where $u^{\text{stretch}}(l)$ is the bond-stretching energy, $u^{\text{bend}}(\theta)$ is the bond-bending energy and $u^{\text{tors}}(\phi)$ is the torsion energy. The second part of the potential, the external potential $\left(u^{\text{ext}}\right)$, is used to bias the selection of a site from the set of trial sites. Note that this split into u^{internal} and u^{ext} is completely arbitrary and can be optimized for a particular application [90].

For a new (n) configuration, a randomly chosen molecule of length N is regrown segment by segment. If the entire molecule is being regrown then f trial sites for the first bead are placed at random positions in the simulation box [51,91]; this will turn out to be more efficient than the conventional choice $f = 1$ [29]. Note that there are also other techniques to bias the selection of the first trial segment [80,92]. The Rosenbluth weight of this segment is

$$w_1(n) = \sum_{j=1}^{j=f} \exp\left[-\beta u_{1j}^{\text{ext}}\right] \tag{2.5}$$

where $\beta = 1/(k_B T)$, and one trial site is selected with probability

$$P_{1i}^{\text{selecting}}(\mathbf{b}_i) = \frac{\exp\left[-\beta u_{1i}^{\text{ext}}\right]}{w_1(n)}. \tag{2.6}$$

For the other segments l of the molecule, k trial orientations $\mathbf{b}_i$ are generated according to the Boltzmann weight of the internal potential of that segment

$$P_{li}^{\text{generating}}(\mathbf{b}_i)\,d\mathbf{b} = \frac{\exp\left[-\beta u_{li}^{\text{internal}}\right] d\mathbf{b}}{\int \exp\left[-\beta u_{l}^{\text{internal}}\right] d\mathbf{b}} \tag{2.7}$$

See, for example, ref. [93] how to optimize k for a particular application. Out of these k trial orientations one is chosen according to the Boltzmann weight of its external potential

$$P_{li}^{\text{selecting}}(\mathbf{b}_i) = \frac{\exp\left[-\beta u_{li}^{\text{ext}}\right]}{\sum_{j=1}^{j=k}\exp\left[-\beta u_{lj}^{\text{ext}}\right]}. \tag{2.8}$$

This procedure is repeated until the entire chain of length N has been grown. The Rosenbluth weight $W(n)$ of the new configuration is defined as

$$W(n) = \frac{w_1(n)\prod_{l=2}^{l=N}\left[\sum_{j=1}^{j=k}\exp\left[-\beta u_{lj}^{\text{ext}}\right]\right]}{f \times k^{N-1}} \tag{2.9}$$

The old (o) configuration is retraced in a similar way, except that for each segment only $k-1$ ($f-1$ for the first bead) trial orientations are generated with a probability according to equation

2.7 (randomly for the first bead). The k-th (f-th) trial orientation is the old orientation. The Rosenbluth weight $W(o)$ of the old configuration is defined as

$$W(o) = \frac{w_1(o) \prod_{l=2}^{l=N} \left[\sum_{j=1}^{j=k} \exp\left[-\beta u_{lj}^{ext} \right] \right]}{f \times k^{N-1}} \tag{2.10}$$

where $w_1(o)$ is the Rosenbluth weight of the first segment of the old configuration. To satisfy detailed balance, the new configuration is accepted with probability

$$\text{acc}(o \to n) = \min\left(1, \frac{W(n)}{W(o)}\right). \tag{2.11}$$

The CBMC algorithm greatly improves the conformational sampling for molecules with articulated structure and increases the efficiency of chain insertions (required for the calculation of chemical potentials, grand-canonical, and Gibbs ensemble simulations) by several orders of magnitude. To make these simulations more efficient and to use this technique for branched molecules, several extensions are needed:

- Dual cut-off CBMC (DC-CBMC) [35]. This algorithm uses an additional bias in the selection of trial segments. It can be shown that hard-core (repulsive) interactions are more important than long-range interactions in the selection of trial segments. Therefore, one can use a second potential cut-off radius ($r_{cut}\star$) for the selection of trial segments. The second cut-off radius can be chosen quite small, for example, for a Lennard-Jones (LJ) fluid one can use $r_{cut}\star \approx \sigma$. This saves a large amount of CPU time, because short-range interactions can be calculated efficiently using a cell-list. The use of a second cut-off radius introduces an additional bias in the CBMC algorithm, which can be removed exactly in the acceptance / rejection rule.
- Parallel CBMC. With the increasing availability of parallel computers, interest in parallel MC algorithms is growing. We present a parallel CBMC algorithm on the basis of the algorithm of Esselink *et al.* [91]. This algorithm has been modified for the Gibbs ensemble by Loyens *et al.* [94].
- Generation of trial segments for a branched molecule. We will briefly discuss some of the difficulties associated with CBMC of branched molecules.

2.2 Dual cut-off CBMC

It is possible to split the external potential that is used for the selection of trial segments into two parts

$$u^{ext} = \overline{u}^{ext} + \delta u^{ext} \tag{2.12}$$

where $\overline{u}^{ext}$ is a potential that is less expensive to calculate than u^{ext}, and δu^{ext} the difference between $\overline{u}^{ext}$ and u^{ext}. A useful choice for $\overline{u}^{ext}$ is the same potential but with a shorter cut-off radius ($r_{cut}\star$)

$$u^{ext}(r) = \overline{u}^{ext}(r < r_{cut}\star) + \delta u^{ext}(r_{cut}\star \leq r < r_{cut}) \tag{2.13}$$

where $\overline{u}^{ext}(r < r_{cut}\star)$ consists only of interactions within a distance $r_{cut}\star$. Dual cut-off Configurational-Bias Monte Carlo (DC-CBMC) uses the potential $\overline{u}^{ext}(r < r_{cut}\star)$ for generation

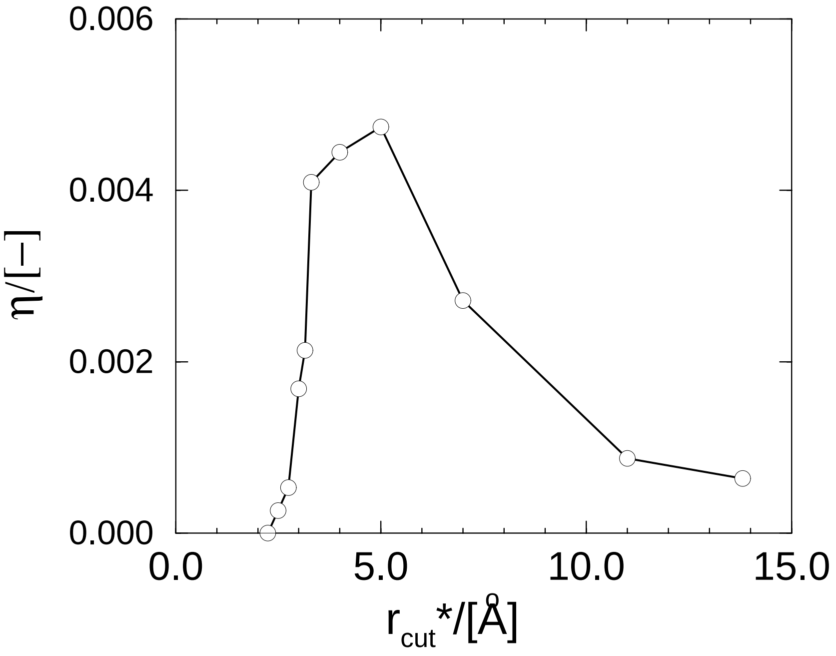

Figure 2.1: Efficiency (η) as a function of the second cut-off radius ($r_{cut}\star$). Details of the simulations can be found in appendix A.

of the chain and thus calculates the Rosenbluth weight faster than CBMC because the number of pair interactions is less. However, this would lead to an incorrect distribution if we would use the conventional acceptance rule (equation 2.11). The correct distribution is recovered by using

$$\mathrm{acc}\,(o \to n) = \min\left(1, \frac{\overline{W}(n)}{\overline{W}(o)} \exp\left[-\beta\left[\delta u^{ext}(n) - \delta u^{ext}(o)\right]\right]\right) \tag{2.14}$$

as the acceptance rule, where $\overline{W}(n)$ and $\overline{W}(o)$ are the Rosenbluth weights calculated using $\overline{u}^{ext}$. The proof of this equation can be found in ref. [35] and in appendix A. Thus, a DC-CBMC regrowth only requires the calculation of the full potential for the final configuration, and not for all of the trial orientations. Note that the division of the external energy can be done in any consistent fashion, and is typically used in conventional CBMC to account for LJ tail corrections and for Ewald corrections in charged systems.

In figure 2.1, we have plotted for a typical simulation the efficiency (η, number of accepted trial moves divided by the amount of CPU time) as a function of the second cut-off radius $r_{cut}\star$. The short-range part of the potential can be calculated efficiently using a cell-list [95]. For $r_{cut}\star = 0$, completely unbiased chains are grown, resulting in a very low efficiency. When $r_{cut}\star = r_{cut} = 13.8$Å, we obtain the original CBMC algorithm. This is not very efficient because for the selection of a trial segment, many long-range energy terms have to be calculated. The optimum value of $r_{cut}\star$ is around 5.0Å, which is slightly larger than the LJ size parameter (here: $\sigma = 3.6$Å). As in the DC-CBMC scheme the long-range energy has to be calculated only for the selected configuration and not for every trial configuration, DC-CBMC is much more efficient. For a more in-depth discussion the reader is referred to ref. [35].

2.3 Parallel CBMC

2.3.1 Introduction

Whereas previous implementations of CBMC algorithms have been limited to sequential machines; here we propose a parallel CBMC algorithm. This algorithm is a combination of two existing CBMC algorithms:

1. The Dual cut-off CBMC algorithm (DC-CBMC); see section 2.2.

2. The parallel CBMC algorithm by Esselink *et al.* [91]. In this algorithm, multiple chains are grown in each CBMC trial move to increase the acceptance probability. Because the growth of multiple chains is independent, this task can be easily distributed among processors. Important to note is that all simulations in the article of Esselink *et al.* were performed on a single workstation and not on a parallel computer, although the title of that article suggests otherwise. Therefore it remains to be shown whether this algorithm will have a good parallel performance in practice.

In this section, we will not only show that on the basis of these two algorithms we can develop an efficient parallel code, but also that a combination of these algorithms is more efficient than one would predict on the basis of each algorithm independently.

At this point we would like to address the question why one should develop a parallel MC algorithm since the most efficient way of doing MC after all is to use a different sequence of random numbers for each processor and average the results. We do not argue this may be the most efficient way, but not always the most convenient way. This is, for example, the case when a long equilibration of the system is needed.

2.3.2 Algorithm

Introduction

In general, there are several criteria to design a successful parallel algorithm:

- There should be a good load-balance, every processor should be doing roughly the same amount of work.

- The amount of communication between processors should be minimized.

There are a number of reasons why the conventional CBMC algorithm cannot be parallelized efficiently:

- The growth of a chain molecule is a sequential process by nature.

- For the selection of a new chain segment from several trial segments, a very short potential cut-off radius can be used (see section 2.2). This means that this calculation is computationally cheap and therefore it is not possible to parallelize this task efficiently on a large number of processors. Also, such a parallelization would imply that communication between processors is necessary for the growth of every segment of the chain.

To avoid these problems, Esselink *et al.* [91] have developed a CBMC algorithm in which multiple (independent) chains are grown instead of only one chain in the conventional CBMC algorithm. Out of these chains, one is selected according to its Rosenbluth weight and the other

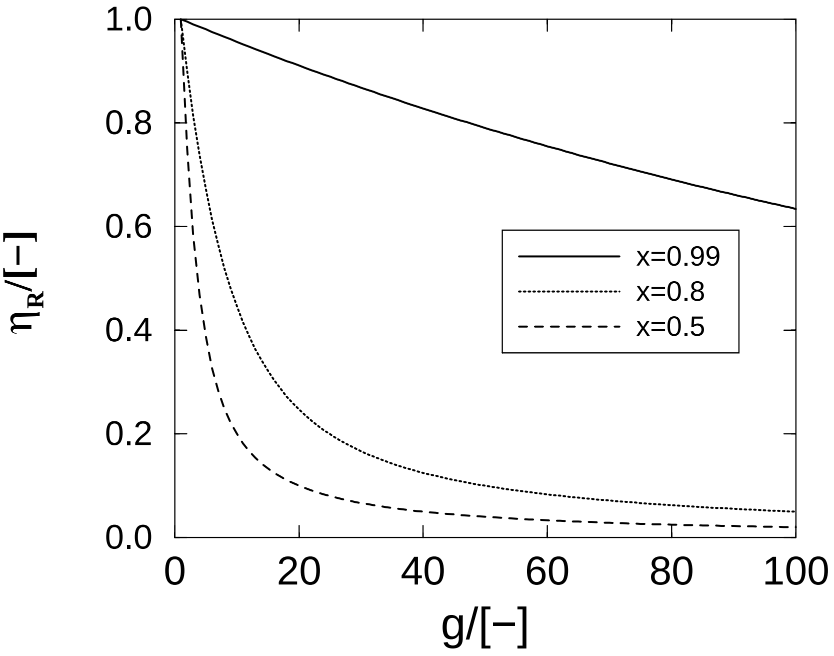

Figure 2.2: Relative efficiency (η_R) as a function of the probability of generating a chain with an overlap (x) and the number of chains grown in parallel (g) for a hard-sphere chain according to equation 2.15.

chains are thrown away. The effect of the use of multiple-chain growth is that it is more likely that one chain is grown in a favorable position, resulting in a larger fraction of accepted trial moves. This will be most effective when the fraction of accepted trial moves is low. When the fraction of accepted trial moves is high, the use of a larger number of trial chains (g) will have a small effect only.

This can be demonstrated very easily for the growth of hard-sphere chains. When the probability of generating a chain with an overlap is equal to x and the number of chains that is grown in parallel is equal to g, the relative efficiency η_R (fraction of accepted trial moves per grown chain divided by the fraction of accepted trial moves for $g = 1$) will be equal to

$$\eta_R(g, x) = \frac{1 - x^g}{(1 - x) \times g} \tag{2.15}$$

This function is plotted in figure 2.2. As can be seen, the relative efficiency will always decrease with increasing g. This decrease is less dramatic when the probability of generating a chain with an overlap is high, meaning that Monte Carlo algorithms with a high acceptance rate will have a poor parallel performance. However, when the acceptance rate is high for $g = 1$ we do not need a parallel algorithm anyway.

Algorithm

The total external energy u can be split into three parts

$$u = \overline{\overline{u}} + \delta u_1 + \delta u_2 \tag{2.16}$$

For the growth of a chain, $\overline{\overline{u}}$ is used only. δu_1 and δu_2 are correction terms. The meaning of δu_1 and δu_2 will be explained later. Note that this division is completely arbitrary.

Repeatedly, the following steps are executed:

1. Among Q processors, g new (n) chains of length N are distributed and grown using the standard CBMC algorithm. To avoid load imbalance, $\mathrm{mod}(g, Q) = 0$ must hold. For the selection of trial segments, $\overline{\overline{u}}$ is used only. This results in a Rosenbluth factor $\overline{\overline{W}}$ for each chain

$$\overline{\overline{W}} = \frac{\left[\sum_{j=1}^{j=f} \exp\left[-\beta \overline{\overline{u}}(j, 1)\right]\right]\left[\prod_{i=2}^{i=N} \sum_{j=1}^{j=k} \exp\left[-\beta \overline{\overline{u}}(j, i)\right]\right]}{f \times k^{N-1}} \tag{2.17}$$

In this equation, the number of trial segments is equal to f for the first bead and k for the next beads.

2. For each chain that has been grown, δu_1 is calculated. This is a correction factor for the Rosenbluth weight $\overline{\overline{W}}$ of each chain:

$$\overline{W} = \overline{\overline{W}} \exp\left[-\beta \delta u_1\right] \tag{2.18}$$

3. Out of the g chains, one chain (i) is selected according to

$$p_i = \frac{\overline{W}_i}{\sum_{j=1}^{j=g} \overline{W}_j} \tag{2.19}$$

4. For the selected chain, δu_2 is calculated, resulting in

$$Z(n) = \frac{\exp\left[-\beta \delta u_2\right] \sum_{j=1}^{j=g} \overline{W}_j}{g} \tag{2.20}$$

5. For the old (o) configuration, a similar procedure is used to calculate $Z(o)$. Note that the first chain of the g chains is actually the old chain that is retraced using standard CBMC retracing. The remaining $g - 1$ chains are new chains.

6. This trial move is accepted with a probability

$$\mathrm{acc}(o \to n) = \min\left(1, \frac{Z(n)}{Z(o)}\right) \tag{2.21}$$

In appendix B, it is shown that this algorithm obeys detailed balance.

Another important application of the CBMC algorithm is the calculation of the chemical potential using Widom's test particle method [29, 32, 96]. For the parallel CBMC algorithm described here it is straightforward to show that the excess chemical potential can be calculated using

$$\mu_{ex} = -\frac{\ln \langle Z^+ \rangle}{\beta} \tag{2.22}$$

in which the symbol $+$ is used to denote an additional test chain. The proof is almost identical to the proof for $g = 1$ which is given in ref. [29].

2.3.3 Discussion

There are several limiting cases of this algorithm that are worth mentioning:

1. $\overline{\overline{u}} = \delta u_1 = 0$ and $f = k = g = 1$. We obtain the standard Metropolis acceptance / rejection rule for a completely unbiased MC trial move

$$\text{acc}\left(o \to n\right) = \min\left(1, \exp\left[-\beta\left(\delta u_2\left(n\right) - \delta u_2\left(o\right)\right)\right]\right) \tag{2.23}$$

   Equation 2.22 reduces to

$$\mu_{\text{ex}} = -\frac{\ln\left\langle \exp\left[-\beta u^{+}\right]\right\rangle}{\beta} \tag{2.24}$$

   which is the usual Widom test particle method [29, 32, 96]. The symbol u^{+} represents the energy of a test particle.

2. $\delta u_1 = \delta u_2 = 0$ and $g = 1$. We obtain the standard CBMC acceptance / rejection rule

$$\text{acc}\left(o \to n\right) = \min\left(1, \frac{\overline{\overline{W}}\left(n\right)}{\overline{\overline{W}}\left(o\right)}\right) \tag{2.25}$$

   Equation 2.22 reduces to

$$\mu_{\text{ex}} = -\frac{\ln\left\langle \overline{\overline{W}}^{+}\right\rangle}{\beta} \tag{2.26}$$

   which is identical to the equation derived in ref. [29]. The symbol $\overline{\overline{W}}^{+}$ represents the Rosenbluth factor of a test chain that is grown using CBMC.

3. $\delta u_2 = 0$ and $g = 1$. We obtain the DC-CBMC acceptance / rejection rule.

4. $\delta u_1 = \delta u_2 = 0$ and $g \neq 1$. We obtain the acceptance / rejection rule for the parallel CBMC algorithm that was proposed by Esselink *et al.* [91]. Note that the algorithm of Esselink *et al.* is slightly different because for the old configuration, only one chain is grown. The Rosenbluth weights of the remaining $g - 1$ chains of the old configuration are equal to the Rosenbluth weights of the $g - 1$ chains of the new configuration that are not chosen. This scheme also obeys detailed balance. The advantage of our scheme is that it is directly portable to various ensembles like the grand-canonical or Gibbs ensemble.

It is interesting to discuss the properties of δu_1 and δu_2 when $g \neq 1$.

1. δu_1 is a correction term that is calculated for each chain individually, which means g times. As chains are divided among processors, the calculation of δu_1 for a single chain is not performed in parallel. When $\delta u_2 = 0$, the acceptance probability for a trial move will become one when $g \to \infty$.

2. The other correction term, δu_2, is calculated only for the selected chain, which means only once. This means that the calculation of δu_2 can be divided among processors. If the amount of CPU time required to calculate δu_2 is large and this calculation cannot be parallelized, load-imbalance occurs. When $\delta u_1 = 0$ and $\delta u_2 \neq 0$, the acceptance probability will not be equal to one in the limit of $g \to \infty$.

We thus can conclude that putting the energy term into δu_1 instead of δu_2 increases both the acceptance probability and the CPU time. As the efficiency (η) of a MC algorithm is usually defined by the number of accepted trial moves divided by the CPU time, the algorithm can be optimized by an intelligent division of the energy between δu_1 and δu_2. There are three parts of the total external energy which are usually put into δu_1 or δu_2:

1. LJ tail corrections. These are equal for all chains and also computationally inexpensive so they can be put safely into δu_2.

2. Fourier part of an Ewald summation [29, 32]. An Ewald summation is usually computationally expensive but it can be parallelized very easily. This term is usually not very different for all chains, so we recommend to put it into δu_2.

3. Inter-molecular interactions. These can be usually split into a short-range part and a long-range part

$$u = \overline{\overline{u}}\left(r < r_{cut^{\star}}\right) + \delta u_i \left(r_{cut^{\star}} \leq r < r_{cut}\right) \tag{2.27}$$

   in which $i = 1$ or $i = 2$. Martyna and co-workers [97] have used a similar division to distinguish two time-reversible Molecular Dynamics integration algorithms in the NVT ensemble (respectively XI-RESPA and XO-RESPA). We will therefore use the notation IN-DC-CBMC for $i = 1$ (long-range interactions are calculated for each chain) and OUT-DC-CBMC for $i = 2$ (long-range interactions are calculated for the selected chain only). Note that in RESPA algorithms a switching function is usually used to smooth the transition from short-range interactions to long-range interactions. We found that for DC-CBMC the use of a switching function does not influence the performance of the algorithm.

An important quantity is the amount of CPU time for the growth of one chain divided by the total amount of CPU time that is spend in the calculation of $\delta u_{1,2}$. When this ratio is low, one can grow multiple chains at almost no computational cost (because most time is spend on calculating $\delta u_{1,2}$). This means that for increasing g the efficiency of the algorithm will increase instead of decrease (figure 2.2). This is, for example, the case for OUT-DC-CBMC with the use of a small value for $r_{cut^{\star}}$. We therefore predict that OUT-DC-CBMC will be more efficient than IN-DC-CBMC.

When the calculation of δu_1 and δu_2 is computationally expensive and not easy to calculate in parallel, IN-DC-CBMC will fail because too many correction terms have to be calculated and OUT-DC-CBMC will fail because the calculation of δu_2 cannot be parallelized. In appendix C, we present an algorithm that may solve this problem.

2.3.4 Results and discussion

To test this parallel algorithm, we have studied a system of a single n-hexane molecule in the zeolite Silicalite. Details about the model we used can be found in appendix A. Our simulation code was written in FORTRAN77 and parallelized using MPI [98]. The following machines were used to test our parallel CBMC algorithm:

1. Sun Enterprice 3000 machine (emerald.epcc.ed.ac.uk) with 4 x 250 MHz UltraSPARC CPU's and 1 Gbyte shared memory. MPICH-1.1.1 [99] was used as communication library.

2. IBM RS/6000 SP (isis.sp.sara.nl) with 76 nodes and 512 MB distributed memory per node. MPI-F was used as a communication library.

3. Cluster (24 nodes) of PC's equipped with Intel PentiumII 350 MHz processors and 128 MB per node running Redhat Linux 5.2 [100]. LAM 6.1 [101] was used as a communication library, the options $[-O - c2c - nger]$ were used for fast communication. The PC's were connected using a 100 Mbit Full-Duplex Ethernet network and a 3Com SuperStack II Switch 3300. See ref. [102] for more information about this computer.

4. Cluster (48 nodes) of PC's equipped with AMD (K7) Athlon 500 MHz processors and 128 MB per node running Redhat Linux 6.1 [100]. LAM 6.3 [101] was used as a communication library, the options $[-O - c2c - nger]$ were used for fast communication. The PC's were connected using a 100 Mbit Full-Duplex Ethernet network and a HP ProCurve Switch 4000M. See refs. [103, 104] for more information about this computer.

In all our simulations, we have defined the efficiency of a simulation (η) as the number of accepted trial moves divided by the CPU time. It is possible to make a direct comparison between different machines/simulations using η only. The relative efficiency η_R is defined as the efficiency divided by the efficiency when the number of grown chains is equal to the number of processors, *i.e.* $g = Q$. The definition of relative efficiency of equation 2.15 is consistent with this definition.

Scaling of the number of chains (g)

In figure 2.3, we have plotted η as a function of g for various values of $r_{cut^\star}$ for simulations using 4 physical processors. All simulations in this subsection were performed on machine 1 [105]. The OUT-DC-CBMC scheme is much more efficient than the IN-DC-CBMC scheme. As expected, decreasing the second cut-off radius $r_{cut^\star}$ increases η. Furthermore, there is a striking difference between IN-DC-CBMC and OUT-DC-CBMC. For IN-DC-CBMC, the efficiency always decreases with an increasing g, resulting in a relative efficiency η_R that is smaller than 1. This is in agreement with equation 2.15. However, for OUT-DC-CBMC and $r_{cut^\star} \approx 4.0\text{Å} - 4.5\text{Å}$, there is a maximum in the efficiency, resulting in a relative efficiency that is larger than 1. The reason for this is that here much more CPU time is spent on the calculation of the long-range part of the LJ potential (δu_2) for the selected chain than in the growth of a chain molecule. This means that growing extra chains does not increase the total CPU time too much, but it does increase the fraction of accepted trial moves resulting in an overall efficiency increase. The reason that the growth of a chain molecule is computationally inexpensive is because of the small second cut-off radius, which explains why this effect only takes place at small $r_{cut^\star}$. When g becomes too large, the fraction of accepted trial moves hardly increases resulting in a decrease in efficiency. As the optimal efficiency will be at $g = 8$, running the simulation on more than 8 processors will result in an efficiency decrease.

Because of this efficiency increase instead of the expected decrease for OUT-DC-CBMC with increasing g at a small $r_{cut^\star}$, we can conclude that a combination of multiple-chain growth and the use of a second cut-off radius is more efficient that one would expect for these methods individually.

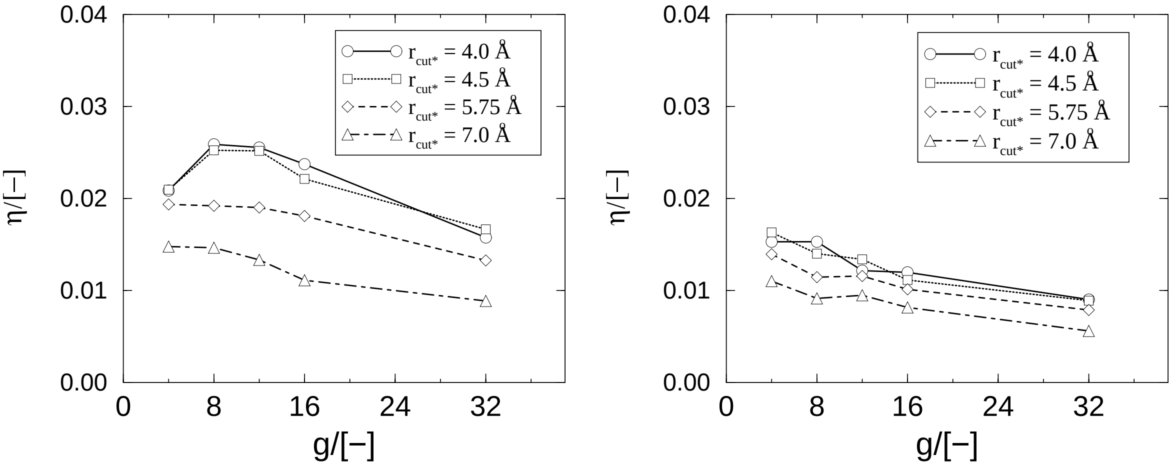

Figure 2.3: Efficiency (η) as a function of the number of chains (g) and the second cut-off radius ($r_{cut}\star$). The number of processors was equal to 4. All simulations were performed on machine 1. Left: OUT-DC-CBMC; Right: IN-DC-CBMC.

Scaling of the number of processors (Q)

To investigate the scaling of the algorithm with the number of processors, we have performed the same simulation on $Q = 1, \cdots, 4$ processors with $g = 12$ and $r_{cut}\star = 4.5$Å on machine 1 and $g = 32$ on machines 2,3,4 using $Q = 1, \cdots, 32$, see figures 2.4 and 2.5. Note that we have used $f = 15$ and $k = 10$. The reason for choosing $g = 12$ on machine 1 is that no load-imbalance will occur for $Q = 1, \cdots, 4$. We have used a large number of chains ($g = 32$) on machines 2 and 3 to test the performance of the algorithm on a large number of processors. Both IN-DC-CBMC and OUT-DC-CBMC have a linear scaling for $Q \leq 4$ on machine 1. On machines 2 and 3, the algorithm scales ideally for $Q \leq 8$. For $Q = 16$ and $Q = 32$, there is a deviation from ideal scaling due to communication overhead and load imbalance. It turns out that machine 4 is by far the fastest one, although the scaling for this machine is worse than for machine 2 for $Q = 32$. The reason is that machine 2 has the most advanced communication system between the processors.

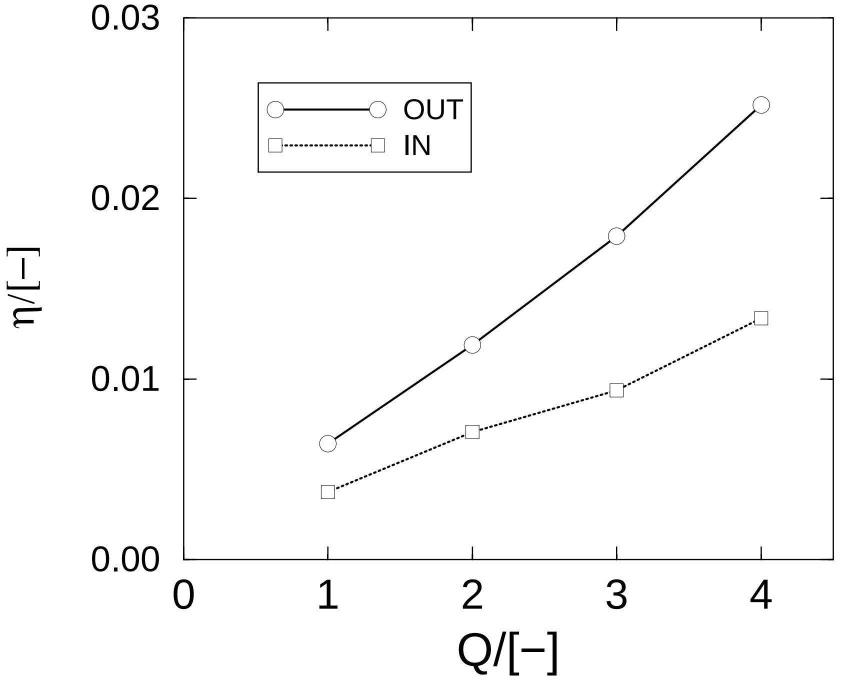

Figure 2.4: Efficiency (η) as a function of the number of processors (Q) for $r_{cut\star} = 4.5$Å, $g = 12$, $f = 15$ and $k = 10$. Simulations were performed on machine 1.

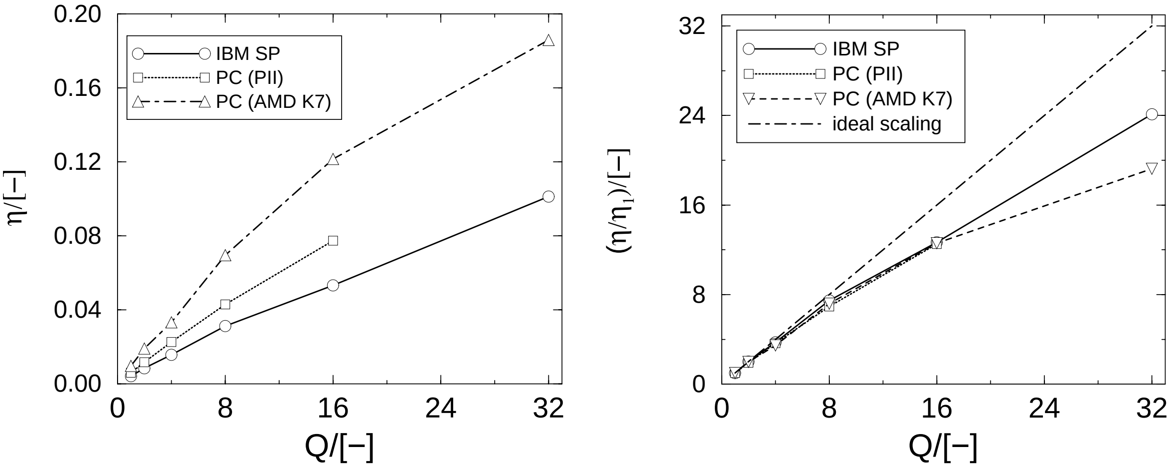

Figure 2.5: Left: Efficiency (η) as a function of the number of processors (Q) for $r_{cut\star} = 4.5$Å, $g = 32$, $f = 15$ and $k = 10$. Simulations were performed on machine 2 (IBM-SP), machine 3 (PC PII) and machine 4 (PC AMD K7). The OUT-DC-CBMC algorithm was used. Right: Same, but the efficiency is divided by the efficiency of a simulation on one processor.

2.4 Generation of trial segments for branched molecules

In this section we will discuss how to generate trial positions of a branched molecule according to the Boltzmann factor of the internal potential.

Let us consider the growth of a structure $\mathbf{x} - \mathbf{y} - (\mathbf{b}_1, \mathbf{b}_2)$. In this structure there are three

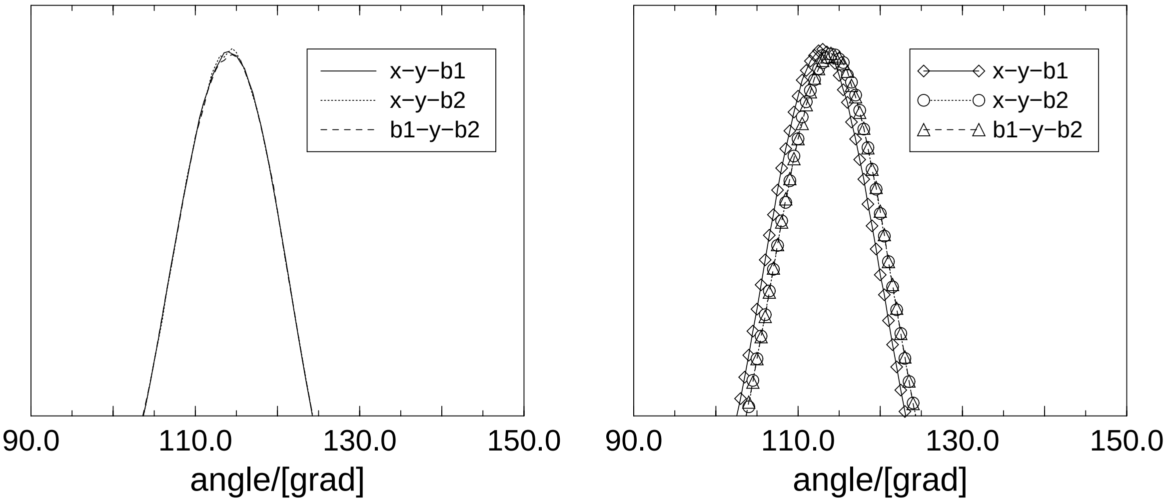

Figure 2.6: Part of the bond-angle distributions of isobutane at $T = 1000K$ ($k_\theta/k_B = 62500K$); (a) results of our algorithm and (b) the incorrect algorithm when the two beads are not inserted simultaneously ($\mathbf{b}_1$ always inserted before $\mathbf{b}_2$). Because of symmetry reasons, all angle distributions of isobutane should be equal. Note that the differences are small but significant.

bonds, $\mathbf{x} - \mathbf{y}$, $\mathbf{y} - \mathbf{b}_1$ and $\mathbf{y} - \mathbf{b}_2$ (with bond-stretching potentials according to equation 2.2) and three bond-angles $\mathbf{x} - \mathbf{y} - \mathbf{b}_1$, $\mathbf{x} - \mathbf{y} - \mathbf{b}_2$ and $\mathbf{b}_1 - \mathbf{y} - \mathbf{b}_2$ (with bond-bending potentials according to equation 2.3). This structure corresponds, for example, to a united atom model of isobutane, which is the simplest branched alkane [36].

Assume that we have already inserted the first two segments $\mathbf{x}, \mathbf{y}$ using the conventional growing schemes. We now have to generate the position of a trial set $\mathbf{B} = (\mathbf{b}_1, \mathbf{b}_2)$ where $\mathbf{b}_1$ and $\mathbf{b}_2$ are the trial positions of the two atoms that are connected to the branched atom ($\mathbf{y}$). In the CBMC scheme the probability of this set is proportional to its Boltzmann weight [29],

$$p(\mathbf{B})d\mathbf{B} \propto \exp\left[-\beta\left[u_{\text{bend}}(\mathbf{B}) + u_{\text{stretch}}(\mathbf{B})\right]\right] d\mathbf{B} \tag{2.28}$$

in which u_{bend} is the total bond-bending energy:

$$u_{\text{bend}}(\mathbf{B}) = u_{\text{bend}}(\mathbf{x}, \mathbf{y}, \mathbf{b}_1) + u_{\text{bend}}(\mathbf{x}, \mathbf{y}, \mathbf{b}_2) + u_{\text{bend}}(\mathbf{b}_1, \mathbf{y}, \mathbf{b}_2). \tag{2.29}$$

and u_{stretch} is the total bond-stretching energy

$$u_{\text{stretch}}(\mathbf{B}) = u_{\text{stretch}}(\mathbf{y}, \mathbf{b}_1) + u_{\text{stretch}}(\mathbf{y}, \mathbf{b}_2) \tag{2.30}$$

It is possible to write $d\mathbf{B}$ in spherical coordinates

$$d\mathbf{B} \propto l^2 \sin(\theta)\, dl d\theta d\phi \tag{2.31}$$

It is easy to see that due to the used harmonic bonded potentials (equations 2.2 and 2.3), the bond-lengths $l_{\mathbf{b}_1}$ and $l_{\mathbf{b}_2}$ are independent of $\theta_{\mathbf{b}_1}$, $\theta_{\mathbf{b}_2}$, $\phi_{\mathbf{b}_1}$, and $\phi_{\mathbf{b}_2}$. This means that we can generate the bond-lengths independent from the other spherical coordinates. However, due to the presence of a bond-bending potential involving $\theta_{\mathbf{b}_1,\mathbf{y},\mathbf{b}_2}$, we cannot generate $\mathbf{b}_1$ and $\mathbf{b}_2$ independent from each other; see appendix D for details. This means that CBMC schemes that do not insert all segments at a branch simultaneously generate incorrect distributions due to the presence of dependent bond-bending potentials [35, 53–55, 66], see figure 2.6.

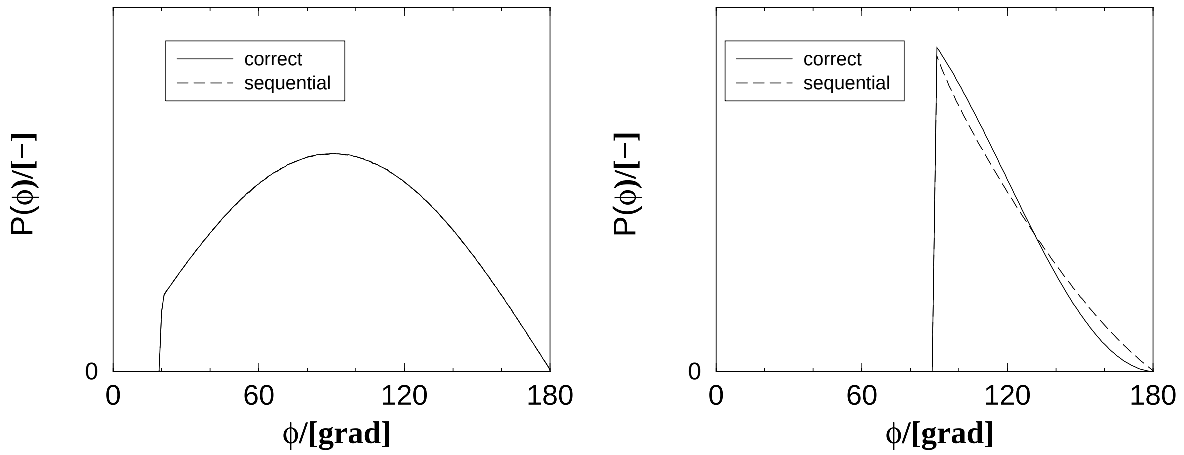

Figure 2.7: Angle distribution of a hard-sphere branch with bond-lengths a for the incorrect CBMC algorithm (sequential growth; first segment is selected at random) and the correct algorithm (beads are inserted simultaneously). Left: $a = 3$. Right: $a = 0.71$.

Let us consider now a system in which $\mathbf{x}$, $\mathbf{b_1}$ and $\mathbf{b_2}$ are hard spheres of diameter 1 and that all bond-lengths are equal to a; no other potentials are involved [106]. A straightforward analysis shows that this system does not have hard-core overlaps for $a > 1/3 \times \sqrt{3} \approx 0.577$. However, when the segments are not inserted simultaneously (we assume that a randomly selected segment is inserted first) this system will have no overlaps for $a > 1/2 \times \sqrt{2} \approx 0.707$; the reason for this is that when the first segment is placed badly, all possible trial segments for the second bead will have hard-core overlaps and thus the growth of the molecule is stuck. This means that for small a the sequential growth algorithm is not able to compute a new configurational at all, although a non-overlapping configuration does exist. In figure 2.7, we have plotted the distribution of the angle $\mathbf{x}-\mathbf{y}-\mathbf{b_1}$ for the sequential (incorrect) CBMC algorithm and the correct algorithm in which both beads are inserted simultaneously. For $a = 3$, there is no noticeable difference in the angle distributions at all. For $a = 0.71$, there is a considerable difference between the methods and for $1/3 \times \sqrt{3} < a < 1/2 \times \sqrt{2}$ the sequential growth algorithm completely fails.

A possible way to overcome these problems is to generate random vectors on a sphere simultaneously for all beads connected to a branch and to accept or to reject this configuration using the conventional acceptance / rejection rule [29, 32, 83]. A problem is that when the distribution $p(\mathbf{B})$ is small (for example, at low temperatures, a large value of the bond-bending constants or many beads that are connected to a branch) this scheme becomes computationally expensive. A possible way overcome this problem is to generate $\mathbf{b}_1, \mathbf{b}_2$ using a separate MC simulation. In such a simulation, there are two possible trial moves to change either $\phi_{\mathbf{b}_i}$ or $\theta_{\mathbf{b}_i}$ (i is chosen at random either 1 or 2) with a random displacement. The acceptance / rejection rules of these trial moves are respectively

$$\mathrm{acc}(o \to n) = \min\left(1, \exp\left[-\beta\left[u(n) - u(o)\right]\right]\right) \tag{2.32}$$

and

$$\mathrm{acc}(o \to n) = \min\left(1, \frac{\sin(\theta(n))}{\sin(\theta(o))} \exp\left[-\beta\left[u(n) - u(o)\right]\right]\right) \tag{2.33}$$

It is possible to start such a MC simulation from a previously conformation. In that case, one has to make sure that the final configuration is independent of the starting configuration. In

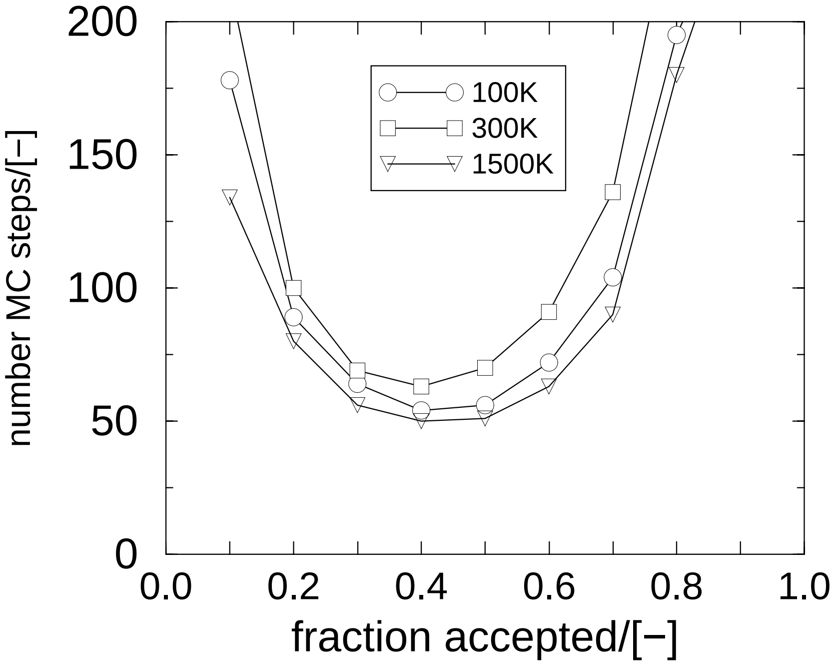

Figure 2.8: Number of MC steps to obtain independent angles for a single isobutane molecule as a function of the fraction accepted trial moves for various temperatures ($k_\theta/k_B = 62500K$). The number of steps between independent angles is calculated by evaluating the angle-angle autocorrelation function. To obtain the highest efficiency, one should adjust all maximum angle rotations to an acceptance probability of 0.4.

figure 2.8, we have plotted the number of required MC steps to obtain an independent configuration as a function of the fraction of accepted trial moves. It turns out that an acceptance rate of 40% is most efficient.

In case that more complex potentials like torsion potentials or potentials in which bond-stretching and bond-bending cannot be separated are present, it may even become impossible to generate trial segments directly according to the bonded intra-molecular potential. A way to correct for this is to generate trial segments with a distribution that is close to the correct distribution and correct for this difference afterwards (see also equation 2.14). One would like to avoid the situation in which the (computationally more expensive) external energy has to be calculated for a trial configuration with a very high internal energy, because such configurations are usually not accepted. A possible way to avoid this problem is to use CBMC on the generation of a trial segment as well [63]. In such a scheme, many (computationally inexpensive) configurations are created at random and out of these random configurations, several configurations are selected according to their Boltzmann weight of their internal bonded potential. Only for these selected configurations, the external energy has to be calculated. This will eventually lead to an acceptance rule with two different Rosenbluth factors: one for internal and one for external interactions. See refs. [63, 80] for a more detailed discussion about this subject.

2.5 Conclusions

In summary, we have briefly reviewed some of the interesting aspects of CBMC. It was found that we can efficiently use parallel computers to perform CBMC simulations and that special care has to be taken for the simulation of branched molecules.

2.6 Appendix A: Model details

To test the efficiency of the algorithm, simulations were performed for the regrowth of one n-hexane (C_6) molecule in the zeolite Silicalite-1. Such a simulation can be used to compute the heat of adsorption or Henry coefficient [29, 71, 107]. The zeolite was modeled as a rigid crystal. The number of unit cells was chosen $2 \times 2 \times 4$, resulting in a system size of $40.044\text{Å} \times 39.798\text{Å} \times 53.532\text{Å}$. For n-hexane, a united atom model was used. All alkane-alkane and alkane-zeolite inter-molecular interactions are modeled using a LJ potential with a cut-off radius of 13.8Å. In the Dual cut-off scheme, all particles including the zeolite particles were placed on a 3D grid with a grid-size at least equal to the second cut-off radius. This grid has to be recalculated only after an accepted trial move. Intra-molecular interactions include a bond-stretching potential for two bonded atoms, a bond-bending potential for three successive atoms, a torsion potential for four successive atoms and a LJ potential for atoms that are separated by more than three bonds. The number of trial orientations was chosen to be 15 for the first bead and 10 to the remaining beads. These large numbers ensure that the chain growth will not be terminated due to an overlap of all beads, which may result in load imbalance. In addition to regrowth trial moves, a very small number of particle displacement and particle rotation trial moves were used. Further details of the force field and the system can be found in sections 4.2 and 4.3.

2.7 Appendix B: Proof of equation 2.21

In this appendix, we will prove that our parallel CBMC algorithm obeys detailed balance. We start with our super-detailed balance [29] equation:

$$\sum_{b_o, b_n} \mathcal{N}(o) P_g(o \to n) \operatorname{acc}(o \to n) = \sum_{b_o, b_n} \mathcal{N}(n) P_g(n \to o) \operatorname{acc}(n \to o) \tag{2.34}$$

in which $\mathcal{N}(i)$ is the probability of finding the system in state i,

$$\mathcal{N}(i) = \exp[-\beta u(i)] \tag{2.35}$$

b_o, b_n are the sets of trial chains for the old and new configuration, $\operatorname{acc}(a \to b)$ is the acceptance probability for a trial move from a to b, and $P_g(a \to b)$ is the probability for selecting a trial move from a to b. Super-detailed balance implies that every term on the l.h.s. of equation 2.34 is equal to each term of the r.h.s. of this equation. This leads to

$$\frac{\operatorname{acc}(o \to n)}{\operatorname{acc}(n \to o)} = \frac{\exp[-\beta u(n)]}{\exp[-\beta u(o)]} \times \frac{P_g(n \to o)}{P_g(o \to n)} \tag{2.36}$$

For $P_g(o \to n)$ we can write

$$P_g(o \to n) = \frac{\exp\left[-\beta \overline{\overline{u}}(n)\right]}{\overline{\overline{W}}(n)} \times \frac{\overline{\overline{W}}(n) \exp[-\beta \delta u_1(n)]}{\sum_{i=1}^{i=g} \overline{W}_i(n)} \tag{2.37}$$

Similar for $P_g(n \to o)$

$$P_g(n \to o) = \frac{\exp\left[-\beta \overline{\overline{u}}(o)\right]}{\overline{\overline{W}}(o)} \times \frac{\overline{\overline{W}}(o)\exp\left[-\beta\delta u_1(o)\right]}{\sum_{i=1}^{i=g} \overline{W}_i(o)} \tag{2.38}$$

Combining these equations and using $u = \overline{\overline{u}} + \delta u_1 + \delta u_2$ leads to

$$\frac{\mathrm{acc}(o \to n)}{\mathrm{acc}(n \to o)} = \frac{Z(n)}{Z(o)} \tag{2.39}$$

It is straightforward to see that equation 2.21 obeys this equation.

2.8 Appendix C: Alternative parallel algorithm

When the calculation of δu_1 and δu_2 is computationally expensive and not easy to calculate in parallel, IN-DC-CBMC will fail because too many correction terms have to be calculated and OUT-DC-CBMC will fail because the calculation of δu_2 cannot be parallelized. This might be true for the simulation of polarizable molecules [108], in which an iterative scheme is used to calculated the polarization energy. In this case, the following algorithm can be used [109]:

1. Among Q processors, g new (n) chains are divided and grown using the standard CBMC algorithm. We also assume that $\mathrm{mod}(g, Q) = 0$. For the selection of trial segments, $\overline{\overline{u}}$ is used only. This results in a Rosenbluth factor $\overline{\overline{W}}$ for each chain.

2. On each processor a, one of the g/Q chains that was grown on processor a is chosen with a probability

$$p_i = \frac{\overline{\overline{W}}_i}{\sum_{j=1}^{j=g/Q} \overline{\overline{W}}_j} \tag{2.40}$$

   This is the main difference from the IN/OUT-DC-CBMC scheme in which one chain is chosen from all chains on all processors.

3. Each processor calculates δu_1 for the chain it has chosen. This leads to

$$\overline{W} = \exp\left[-\beta\delta u_1\right] \sum_{j=1}^{j=g/Q} \overline{\overline{W}}_j \tag{2.41}$$

4. One of the processors is chosen with a probability

$$p_i = \frac{\overline{W}_i}{\sum_{j=1}^{j=Q} \overline{W}_j} \tag{2.42}$$

5. For the selected chain on the selected processor, δu_2 is calculated, resulting in

$$Z(n) = \frac{\exp\left[-\beta\delta u_2\right] \sum_{j=1}^{j=Q} \overline{W}_j}{g} \tag{2.43}$$

6. For the old (o) configuration, a similar procedure is used to calculate $Z(o)$. Note that the first chain of the g chains is actually the old chain that is retraced using standard CBMC retracing. The remaining $g-1$ chains are new chains.

7. This trial move is accepted with a probability

$$\mathrm{acc}(o \to n) = \min\left(1, \frac{Z(n)}{Z(o)}\right) \tag{2.44}$$

For $Q = 1$ this algorithm will reduce to the OUT-DC-CBMC, while for $Q = g$ the algorithm reduces to the IN-DC-CBMC scheme. Note that in this algorithm the acceptance probability will be an explicit function of the number of processors, while this is not the case for OUT-DC-CBMC and IN-DC-CBMC. The proof that this algorithm obeys detailed balance is not given because it is similar to the proof in appendix B. It is quite straightforward to construct variants of this algorithm, for example, when a chain is chosen from chains that were grown on 2 processors. In general, one can construct an algorithm as follows:

1. Find a smart way to split the total external energy for a particular application.
2. Investigate if and how the calculation of the correction term δu_1 can be parallelized efficiently.
3. Construct a new algorithm by combining this information.
4. Prove that the algorithm obeys detailed balance.

2.9 Appendix D: Growth of isobutane

In this appendix, we demonstrate that for the growth of isobutane, all trial segments have to be inserted simultaneously.

In schemes in which $\mathbf{b}_1$ and $\mathbf{b}_2$ are not inserted simultaneously it is assumed that

$$\begin{aligned} p(\mathbf{b}_1) &\propto \exp[-\beta u_{\mathrm{bend}}(\mathbf{x}, \mathbf{y}, \mathbf{b}_1)] \\ p(\mathbf{b}_2 \mid \mathbf{b}_1) &\propto \exp[-\beta(u_{\mathrm{bend}}(\mathbf{x}, \mathbf{y}, \mathbf{b}_2) + u_{\mathrm{bend}}(\mathbf{b}_1, \mathbf{y}, \mathbf{b}_2))] \\ p(\mathbf{B}) &= p(\mathbf{b}_1)p(\mathbf{b}_2 \mid \mathbf{b}_1) \end{aligned} \tag{2.45}$$

It is important to note that this is assumption is only valid if

$$\begin{aligned} &\left[\int d\mathbf{b}_1 \exp\left[-\beta u_{\mathrm{bend}}(\mathbf{x}, \mathbf{y}, \mathbf{b}_1)\right]\right] \times \left[\int d\mathbf{b}_2 \exp\left[-\beta\left[u_{\mathrm{bend}}(\mathbf{x}, \mathbf{y}, \mathbf{b}_2) + u_{\mathrm{bend}}(\mathbf{b}_1, \mathbf{y}, \mathbf{b}_2)\right]\right]\right] \\ &= \left[\int d\mathbf{b}_1 \exp\left[-\beta u_{\mathrm{bend}}(\mathbf{x}, \mathbf{y}, \mathbf{b}_1)\right] \int d\mathbf{b}_2 \exp\left[-\beta\left[u_{\mathrm{bend}}(\mathbf{x}, \mathbf{y}, \mathbf{b}_2) + u_{\mathrm{bend}}(\mathbf{b}_1, \mathbf{y}, \mathbf{b}_2)\right]\right]\right] \end{aligned} \tag{2.46}$$

Because of the dependence of the second term on l.h.s. on $\mathbf{b}_1$ this equation does not hold in general.

Chapter 3

Recoil growth algorithm for chain molecules with continuous interactions*

3.1 Introduction

In the previous chapter, we have discussed several improvements of Configurational-Bias Monte Carlo (CBMC). CBMC uses the algorithm suggested by Rosenbluth and Rosenbluth [110] for generating a configuration of a chain molecule. In CBMC, a chain conformation is grown segment by segment. For each chain segment that has to be inserted, several trial segments are generated and one of these segments is selected with a probability proportional to its Boltzmann factor. This introduces a bias in the growth of the chain, which can be removed exactly by a modification of the acceptance / rejection rule; see section 2.1.

An important disadvantage of CBMC is that in the growth of the chain, only one step ahead is examined, which means that one cannot avoid that the growth of the chain may lead into a "dead-end street". To compensate for this high attrition rate in the chain construction, one is forced to use a large number of trial directions. For hard-core interactions, this leads to a broad distribution of the Rosenbluth weight and therefore low acceptance rates [111].

The recoil growth (RG) [111] algorithm first applied for polymers with hard-core interactions has been suggested as an alternative for CBMC which does not suffer from the "shortsightedness" of CBMC. The RG method is a 'look-ahead' dynamic MC scheme (in contrast to the *static* schemes of refs. [39–41]). In this algorithm, a chain is extended by one segment provided that a pathway (also called feeler) of certain length ahead of the current segment can be grown successfully. However, the feeler may fail to grow because of overlaps with other segments. In that case, the feeler can recoil up to the part of the chain that has been successfully grown.

There are two parameters that one has to tune to obtain good construction and acceptance rates: the length of the feeler and the number of trial directions. For hard-core chains, it was found that a small number of trial directions in combination with a relatively large recoil length is optimal. This is because a small number of trial directions ensures that the distribution of the Rosenbluth weight is small, which increases the acceptance probability of the chain. The consequence of a large feeler is that the accessible part of the phase space for a segment of the chain is much larger than for CBMC, which means that it is more likely that a favorable configuration will be found. Just as for CBMC, RG introduces a bias in the generation of a chain which can be removed exactly by a modification of the acceptance / rejection rule. In ref. [111], the RG algorithm was tested for self-avoiding walks on a lattice and its efficiency was compared

*This chapter is based on ref. [38]. Appendix C is unpublished.

with CBMC. It was found that for low densities (*e.g.* 30% occupancy of the lattice), CBMC performs better than RG for both short and long polymer chains. For higher densities and chain lengths longer than 20 segments, RG is an order of magnitude more efficient than CBMC.

The purpose of this study is to extend the RG algorithm to off-lattice chain molecules with continuous interactions. Although the algorithm is inspired by the one for hard-core interactions, there are several important differences in the construction of the algorithm.

The structure of this chapter is as follows. In section 3.2 the RG algorithm for the case of continuous interactions is described, while in section 3.2.3 it is shown that RG can only become equivalent to CBMC for hard-core potentials. Section 3.3.2 contains a study of the efficiency compared to CBMC and suggestions for the optimization of the method. In appendix A, we present an alternative (but less efficient) algorithm to compute the Rosenbluth weight of a chain. In appendix B, we show that there is little point in parallelizing the RG scheme using a "multiple chain" algorithm as described in section 2.3. In appendix C, we show how to incorporate RG into a fixed endpoint scheme. In such a scheme, part of a chain is regrown between fixed endpoints.

3.2 Description of the algorithm

The RG algorithm for hard-core chains is described in detail in ref. [111]. Here we discuss extensions of this algorithm for continuous potentials. In what follows we describe the RG scheme for canonical MC in which M chains of length N are sampled. It is straightforward to extend this algorithm to other ensembles [29, 32].

3.2.1 Construction of a chain

The central step in RG is the selection of a specific polymer trial conformation from an entire "tree" of possible conformations. The essential difference between the "continuous-potential" RG method and the earlier schemes is that the selection of the trial conformation involves *two* stochastic steps: the first is the selection of a subset of "open" branches on the tree, the second is the selection of the trial conformation among the open branches. The crucial new concept in RG is that trial directions can be either open or closed. A trial direction that is closed will never be chosen as a part of the chain. For hard-core potentials, a trial direction is closed if it leads to a configuration that has at least one hard-core overlap - otherwise it is open. Therefore, the selection of the open trial directions is *deterministic* rather than *stochastic*. In contrast, for continuous potentials, we use a stochastic rule to decide whether a trial direction is open or closed. The probability p_i that direction i is open depends on its energy u_i, hence $p_i = p_i(u_i)$. It is important to note that, in principle, this stochastic rule is quite arbitrary, the only restriction is $0 < p_i \leq 1$ (for hard-core potentials: $0 \leq p_i \leq 1$). However, it is useful to apply the following restrictions [112]

$$\begin{aligned} \lim_{u_i \to \infty} p_i(u_i) &= 0 \\ \lim_{u_i \to -\infty} p_i(u_i) &= 1 \end{aligned} \tag{3.1}$$

These restrictions ensure that very favorable configurations will be open and very unfavorable configurations will be closed. An obvious choice that obeys these restrictions is the standard Metropolis acceptance / rejection rule [29, 31, 32]

$$p_i(u_i) = \min(1, \exp[-\beta u_i]) \tag{3.2}$$

in which $\beta = 1/(k_B T)$. For hard-core potentials, p_{open} is either equal to 0 (at least one overlap) or 1 (no overlaps). Once we have determined the set of open trial directions, the RG algorithm for a chain with continuous interactions becomes almost identical to that for a hard-core chain:

1. To start, the first segment of a chain is placed at a random position in the system. If the first position is open, we continue with the next step. Otherwise, the chain is discarded.

2. A direction is assigned randomly to a segment i ($i > 1$). If this direction leads to overlap with another segment in the system, another direction is tried, up to a maximum of k trial directions. In principle, k can vary with i. In fact, it can even be a stochastic variable.

3. If an open direction is found, a new segment is added and the number of the directions for segment i that have not yet been explored is recorded. If all directions are blocked the chain retracts by one step to segment $i-1$, and the unused directions are explored. The chain is allowed to recoil up to length $(l_{max} - l + 1)$ where l_{max} is the maximum length that the chain has attained in its growth history, and l is the recoil length, which is a fixed simulation parameter. When a chain is not allowed to recoil the entire chain is discarded.

4. The previous steps are repeated until the complete chain has been grown. After the successful construction of a chain, the weight of the new chain, $W(n)$, is computed. This weight will be needed in step 6 to determine whether or not the new conformation will be accepted. The computation of W will be discussed in the next section.

5. For the old chain, on every segment of the old chain $k-1$ feelers of length l are grown and the number of feelers that is grown successfully is recorded. Using this information, one can compute the weight of the old configuration, $W(o)$.

6. The new configuration is accepted with a probability

$$\text{acc}(o \to n) = \min\left(1, \frac{W(n)}{W(o)}\right) \tag{3.3}$$

In the next sections, we derive the form for $W(n)$ and $W(o)$ that is required to obey detailed balance.

3.2.2 Detailed balance condition and acceptance probability

In a Markov-chain Monte Carlo scheme, we need to ensure that different points in configuration space are visited with a frequency proportional to their Boltzmann weight. This is usually achieved by imposing the detailed balance condition

$$\mathcal{N}(o)\, P(o \to n) = \mathcal{N}(n)\, P(n \to o) \tag{3.4}$$

where $\mathcal{N}(i)$ is the Boltzmann weight of state i,

$$\mathcal{N}(i) = \exp\left[-\beta u(i)\right] \tag{3.5}$$

and $P(o \to n)$ is the transition probability from state o (old configuration) to state n (new configuration).

In the RG algorithm, the transition probability includes the construction of a particular tree of trial segments for both the new and the original state, the stochastic choice of the subset of "open" segments in both trees, the selection of a particular configuration among the "branches"

of the “new” tree, and finally the probability of accepting the new configuration. The transition probability from the old to the new state is given by:

$$P(o \to n) = \sum_{t_o, t_n, O_o, O_n} P_g(t_n) P_g(O_n \mid t_n) P_g(rw_n \mid t_n, O_n) \times \\ P_g(t_o \mid rw_o) P_g(O_o \mid t_o, rw_o) \, \mathrm{acc}(o \to n) \quad (3.6)$$

where $P_g(t_n)$ is the probability of generating the new tree t_n - in what follows, we shall consider the case that this probability is uniform [113]. $P_g(O_n \mid t_n)$ is the probability of selecting a particular set of open/closed directions (O_n) on the new tree t_n. $P(rw_n \mid t_n, O_n)$ is the probability of putting a chain on the new tree t_n with a set of open/closed directions O_n. This can be interpreted as a random walk (rw) on the tree t_n in the direction of the chain. Therefore, this factor is equal to

$$P(rw_n \mid t_n, O_n) = \frac{1}{\prod_{i=1}^{i=N} m_i} \quad (3.7)$$

in which m_i is the number of successfully grown feelers at position i in the chain. m_i is always larger than zero, because if it were not, the trial move would not have resulted in *any* new configuration, and it would have been rejected. The next two terms are related to the old configuration: $P_g(t_o \mid rw_o)$ is the probability of generating a tree around the old configuration (*i.e.* the old configuration is included in the tree, the other configurations are generated) and $P_g(O_o \mid t_o, rw_o)$ is the probability of selecting a particular set of open/closed directions on this tree - but the old configuration of the chain is always “open”. Finally, the term $\mathrm{acc}(o \to n)$ is the probability that the transition from o to n is accepted. The transition probability from the new (n) to the old (o) state is written as equation 3.6 by exchanging o and n:

$$P(n \to o) = \sum_{t_o, t_n, O_o, O_n} P_g(t_o) P_g(O_o \mid t_o) P_g(rw_o \mid t_o, O_o) \times \\ P_g(t_n \mid rw_n) P_g(O_n \mid t_n, rw_n) \, \mathrm{acc}(n \to o) \quad (3.8)$$

Detailed balance is satisfied by imposing the stronger condition of super-detailed balance [29], which means that we obey detailed balance for all possible sets of trees and open/closed directions of both the new and old configuration ($[t_o, t_n, O_o, O_n]$). Many factors in $P_g(O_n \mid t_n, rw_n)$ that are found in the transition probability from the new (n) to the old (o) state cancel with the factors of $P_g(O_n \mid t_n)$ which are in the expression for the transition probability from the old (o) to the new (n) state. The only remaining term is the probability of generating open directions along the backbone of the tree. Therefore, the correct acceptance/rejection rule is given by

$$\mathrm{acc}(o \to n) = \min\left(1, \frac{W(n)}{W(o)}\right) \quad (3.9)$$

in which $W(n)$ equals

$$W(n) = \frac{\exp[-\beta u(n)] \prod_{i=1}^{i=N} \frac{m_i(n)}{p_i(n)}}{f \times k^{N-1}} \quad (3.10)$$

In this equation, f is the number of trial positions for the first segment, which is equal to 1 when the first segment of the chain is placed at a random position in the system. Note that the term $f \times k^{N-1}$ is present in both the numerator and denominator of equation 3.9 and is therefore

irrelevant. We include this term to emphasize the similarity of W with the Rosenbluth weight (equation 2.9). We obtain the expression for $W(o)$, by exchanging n and o:

$$W(o) = \frac{\exp\left[-\beta u(o)\right] \prod_{i=1}^{i=N} \frac{m_i(o)}{p_i(o)}}{f \times k^{N-1}} \tag{3.11}$$

If we choose equation 3.2 as our stochastic rule, there is complete cancellation of Boltzmann factors associated with the selected trial segments (i) as long as $u_i \geq 0$. For hard-core interactions $p_i = 1$, in which case the algorithm reduces to the RG algorithm for hard-core potentials [111].

For the simulation of branched chain molecules, there will be an additional term in equation 3.6 for the probability to select a random growth path on the branched molecule. As this probability is uniform, this does not influence the final expression (equation 3.9). For the simulation of branched molecules with bonded intra-molecular interactions special techniques like the Coupled-Decoupled CBMC method by Martin and Siepmann [63] may be required; see section 2.4.

An alternative scheme to compute the weights $W(n)$ and $W(o)$ can be found in appendix A. As this scheme is more complex and less efficient than the scheme presented above, we will not discuss it in the main text of this chapter.

3.2.3 Comparison with CBMC

It is instructive to compare RG with CBMC for when the recoil length l is equal to 1. In ref. [111] it was explained that, for hard-core potentials, RG and CBMC become identical when $l = 1$. Below we show that this is not the case continuous potentials. In other words, RG is not simply a generalization of CBMC. In CBMC we retain *all* possible trial directions and then select a particular direction i with a probability proportional to its Boltzmann weight $b_i = \exp\left[-\beta u_i\right]$. For models with continuous interactions, $b_i > 0$ (even though it may be very small). Hence, in a naive implementation of the CBMC scheme, the growth of a trial configuration will be completed, no matter how small b_i (see, however, ref. [114]). Of course, in the acceptance step, conformations with a very low weight will most likely be rejected. In contrast, in the RG scheme, unlikely configurations are weeded out at an early stage because, most likely, they will be "closed". One might think that RG would become similar to CBMC if we do not allow trial segments to be closed (*i.e.* if $p_i(u_i)$ is always equal to one). However, if we do that, *all* generated configurations are equally likely to be selected, irrespective of their Boltzmann weight. Clearly, that would be much worse than CBMC (unless $k = 1$, in which case both schemes reduce to the worst possible algorithm: *i.e.* random insertion). Otherwise, RG is only equivalent to CBMC in the case that $l = 1$ provided that all configurations that have a non-zero Boltzmann weight, do in fact have the *same* Boltzmann weight. Clearly, this condition is fulfilled for hard-core potentials. But, in general, RG and CBMC are based on different stochastic rules to generate trial configurations.

3.3 Simulations

3.3.1 Simulation details

To study the efficiency of the continuous-potential RG method, we have performed NVT-Monte Carlo simulations of M linear chains (length N) with truncated Lennard-Jones interactions between the non-bonded segments. In reduced units (well depth $\epsilon = 1$, Lennard-Jones diameter

$\sigma = 1$), the truncated LJ potential has the following form:

$$u(r) = \begin{cases} 4\left[\left(\frac{1}{r}\right)^{12} - \left(\frac{1}{r}\right)^{6}\right] & r \le r_{cut} \\ 0 & r > r_{cut} \end{cases} \quad (3.12)$$

We have used $r_{cut} = 2.5$. The bond-length between two successive segments was chosen to be 1.0. Three successive segments of a molecule have a constant bond-angle of 2.0 rad. Intra-molecular non-bonded interactions were taken into account for segments that are separated by more than two bonds.

To enhance the efficiency of both the CBMC and the RG scheme, we have divided the inter-molecular potential energy into short-range and long-range parts

$$u(r) = \overline{u}(r < r_{cut^\star}) + \delta u(r_{cut^\star} \le r < r_{cut}) \quad (3.13)$$

in which $r_{cut^\star}$ is a second cut-off radius. As is shown in section 2.2, the repulsive part of the potential is most important for the generation of a chain:

- For CBMC, we generate chain segments only with the short-range part of the potential and correct for the bias afterwards (see section 2.2).

- For RG, we only use the short-range part of the potential to decide whether a segment is open or closed. In this study, we have used

$$p_{open} = \min\left(1, \exp\left[-\beta\left(\overline{u}_{inter}(r < r_{cut^\star}) + u_{intra}\right)\right]\right), \quad (3.14)$$

  where u_{intra} is the intra-molecular energy [115]. In principle, one could optimize this stochastic rule.

Since the generation of a chain only uses the short-range part of the potential, we can make a linked cell-list to calculate the potential efficiently. Such a cell-list only has to be updated after an accepted trial move. As the number of interactions within the short-range part of the potential is usually quite small, we can calculate the energy of a trial position very fast, see section 2.2. One consequence of this trick is that most of the CPU time will be spent in calculating the long-range part of the potential energy, as the construction of a chain is very fast. As a consequence, the overall efficiency of the simulation does not depend strongly on the choice of the simulation parameters (f, k, l). This makes it difficult (but also less relevant) to find (or predict) the optimal values for (f, k, l) [93].

When the first segment of a new chain is placed at an unfavorable position, it is not very likely that this trial move will be accepted. Therefore, we use CBMC in the selection of a position for the first segment [91], for which we use f trial positions. One of these positions is selected with a probability proportional to its Boltzmann factor. For the old configuration, $f - 1$ trial positions are generated (the f-th is the position of the first segment itself). To obey detailed balance, one has to multiply the Rosenbluth weight of the new and old configuration (equations 3.10 and 3.15) with the sum of the f Boltzmann factors; see also refs. [63, 80, 91]. The value of f can be chosen quite large for CBMC, for example, Martin *et al.* use $f = 10$ [63] and Mackie *et al.* have used $f = 32$ to $f = 128$ [51]. RG is less sensitive to the value of f because, if the first segment is placed at a position with a very unfavorable energy, the chain growth will be terminated immediately.

3.3.2 Efficiency of RG compared to CBMC

To test the efficiency of our algorithm, we have simulated the following systems at $T = 5.0$:

1. $N = 10$, $\rho = 0.4$, $M = 40$
2. $N = 10$, $\rho = 0.2$, $M = 20$
3. $N = 20$, $\rho = 0.4$, $M = 20$
4. $N = 20$, $\rho = 0.2$, $M = 10$
5. $N = 40$, $\rho = 0.4$, $M = 10$
6. $N = 40$, $\rho = 0.2$, $M = 5$

Note that ρ is the segment density. In all our simulations, we have used $r_{cut}\star = 1.5$. The length of our cubic simulation box was 10.0. We have simulated all systems using CBMC ($f = 5, 10$, $k = 5, 10, 15$) and RG ($f = 5$, $k = 1, 2, 3, 4, 5$, $l = 1, 2, 3, 4, 5$). Note that, in principle, k itself can be a stochastic variable [111] - but here we have kept it fixed. We have performed two different trial moves:

- Displacement of a chain. A randomly chosen chain is given a random displacement. The maximum displacement is adjusted such that 50% of the trial moves are accepted.
- Regrowth of a chain. A randomly chosen chain is regrown at a random position using either CBMC or RG.

In every MC trial move consists of either a trial regrowth or a trial displacement (both selected with equal probability). The amount of CPU time that is spent in the regrowth trial move is monitored during the simulation. A total simulation consists of 10^5 cycles, *i.e.* 10^5 trial moves per chain.

First of all, we have checked if the implementation of RG and CBMC is correct. We have found excellent agreement in average energies, distribution of the radius of gyration of a chain and also the radial distribution function between RG and CBMC for various simulation parameters. In general, there are several ways to define the efficiency of a simulation:

1. Number of accepted trial moves divided by the CPU time (η_1). This definition is often used, but it does not say anything about the effectiveness of accepted trial moves in changing the molecular configuration. For example, if we swap between two different configurations the number of accepted trial moves can be large while the system itself is hardly changed.
2. Decay of an autocorrelation function that measures the rate of change of molecular conformations (η_2). For example, we can measure the autocorrelation function of the angle between the end-to-end vector of a chain with an arbitrary but constant vector (for example, the z-axis) as a function of the CPU time. The faster the decay of this function, the faster a new independent configuration is generated. The efficiency η_2 is defined as the initial decay of this autocorrelation function.

The second definition is generally preferred, because this one contains not only information about the CPU requirements of the algorithm, but also information about its effectiveness in sampling configuration space.

Table 3.1: Optimal simulation parameters and efficiencies (arbitrary units) by both definitions (η_1, η_2) for both RG ($f = 5$) and CBMC. The last two columns are the efficiency ratios for RG and CBMC according to different definitions (η_1, η_2).

				CBMC			RG			(RG / CBMC)$_1$	(RG / CBMC)$_2$
	N	ρ	M	f,k	η_1	η_2	k,l	η_1	η_2	-	-
1	10	0.4	40	10,10	5.9	0.071	3,4	22.4	0.27	3.8	3.8
2	10	0.2	20	10,5	63.2	1.54	2,2	102.5	2.5	1.6	1.7
3	20	0.4	20	10,15	0.58	0.013	3,5	5.0	0.12	8.6	8.4
4	20	0.2	10	10,10	16.2	0.748	2,2	35.7	1.8	2.2	2.4
5	40	0.4	10	10,15	0.031	0.0017	3,5	0.81	0.039	26	23
6	40	0.2	5	10,10	3.6	0.35	2,3	9.83	1.02	2.7	2.9

In table 3.1, we have summarized the efficiency by both definitions for our six model systems, with their optimal simulation parameter sets for both CBMC and RG. It is found that the ratios of efficiencies of CBMC compared to RG are equal for both definitions. This means that an accepted CBMC move is as effective in changing the molecular configuration of the system as an accepted RG trial move. This is different from lattice simulations of RG and CBMC [111], the reason for this is unclear to us. For short chains and low density the improvement of RG over CBMC is only marginal. However, for high densities and long chain lengths, RG is an order of magnitude more efficient than CBMC. For both schemes, the efficiency of the MC scheme decreases quite rapidly at high densities and for long chain lengths. However, using RG we can clearly extend the density and chain-length regime for which MC techniques based on chain regrowth are feasible.

In figure 3.1, we have plotted the efficiency of the RG scheme as a function of the number of trial directions (k) for various values of the recoil length (l). As is to be expected, the efficiency decreases quite rapidly with increasing chain length and density. The figure shows that, once k, the number of trial directions, is larger than one, more efficiency is gained by increasing the value of the recoil length l than by increasing k. However, at higher densities, it is important to optimize k. Of course, for $k = 1$, the efficiency is independent of the recoil length.

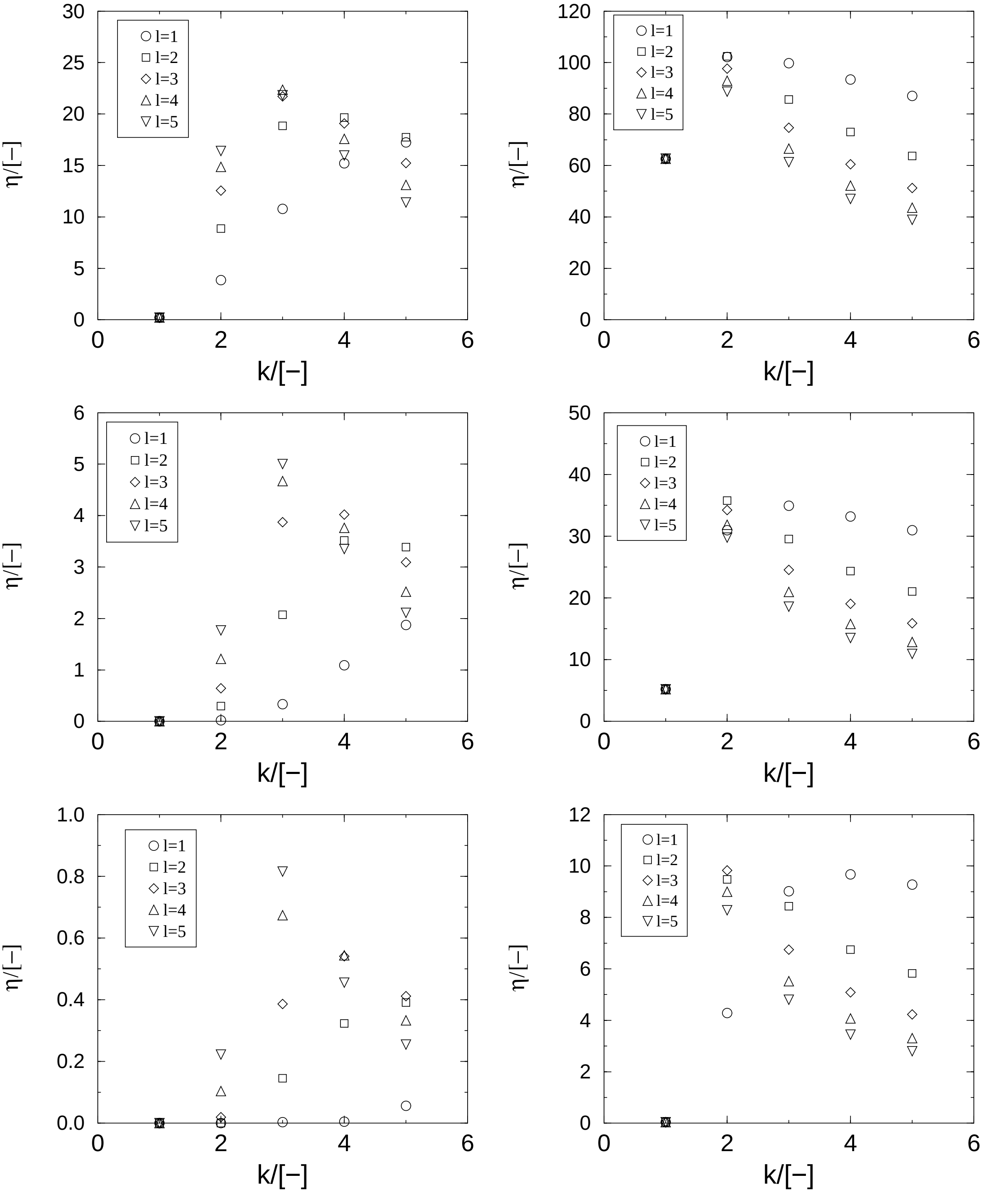

Figure 3.1: Efficiency (arbitrary units, η_1) as a function of the number of trial directions (k) for a given recoil length (l) for the six systems described in section 3.3.2 (Left: reduced density $\rho = 0.4$, Right: $\rho = 0.2$. Top-to-bottom: chain-lengths $N = 10$, $N = 20$, $N = 40$). $f = 5$.

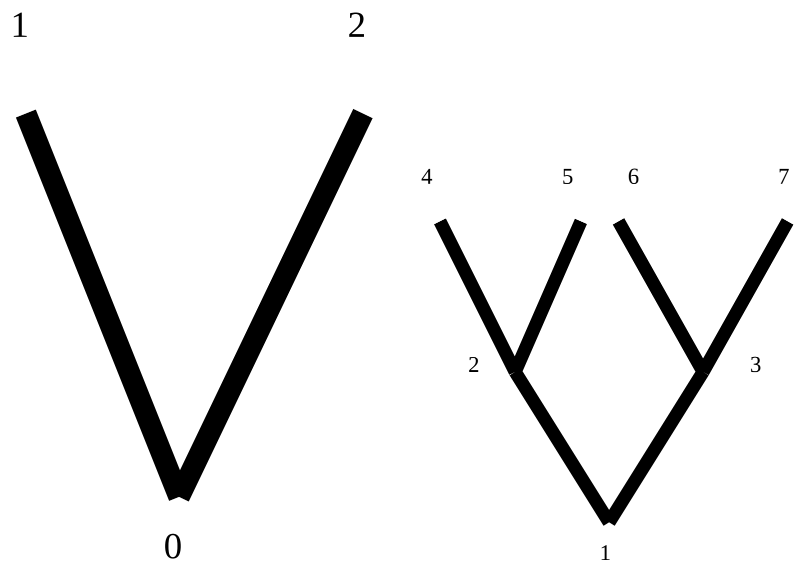

Figure 3.2: Schematic representation of some simple trees. Left: $l = 1$, $k = 2$, and $N = 2$, Right: $l = k = 2$ and $N = 3$.

3.4 Conclusions

In summary, we have extended the recoil growth scheme for systems with continuous potentials. We find that in a NVT simulation RG is much more efficient than CBMC for long chains and high densities. However, in appendix B we have shown that RG is less suitable for parallelization using the parallel algorithm of section 2.3. We found that the standard Metropolis acceptance / rejection rule is a reasonable stochastic rule when a Lennard-Jones potential is used.

3.5 Appendix A: Alternative algorithm to compute the weight

Instead of the method described in section 3.2.2, it is also possible to calculate the probability that a certain path on the tree t is followed explicitly, without having to use terms that represent the probability of generating a set of open/closed directions ($P_g(O_n \mid t_n)$, $P_g(O_o \mid t_o, rw_o)$). This means that O_o and O_n do not appear in the super-detailed balance expression (equations 3.6 and 3.8). When the probability to follow a path on the tree is equal to Ψ, to obey detailed balance and to use equation 3.9 as acceptance/rejection rule we have to redefine the weight $W(n)$ as

$$W(n) = \frac{\exp[-\beta u(n)]}{\Psi(n) \times f \times k^{N-1}} \tag{3.15}$$

To obtain the correct expression for $W(o)$, we have to replace n with o:

$$W(o) = \frac{\exp[-\beta u(o)]}{\Psi(o) \times f \times k^{N-1}} \tag{3.16}$$

To calculate Ψ, we have to extend all feelers up to the recoil length l and calculate the probabilities that each of these trial segments is open.

It is instructive to discuss the situation $l = 1$ and $N = 2$. This system is schematically drawn in figure 3.2 (left). The probability that the first segment is open is equal to p_0. For the second

Table 3.2: Recursive FORTRAN90 function (F) to compute the probability to select direction 1 from k directions (see equations 3.17 and 3.19). The probability that direction i is open is equal to P(i). This function should be called with N=k and Norm=1.

```
Recursive Double Precision Function F(P,N,Norm) Result(Res)
Implicit None

Integer N,Norm
Double Precision P(*)

If(N.Eq.1) Then
   Res = P(1)/Dble(Norm)
Else
   Res = P(N)*F(P,N-1,Norm+1)
   Res = Res + (1.0d0-P(N))*F(P,N-1,Norm)
Endif

Return
End Function F
```

segment, the probability that we select trial segment 1 is equal to

$$Q = \frac{p_1 p_2}{2} + \frac{p_1 (1 - p_2)}{1}, \tag{3.17}$$

in which p_i is the probability that segment i is open. The probability of generating the whole chain (segments $0, 1$) then equals

$$\Psi = p_0 Q \tag{3.18}$$

When the number of trial segments for the second segment is equal to k, the number of terms in this equation will be equal to 2^{k-1}. For example, for $k = 3$ the probability to select trial segment 1 is equal to

$$Q = \frac{p_1 p_2 p_3}{3} + \frac{p_1 p_2 (1 - p_3)}{2} + \frac{p_1 (1 - p_2) p_3}{2} + \frac{p_1 (1 - p_2)(1 - p_3)}{1} \tag{3.19}$$

For arbitrary k, it is possible to compute this function recursively, see table 3.2. Note that for hard-core potentials, p_i is either equal to 0 or 1. This means that for arbitrary k, all terms except one in equation 3.19 will be equal to zero. Therefore this equation will reduce to

$$Q = \frac{1}{m} \tag{3.20}$$

in which m is the number of open directions including direction 1. It is straightforward to see that in this case the algorithm reduces to the standard RG algorithm of hard-core potentials [111].

Let us now consider the case that we have to calculate the probability of generating a chain of length $N = 3$. This is only different from the previous case in the way we calculate the probabilities that parts of the tree are open. For example, consider a segment (1) with children 2 and 3. Segment 2 has children 4 and 5 and segment 3 has children 6 and 7. This situation is drawn schematically in figure 3.2 (right) and it corresponds to $l = k = 2$. Let us again use p_i for

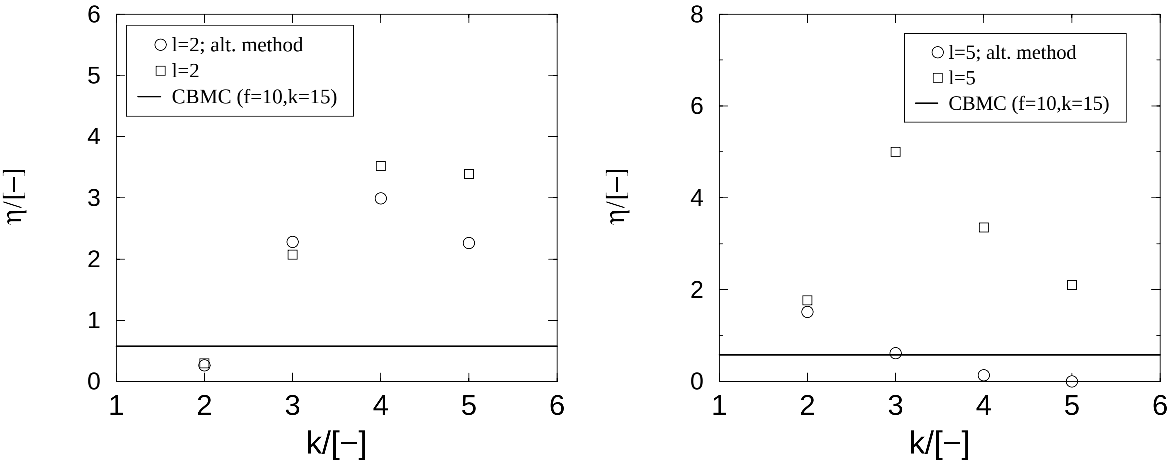

Figure 3.3: Efficiency (arbitrary units) as a function of the number of trial directions (k) for a given recoil length (l) for the two different algorithms to compute the Rosenbluth weight (section 3.2.2 and the alternative method of appendix A). $N = M = 20$ and $\rho = 0.4$. Left: $l = 2$, Right: $l = 5$. Note that for CBMC, the number of trial directions is constant ($f = 10$, $k = 15$).

the probability that segment i is open. The probability to follow the path $1, 2, 4$ along this tree is equal to

$$\Psi = p_1 \left[\frac{p_2^\star p_3^\star}{2} + \frac{p_2^\star (1 - p_3^\star)}{1} \right] \tag{3.21}$$

In this equation, $p_2\star$ is the probability to successively grow segment 4 from segment 2. The expression for $p_2\star$ is similar to the previous expression

$$p_2^\star = p_2 \left[\frac{p_4 p_5}{2} + \frac{p_4 (1 - p_5)}{1} \right] \tag{3.22}$$

The physical meaning of $p_3\star$ is the probability to grow either 6 or 7 starting from 3. This means that segment 3 and at least 6 or 7 have to be open

$$p_3^\star = p_3 \left[1 - (1 - p_6)(1 - p_7)\right] \tag{3.23}$$

For different chain and recoil lengths, we simply have to use the previous expressions in a recursive way:

- For a part of the tree that is part of the backbone, we have to calculate the probability that the backbone is followed; see table 3.2.
- For a part of the tree that is not part of the backbone, we have to calculate the probability that at least one trial direction is open. This is of course equal to 1 minus the probability that none of the directions are open; see, for example, equation 3.23.

A possible way to program this on a computer is to use a parent/child concept, in which every point of the tree has pointers to both its parent and its children. One can use the same recursive operators for a parent and all descendants of the parent.

An important difference with the algorithm in section 3.2.2 is that we have to extend all feelers up to length l, even if a direction is closed [116]. This means that we have to compute many

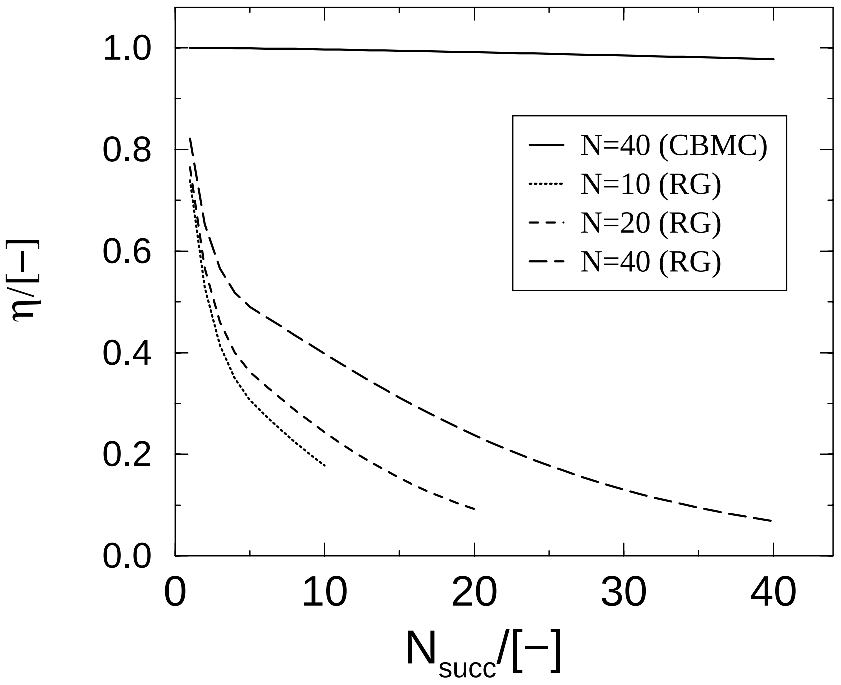

Figure 3.4: Fraction of chains (η) that are successfully grown up to length N_{succ} as a function of N_{succ} for $\rho = 0.4$ and $T = 5.0$. For RG, we have used $f = 5$, $l = 5$, and $k = 3$. For CBMC, we have used $f = k = 10$.

more trial directions compared to the algorithm in section 3.2.2. Although it is possible to reduce the fraction of CPU time that is spend in the calculation of the energy of a trial segment (see section 2.2), this algorithm will always be computationally more expensive than the algorithm in section 3.2.2. In figure 3.3, we have plotted the efficiencies of the method described in this appendix and the method described in section 3.2.2 for $N = M = 20$ and $\rho = 0.4$. It is found that for a large recoil length and number of trial directions, the algorithm described in this section becomes less efficient. However, the method described in this appendix is still almost a factor of 5 faster than CBMC for $l = 2$.

We found that although this algorithm is correct, in principle, this method is quite difficult to program. Although every program with recursive functions can be transformed to a program without recursion, we found that this method is relatively difficult to program without this technique. Because of the lower efficiency and the complexity we do not recommend to use this algorithm. However, there may be other problems where an approach like the one sketched in this appendix is useful.

3.6 Appendix B: Parallelization

In section 2.3, we have discussed a parallel CBMC algorithm. It was found that, although the construction of a single chain cannot be parallelized efficiently on a large number of processors, one can construct multiple chains instead. This task can readily be divided among processors. One of these chains is selected as the new configuration, while the remaining chains are thrown away. This introduces a bias in the generation of the new configuration, which can be removed exactly by a modification of the acceptance / rejection rule.

In such a multiple chain algorithm, it is essential to have a good load balance. This means

that every processor is doing roughly the same amount of work. Therefore, the distribution in CPU time for the construction of a chain should be as small as possible. In figure 3.4, we have plotted the fraction of chains that is successfully grown as a function of the maximum chain-length that has been attained during the construction of a chain for various chain-lengths (systems 1,3,5 of section 3.3.2). Note that in CBMC, a chain is only discarded for numerical reasons when the Rosenbluth weight is in the order of the machine accuracy of the computer (roughly 2×10^{-308} for the computer used in this study). For the Boltzmann factor of a Lennard-Jones potential with $\sigma = \epsilon = \beta = 1$, this corresponds to a pair separation of $r_{ij} = 0.64$. It turns out that the distribution in CPU time is much wider for RG than for CBMC. The fact that in RG many configurations can be thrown away before the complete chain is constructed is one of the main reasons why RG is more efficient than CBMC. However, it also implies that multiple chain algorithms cannot be parallelized efficiently, which makes RG less suitable for parallelization.

3.7 Appendix C: Fixed endpoints

In this appendix, we will show how to incorporate the RG method into a scheme that regrows chain segments between fixed endpoints. Such schemes are important, for example, for the calculation of phase equilibria of cyclic alkanes [67, 68] or for the simulation of cyclic peptides [85,86]. Also, for very long chains, complete regrowth of a chain will have a low acceptance probability. Therefore, it can be efficient to regrow only a part of the chain while all other segments keep their positions; the endpoints of the segment that is regrown are determined by the part of the chain that is not regrown. It is important to note that we do not claim that the algorithm described in this appendix is better (more efficient) than other algorithms like, for example, the ECB method of Escobedo and co-worker [117]. Instead, we would like to demonstrate the flexibility of the RG scheme and demonstrate that it can be incorporated into various other algorithms. For more information on fixed endpoints algorithms, we refer the reader to refs. [29, 67, 68, 85, 86, 117–119].

Consider a fully flexible linear chain of N elements, of which a randomly selected segment of N_{fix} beads ($0 < N_{\text{fix}} < N-1$) is cut and regrown using RG; the positions of all other segments are unchanged. To improve the efficiency, trial positions are generated using the bonded (internal) part of the potential energy (see section 3.2.2). However, the bonded energy between the last bead of the segment of length N_{fix} that is grown and the fixed endpoint is not taken into account for the generation of the position of this last bead. For the probability that a trial position is considered as "open" we have used

$$\begin{aligned} p_{\text{open}} &= \min\left(1, \exp\left[-\beta u_{\text{ext}}\right]\right) \times \exp\left[-\beta B\left(i\right) \times \left(l - l_0\left(i\right)\right)^2\right] \\ &= p_{\text{ext}}\left(u_{\text{ext}}\right) \times p\left(l, i, \beta\right) \end{aligned} \tag{3.24}$$

in which $\beta = 1/\left(k_B T\right)$, u_{ext} is the external (non-bonded) energy (for the last bead of the segment of length N_{fix} that is grown, the bonded energy between this bead and the fixed endpoint is also included in u_{ext}), l is the distance to the fixed endpoint, and $B\left(i\right)$, $l_0\left(i\right)$ are constants that only depend on the number of beads between the bead that is being grown and the fixed endpoint (i). Note that $B\left(0\right) = 0$. Both $B\left(i\right)$ and $l_0\left(i\right)$ can be determined from a short simulation in which the distribution of the distance between beads is recorded as a function of i. The probability that a bead is considered "open" is both a function of the external energy and the probability that one is able to reach the fixed endpoint after i beads. Because of the formulation in equation 3.24, one does not have to calculate the (usually computationally expensive) external energy (u_{ext}) for beads that are considered as "closed" due to their distance (l) to the endpoint (which

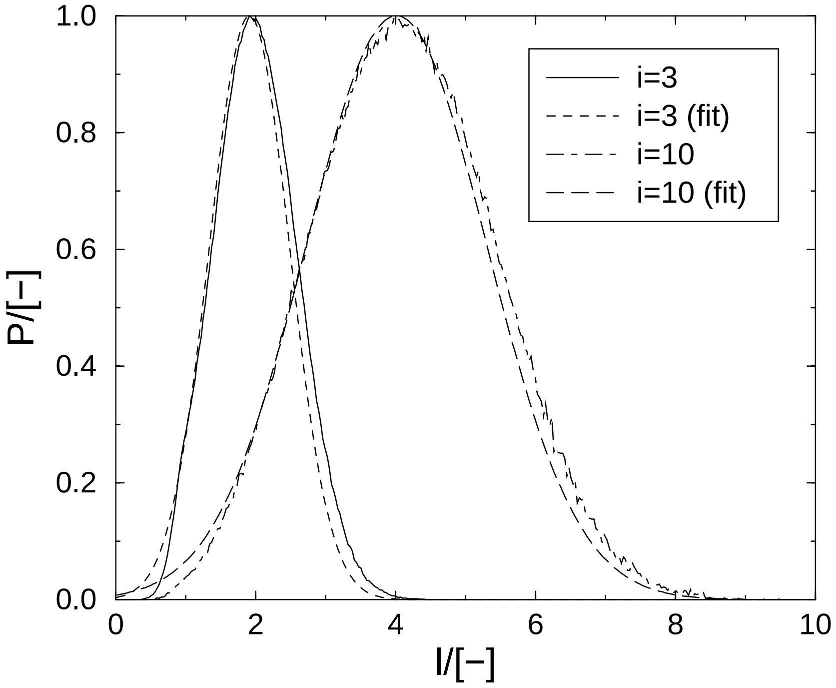

Figure 3.5: Probability distribution of the distance between two beads (l) as a function of the number of segments between the beads (i). $a = 10.0$, $C = 2.0$, $N = 15$, $\beta = 2.0$. The probability distribution is fitted using $p(i) = \exp\left[-\beta B(i) \times (l - l_0(i))^2\right]$. This function is able to describe the simulated probability distribution quite well.

is computationally very cheap to calculate).

To test this algorithm, we have simulated a single chain of which the particles interact with a DPD (Dissipative Particle Dynamics) potential [120–122]. For this DPD potential, every pair of beads has a soft repulsive interaction:

$$u_s(r) = \begin{cases} \frac{1}{2}a\left[r^2 - 2r + 1\right] & r \leq 1 \\ 0 & r > 1 \end{cases} \tag{3.25}$$

For every pair of bonded beads an additional bond-stretching potential is included:

$$u_b(r) = \begin{cases} \frac{1}{2}Cr^2 & r \leq 2 \\ \infty & r > 2 \end{cases} \tag{3.26}$$

In this work, we have used $a = 10.0$, $C = 2.0$, $N = 15$ and $\beta = 2.0$. The constants $B(i)$ and $l_0(i)$ ($i = 1 \cdots N_{\text{fix}}$) have been determined from a short simulation; see figure 3.5. In the simulation, it was decided at random to perform a trial move to regrown the entire chain using CBMC (probability of 0.01, $k = 5$) or to grow a segment of length N_{fix} between (randomly selected) fixed endpoints (probability of 0.99) using RG. To generate a bond-length from the bonded part of the potential

$$p(l)\,dl \propto \exp\left[-\beta\left(u_s(l) + u_b(l)\right)\right] l^2 dl \qquad 0 < l \leq 2 \tag{3.27}$$

we have calculated

$$f(l) = \frac{\int_0^l p(x)\,dx}{\int_0^2 p(x)\,dx} \tag{3.28}$$

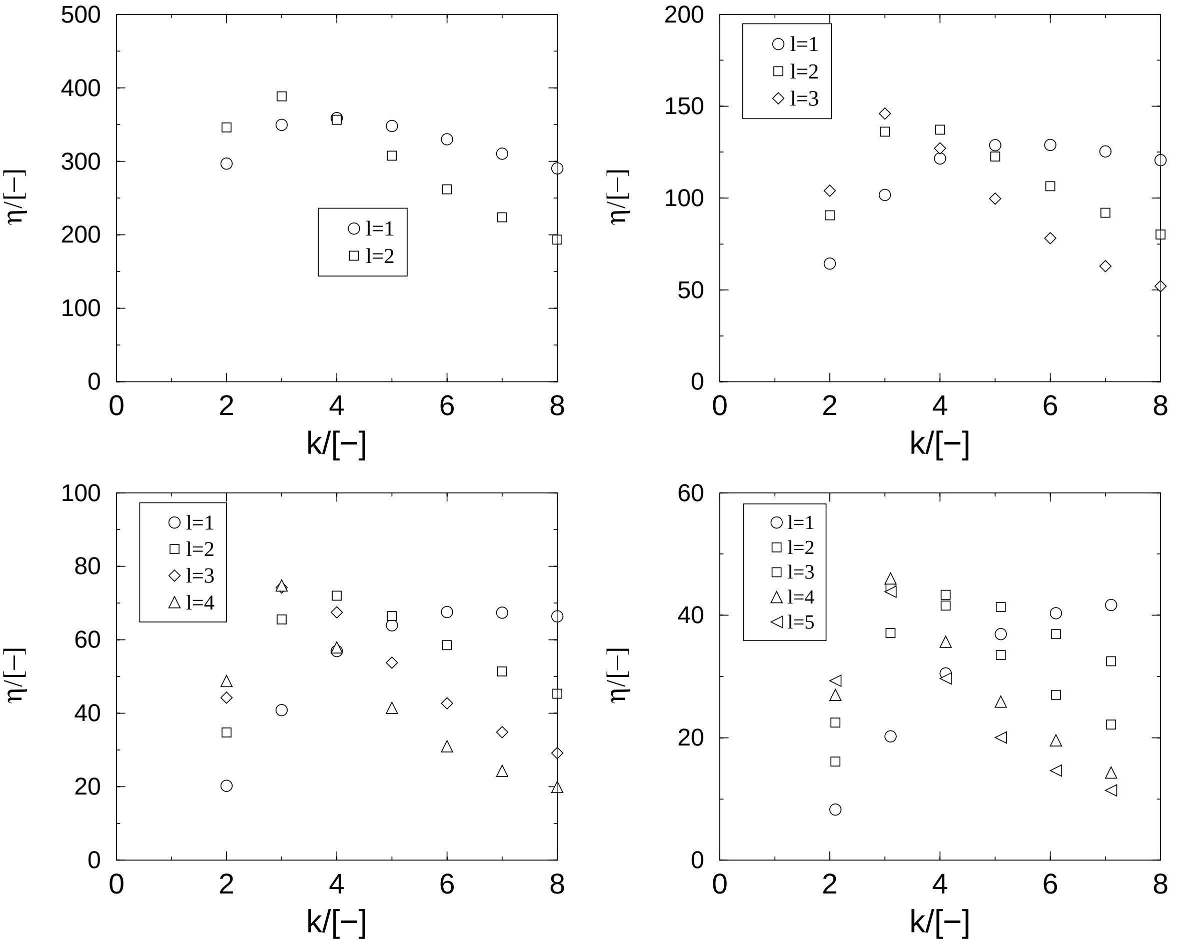

Figure 3.6: Efficiency (η) in arbitrary units as a function of the number of trial directions (k) for various recoil lengths (l). Top: left $N_{fix} = 3$, right $N_{fix} = 5$. Bottom: left $N_{fix} = 7$, right $N_{fix} = 8$.

and solved l from

$$f(l) = \psi \tag{3.29}$$

in which ψ is a uniformly distributed random number between 0 and 1 [123].

In figure 3.6, we have plotted the efficiency of the fixed endpoints RG trial move (here defined as the number of accepted trial moves divided by the amount CPU time, in arbitrary units) as a function of k, l and N_{fix}. It turns out that for large values of N_{fix}, the efficiency decreases significantly and that the optimum efficiency is at $k = 3$. However, this optimum efficiency does not differ too much from $k = 8$, $l = 1$.

Chapter 4

Adsorption of alkanes in Silicalite*

4.1 Introduction

In the previous chapters, we have discussed techniques to calculate thermodynamic properties of chain molecules. In this chapter, we will use these techniques to study the adsorption of linear and branched alkanes in the zeolite Silicalite.

Adsorption isotherms provide information on the amount of hydrocarbons adsorbed in these porous materials at a given pressure and temperature. Recent studies have revealed some interesting characteristics of the adsorption isotherms of hydrocarbons. For example, the isotherms of most linear hydrocarbons in the zeolite Silicalite show simple Langmuir behavior [124]. The isotherms of heptane and hexane, however, show an inflection point. Evidence of this surprising inflection behavior can be gleaned by careful analysis of experimental data from various sources [125–128]. More recent and systematic studies have confirmed this peculiar behavior of hexane and heptane [129–134]. It is interesting to note that computer simulation studies had preceded these experimental works with a possible explanation of this behavior in terms of a commensurate freezing of hexane and heptane in the zigzag channels of Silicalite [20].

Fewer experimental data are available for adsorption of branched hydrocarbons adsorbed in Silicalite. The adsorption isotherms of isobutane also shown an inflection [21, 135, 136] but for 2-methylpentane a simple Langmuir isotherm was found [137]. Molecular simulations have shown that the inflection of isobutane is related to the preferential adsorption of the branched alkanes at the intersections of the zigzag and straight channel of Silicalite [21].

Experimentally, the determination of adsorption isotherms of long chain alkanes can be time consuming. For example, Stach *et al.* [17] report that measurement of each isotherm for decane in Silicalite requires at least two weeks of equilibration. It is therefore an important question whether molecular simulations provide an attractive alternative for estimating the adsorption of long chain hydrocarbons in the pores of a zeolite. The main reason why experimentally it takes two weeks to achieve equilibration is that the diffusion of long chain alkanes is very slow. Such slow diffusion would lead to extremely long simulation times if the conventional molecular dynamics or Monte Carlo simulation techniques were to be used, see figure 1.2. The Configurational-Bias Monte Carlo (CBMC) technique has been developed to reduce these simulation times many orders of magnitude; see chapter 2.

In this chapter we present the results of computer simulations of linear and branched alkanes in the zeolite Silicalite. We focus on the development of the model and a detailed comparison with experimental data for the linear and branched alkanes. In addition we demonstrate that these isotherms can be described quantitatively with a dual-site Langmuir isotherm.

*This chapter is based on refs. [21, 36].

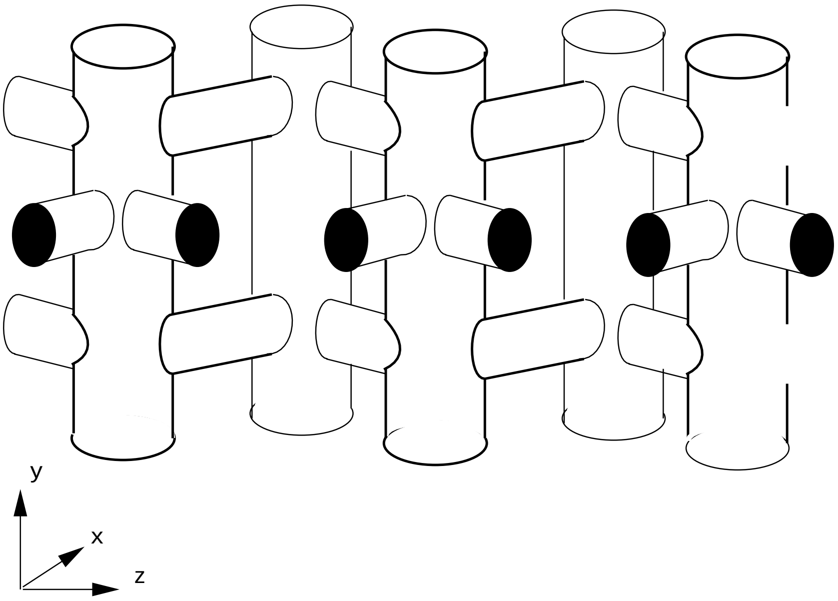

Figure 4.1: Schematic drawing of the pore structure of Silicalite (MFI type framework). See also figure 1.1.

A schematic drawing of the Silicalite structure is shown in 4.1. Silicalite has two types of channels, straight and zigzag channels which are connected via intersections.

4.2 Model

In practical applications of the adsorption of hydrocarbons in zeolites the temperatures and pressures of interest can vary significantly. It is therefore important that the models for the hydrocarbon and zeolites give reasonable results for the thermodynamics over a wide range of temperatures and pressures.

The linear and branched alkanes are described with a united-atom model [138], *i.e.* CH_3, CH_2, and CH groups are considered as single interaction centers [139]. The bonded interactions include bond-bending and torsion potentials, the non-bonded interactions are described with a Lennard-Jones potential. A way to obtain reasonable Lennard-Jones parameters is to fit the Lennard-Jones parameters to reproduce the vapor-liquid curve of the phase diagram. In ref. [49] it is shown that the prediction of the vapor-liquid curve is very sensitive to the choice of the non-bonded Lennard-Jones potential. The model of Siepmann *et al.* [47] can describe the vapor-liquid curves of a large number of alkanes over a large temperature range. This model has been further refined and extended to branched alkanes in refs. [53, 59, 63]. We have compared the different sets of parameters to investigate how sensitive the adsorption of hydrocarbons in zeolites is for these parameters. This comparison indicates that the results do not differ significantly and gave a very good prediction of the vapor-liquid curves for all tested sets. The details of the alkanes model we have used in this work are given in appendix A.

Following Kiselev and co-workers [24], the zeolite is modeled as a rigid crystal [140]. This allows the use of interpolation techniques to determine the interaction of an alkane atom with the zeolite and avoids having to consider all zeolite atoms [107, 141]. The interactions of the alkane atoms with the zeolite atoms are dominated by the dispersive interactions with the oxygen atoms [24], these interactions are described with a Lennard-Jones potential.

Table 4.1: Lennard-Jones parameters for the zeolite-alkane interactions: of the model proposed by June *et al.* [141], Smit *et al.* [142], and the model developed in this work. The potentials were truncated at 13.8 Å, and the usual tail corrections have been applied [29, 32].

	$\frac{\sigma_{CH_iO}}{[\text{Å}]}$	$\frac{\epsilon_{CH_O}/k_B}{[K]}$	$\frac{\epsilon_{CH_2O}/k_B}{[K]}$	$\frac{\epsilon_{CH_3O}/k_B}{[K]}$	$\frac{\epsilon_{CH_4O}/k_B}{[K]}$
June *et al.*	3.364	50.0	83.8	83.8	-
Smit *et al.*	3.64	51.3	54.4	87.5	-
This work	3.60	58.0	58.0	80.0	96.5

Table 4.2: Parameters for the Lennard-Jones potential describing the interactions between pseudo atoms of a branched alkane [53]. We have also given the parameters for the methane-methane interactions [143]. We have used the Jorgensen mixing rules [89] to compute interactions between different pseudo-atoms: $\sigma_{ij} = \sqrt{\sigma_{ii}\sigma_{jj}}$, $\epsilon_{ij} = \sqrt{\epsilon_{ii}\epsilon_{jj}}$. The potentials were truncated at 13.8 Å, and the usual tail corrections have been applied [29, 32].

	$(\epsilon/k_B)/[K]$	$\sigma/[\text{Å}]$
CH_4-CH_4	148.0	3.73
CH_3-CH_3	98.1	3.77
CH_2-CH_2	47.0	3.93
CH-CH	12.0	4.10

In ref. [70] it is shown that to describe an adsorption isotherm sufficiently accurately, it is important to have models that yield an accurate prediction of both the Henry coefficient and the heat of adsorption. For the short chain alkanes there are sufficient experimental data to arrive at a reasonably reliable model, for the long chain alkanes, however, there are far less experimental data, which makes it difficult to perform a careful test of the model.

To reduce the set of interaction parameters, we have assumed that the size parameter of the Lennard-Jones potential (σ) is equal for all pseudo atoms including methane, ethane, and propane. However, one would expect that all size parameters are different. Because a united-atom force field implies lumping of parameters it is very difficult to justify values of parameters based on other reasons than a good reproduction of experimental data, so the choice of equal σ is justified [144]. This has as additional advantage that the same interpolation table can be used for all interactions and thus memory is saved. In table 4.1 the parameters of the Lennard-Jones potential are given of two models that we have used in this study. These parameters have been optimized to give a reasonable prediction of the Henry coefficients and heats of adsorption.

4.3 Simulation technique

In this work we have used NVT Monte Carlo simulations in combination with the CBMC technique (see chapter 2) to determine the heat of adsorption and the Henry coefficient [69, 107]. The adsorption isotherms have been determined using grand-canonical Monte Carlo simulations, also in combination with the CBMC technique. The technical details of these methods are described in refs. [107, 145] and in chapter 2; below a short description is given.

The simulations are performed in cycles, in each cycle an attempt is made to perform one of the following (randomly selected) moves [146]

- displacement of a chain; a chain is selected at random and given a random displacement. The maximum displacement was taken such that 50% of the moves were accepted.
- rotation of a chain; a chain is selected at random and given a random rotation around the center of mass. The maximum rotation was selected such that 50% of the moves were accepted.
- partly regrowing of a chain; a chain is selected at random and part of the molecule is regrown using the CBMC scheme. It is decided at random which part of the chain is regrown and with which segment the regrowing is started.
- regrowing of the chain (only for the case of NVT-simulations); a chain is selected at random and is completely regrown at a randomly selected position. During this step data are collected from which the Henry coefficient is determined.
- exchange with reservoir (only in the case of grand-canonical simulations); it is decided at random whether to add or to remove a molecule from the zeolite. This exchange with the reservoir is done using the CBMC scheme.
- change of identity (only in the case of mixtures); one of the components is selected at random and an attempt is made to change its identity [50]. The acceptance rules for this type of move are given in ref. [147]. Simulations of alkane mixtures are presented in the next chapter.

The relative probabilities for attempting these moves were such that in the NVT-simulations 10% of the total number of moves were displacements, 10% rotations, 10% partial regrowths, and 70% regrowths of the entire molecule. For the case of grand-canonical simulations of the pure components the distribution of moves was: 15% displacements, 15% rotations, 15% partial regrowths, and 55% exchanges with the reservoir. For alkane mixtures the number of exchanges was reduced to 50% and the remaining 5% of the moves were attempts to change the identity of a molecule. The number of trial orientations in the CBMC scheme (k) was eight for all molecules. In addition, we used the multiple first bead scheme (see section 2.1) with 15 trial positions for the first bead (f). For the growth of a branched molecule we have used the procedure described in section 2.4. For the NVT-simulations the total number of cycles was at least 10^6. In a cycle, the number of trial moves is equal to the number of particles with a minimum of 20 trial moves per cycle. The grand-canonical simulations were started from the end configuration of a simulation at a lower chemical potential. We have allowed at least 10^5 cycles for equilibration and subsequent production runs were at least 10^5 cycles. For the longest chains and at high loading a larger number of cycles were performed.

4.4 Linear alkanes

4.4.1 Heats of adsorption and Henry coefficients

To test our model we use the experimental heats of adsorption and Henry coefficients of the linear and branched alkanes. In appendix B, a compilation of the experimental data is given.

In figure 4.2 the experimental heats of adsorption are compared with the results from simulations using the models given in table 4.1. Both the model of June *et al.* [141] and the model introduced in this work reproduce the experimental data. In addition, this figure also shows that our simulation results are in excellent agreement with the CBMC integration calculations of Maginn *et al.* [71].

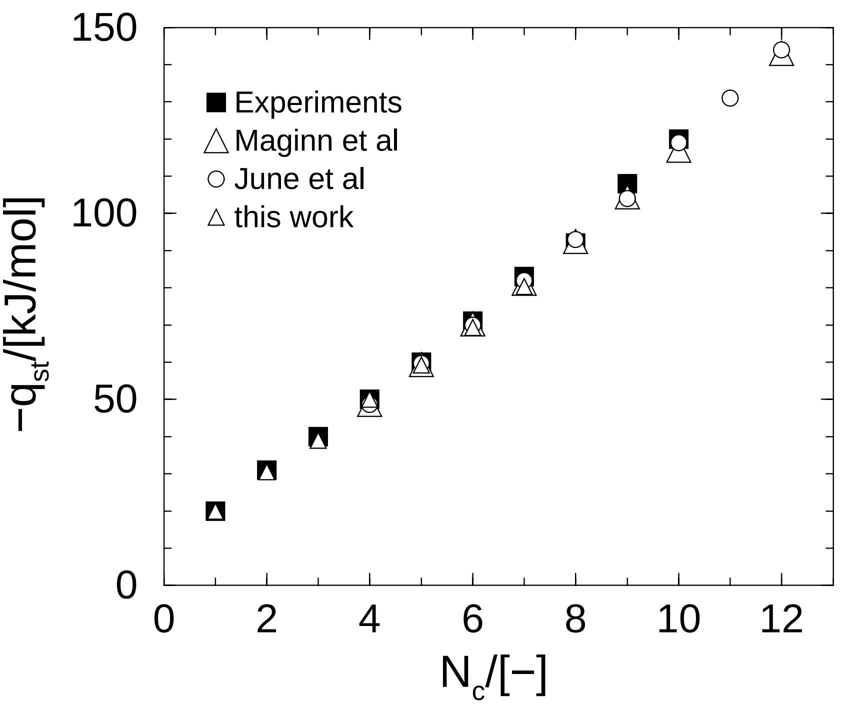

Figure 4.2: Heats of adsorption ($-q_{st}$) as a function of the number of carbon atoms N_c of the alkanes adsorbed in Silicalite.

Figure 4.3 compares the experimental Henry coefficients with the predictions of the various models. For the Henry coefficient there is a significant difference between the various models. Note that the results are plotted on a logarithmic scale, a small deviation from the experimental value gives already a significant deviation for the adsorption isotherms. The results indicate that the model June *et al.* [141] gives a good description for butane, but deviates significantly for the higher alkanes. Our model describes the short chain alkanes very well but deviates, although less than the model of June *et al.*, for hexane and the longer alkanes. For both models, the simulation data for the Henry coefficients fall on a straight line. The experimental data, however, suggest that the Henry coefficients deviate from a straight line for the longer alkanes. We have also calculated the Henry coefficients for various other sets of parameters but always obtained a straight line. Although we did not test all combinations of parameters, these results indicate that with the current set of models one cannot describe this deviation from a straight line. It would be interesting to investigate whether a straight line is also observed in a simulation with a flexible zeolite lattice.

4.4.2 Adsorption isotherms

The adsorption isotherms of methane, ethane, and propane as predicted by the model developed in this work are reported in ref. [148]. In the tested temperature range $T = 275K–350K$ the model reproduces the experimental isotherms very well.

For butane the simulation results are compared in figure 4.4 with experimental data of Abdul-Rehman *et al.* [149, 150], Richard *et al.* [151], Stach *et al.* [124], Sun *et al.* [131], and Zhu *et al.* [135]. The simulation results are in good agreement with the experimental data. The maximum loading of Zhu *et al.* is considerably lower than the maximum loading of the other isotherms, which are due to impurities in the sample [152].

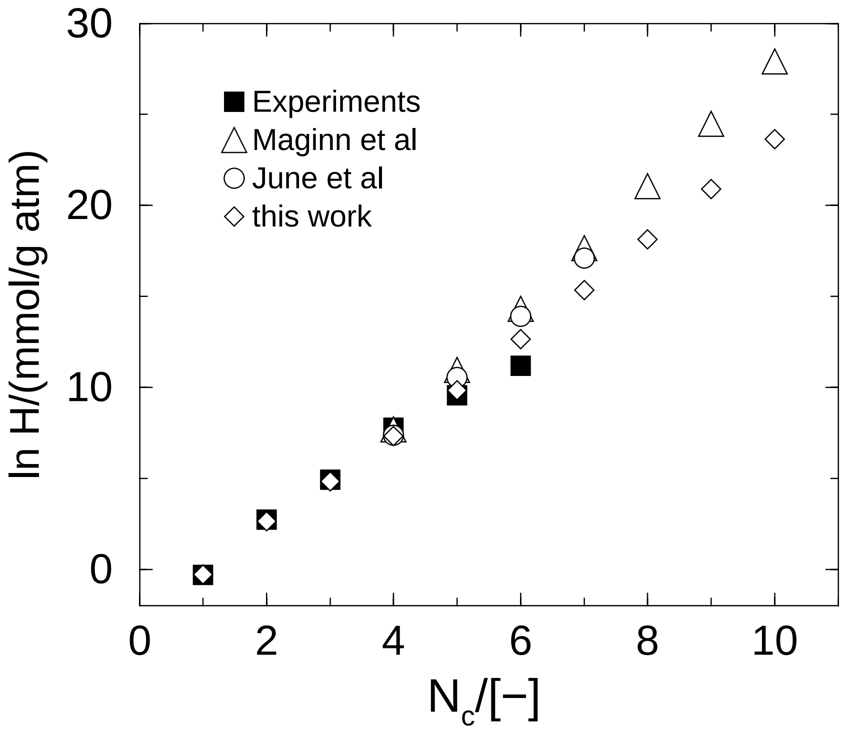

Figure 4.3: Henry coefficients, H, (in [mmol / g / Pa]) of linear alkanes as a function of the number of carbon atoms N_c in Silicalite.

The simulated adsorption isotherm of pentane is compared in figure 4.5 with the experimental isotherms of Rakhmatkariev *et al.* [126], Dubinin *et al.* [127], and Sun *et al.* [131]. The experimental data differ significantly. The maximum loading obtained by Sun *et al.* is significantly higher than the maximum loading obtained by Rakhmatkariev *et al.* and Dubinin *et al.* The maximum loading of Sun *et al.* agrees very well with the maximum loading obtained from the simulations. A similar agreement with the data of Sun *et al.* and our simulation results for the maximum loading is obtained for butane (see figure 4.4) and hexane (see figure 4.6). For these systems more experimental data is available which is consistent with the data of Sun *et al.* This suggests that the Silicalite used by Rakhmatkariev *et al.* and Dubinin *et al.* may suffer from pore blocking.

In figure 4.6 the experimental isotherms for hexane of Stach *et al.* [124], Richard and Rees [128], and Sun *et al.* [131] are compared with the simulation results using the model of June *et al.* and the model developed in this work. From the comparison with the Henry coefficients (see figure 4.3) it was already clear that the model of June *et al.* would overestimate the adsorption significantly. Our model gives a better agreement with experiments.

For heptane adsorption isotherms have been reported by Lohse and Fahlke [125], Rakhmatkariev *et al.* [126], Dubinin *et al.* [127], and Sun *et al.* [131]. The simulations agree very well with the data of Sun *et al.* Since Rakhmatkariev *et al.* and Dubinin *et al.* used the same zeolite as for the experiments of pentane a similar difference as observed for pentane has to be expected with their data and our simulation results. Although the agreement with experimental data of Rakhmatkariev *et al.* and Dubinin *et al.* is less satisfactory, both sets of experimental data show an inflection at a loading of adsorbate loading of 4 molecules per unit cell (which corresponds to approximately 0.7 mmol / g). This inflection is also observed in the simulated adsorption isotherms. In the next section we will discuss this aspect in detail.

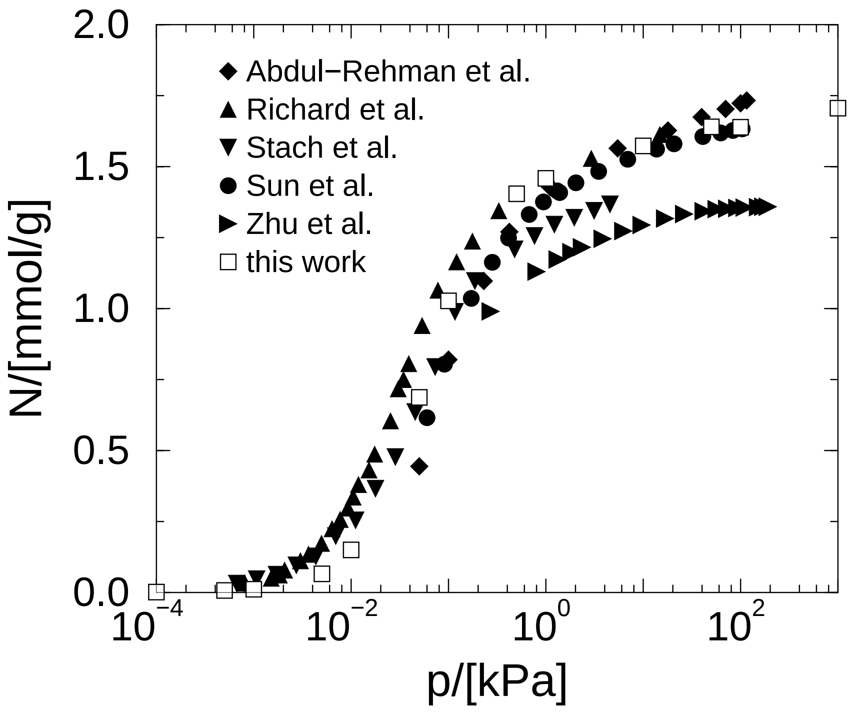

Figure 4.4: Comparison of adsorption isotherms of butane in Silicalite.

For octane and nonane the simulation results are compared with the data of Sun *et al.* [131] in figures 4.8 and 4.9, respectively. It is interesting to note that our simulations show a pronounced inflection at a loading of 4 molecules per unit cell. The experimental data of Sun *et al.* were obtained above this loading and therefore no inflection was noted experimentally. The agreement between the simulation results and experiments would improve significantly if the model would yield three times larger Henry coefficients (see figure 4.3). The precise reason for the inflection behavior of these molecules is as yet unclear to us. The experimental data of Yang and Rees [133] indicate inflection behavior for octane and nonane. At this point it is important to note that the number of accepted exchanges with the reservoir in the CBMC scheme becomes for these molecules at high pressures (above 100 Pa) very low. Therefore we had to increase the total length of the simulation and the total number of trial orientations significantly. We have performed simulations starting from a low loading and increasing the pressure as well as simulations starting from a high loading and decreasing the pressure. Both gave identical results. Therefore we do have some confidence that the inflection is not due to limitations of the CBMC technique. Furthermore, for these large molecules at these high pressures it is an important question whether the assumption of the zeolite being rigid is still reasonable.

In figure 4.10, the simulated isotherms for linear alkanes have been collected together for comparison and discussion.

4.4.3 Discussion

The adsorption isotherm of heptane shows a distinct inflection which suggests that a (phase)-transition takes places in the pores of the zeolite. A well-known example of a phase transition in porous systems is capillary condensation. If in a system capillary condensation is observed the adsorption isotherm shows a step and hysteresis occurs, such isotherms are denoted as type IV or V [153]. Steps or inflections without hysteresis are occasionally observed in adsorption

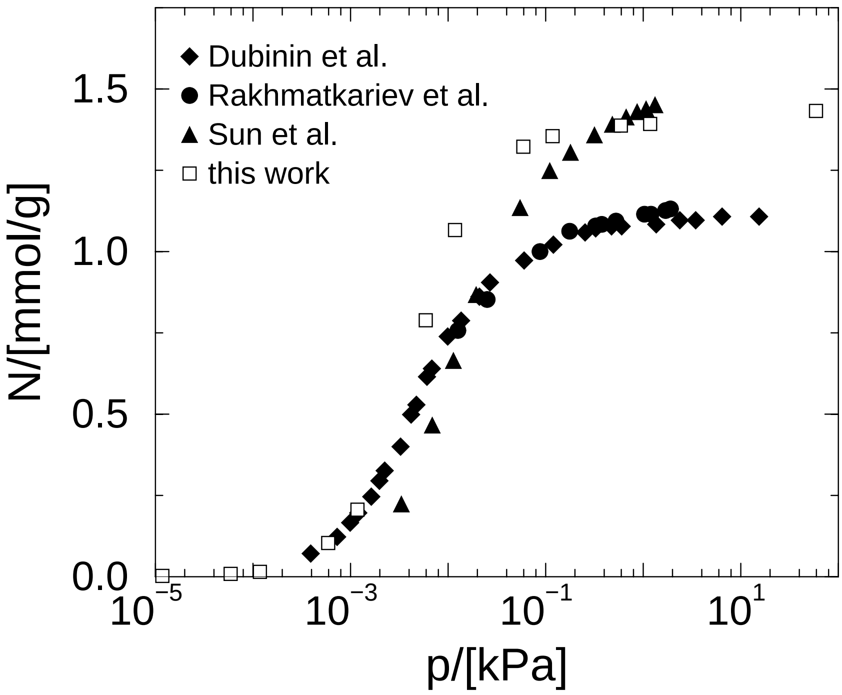

Figure 4.5: Comparison of adsorption isotherms of pentane in Silicalite.

isotherms. Such adsorption isotherms are classified as type VI isotherms. These steps are usually due to wetting or pre-adsorption and occur mainly on flat surfaces [154]. The pores of most zeolites are too small to observe capillary condensation. In these narrow pores the fluid behaves as a quasi one-dimensional fluid and in a such one-dimensional system phase transitions do not occur . Therefore for zeolites one would expect that for the linear alkanes the adsorption isotherms are of the type I. If a stepped adsorption isotherm is observed, this step is usually attributed to capillary condensation in the exterior secondary pore system formed by the space between the different crystals [124]. If such a measurement would have been performed with a perfect crystal, an ordinary type I isotherm would have been observed. For linear alkanes with five or less carbon atoms a simple Langmuir isotherm has been found [158]. Also temperature programmed desorption studies show that among the linear alkanes hexane and heptane behave distinctly differently [129, 130, 132, 134]. Therefore the results for heptane and also hexane are surprising and in this section we discuss these results in detail.

Detailed inspection of the hexane experimental data of Richard and Rees [128] suggests that a small kink is present at about 4 molecules per unit cell at $T = 333K$. In addition, the data in [128] indicates that with increasing temperature this inflection becomes more pronounced. Stach *et al.* [124] and Lohse *et al.* [159] did not observe an inflection at room temperature. Eder and Lercher [160–163] observed an inflection at $T = 333K$. Yang and Rees [132] also observed that this inflection disappears when the temperature is increased above $T = 383K$. Sun *et al.* [131] state that an inflection is observed in a narrow temperature window ($310K < T < 360K$), below and above this temperature window normal type I isotherms are observed. For heptane both the experiments and simulations show a pronounced inflection.

The anomalous behavior of hexane and heptane in Silicalite compared to other alkanes is now well established. However, the temperature dependence of the inflection of hexane and heptane is still debated in the literature. The simulation results for hexane of Smit and Maesen [20] indicate that as the temperature increases the inflection becomes more pronounced. The

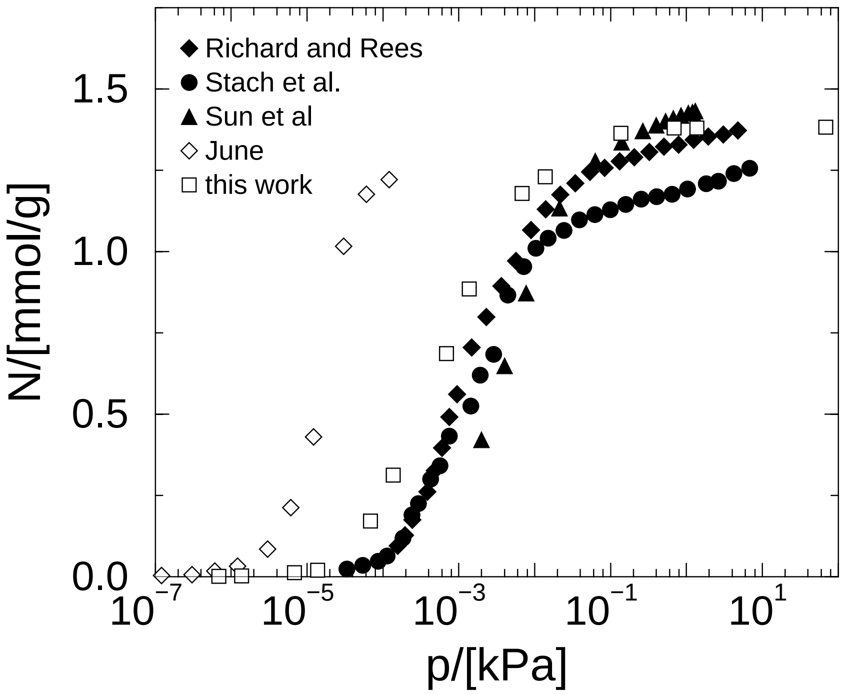

Figure 4.6: Comparison of adsorption isotherms of hexane in Silicalite.

experimental data of Richard and Rees [128] appear to support this point. However, recently Sun *et al.* [131] and Yang and Rees [132] claim that their experimental data indicate that as the temperature is increased the inflection disappears. It is therefore interesting to investigate the temperature dependence of the inflection in detail.

In figure 4.11, the simulated adsorption isotherms of hexane obtained at temperatures ranging from 298K to 373K are compared with the experimental data of Sun *et al.* [131], Richard and Rees [128] and Yang and Rees [132]. At about 300K the simulations are in good agreement with the data of Richard and Rees [128] but deviates slightly from the data of Sun *et al.* There is excellent agreement between the simulations at 323K and 343K and the experimental data of Sun *et al.* [131]. When the temperature is further increased to 373K, we note that the experimental data of Sun *et al.* are significantly below the simulation results. The reason for this deviation is unclear. It is important to note that our simulations at 373K are in excellent agreement with the data of Yang and Rees [132]. Our simulations show a regular shift of the isotherm towards higher pressures if the temperature is increased; this agrees with the experimental observations of Yang and Rees [132], but not with those of Sun *et al.*

At room temperatures both the experiments and the simulations show an inflection at a loading of 4 molecules per unit cell. At high temperatures all simulated adsorption isotherms show inflection behavior. Simulation at $T = 1000$K have confirmed this. A careful examination of our simulation results and also the experimental data of Yang and Rees [132] shows that these results are in very good agreement. It also shows that from the experimental data it is difficult to conclude whether or not an inflection is present at higher temperature. Our CBMC simulations do not support the contention of Yang and Rees that the inflection behavior disappears at higher temperatures. As is shown in figure 4.11, the isotherm data of Sun *et al.* at high temperatures were not obtained at sufficiently high pressures to notice inflection behavior. Therefore, the observation of Sun *et al.* that the inflection behavior of n-hexane is restricted to a temperature window ($310\,K < T < 360\,K$) is also not borne out.

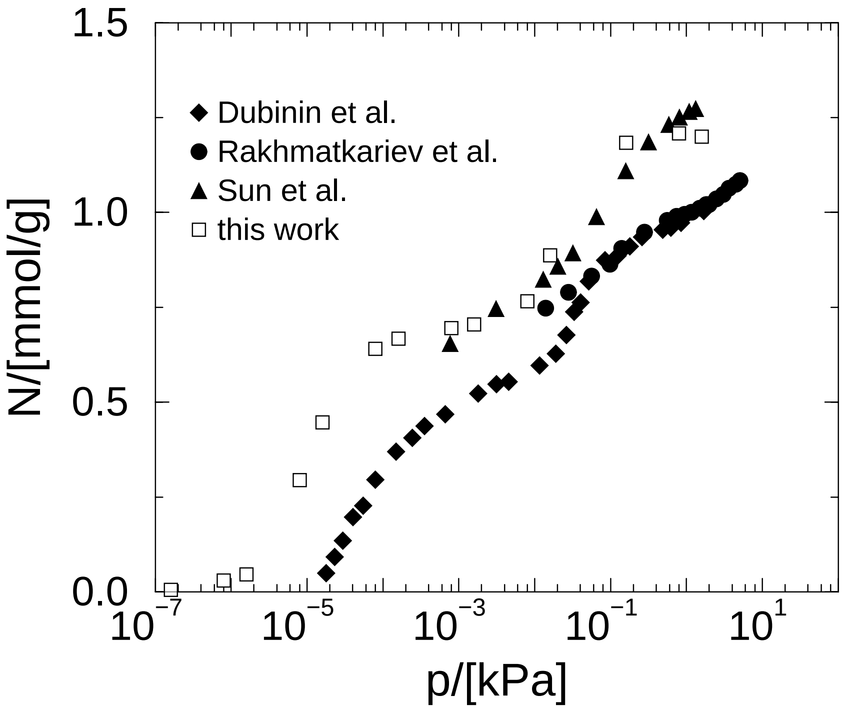

Figure 4.7: Comparison of adsorption isotherms of heptane in Silicalite.

Figure 4.14 compares the experimental adsorption isotherms of heptane of Sun *et al.* [131] and Eder [160, 162–164] obtained at temperatures ranging from 323K, 343K, and 373K with the simulation results. At 323K the simulations are in good agreement with the data of Sun *et al.* There is excellent agreement between the simulations at $T = 343K$ with the experiments of both Sun *et al.* and Eder. At $T = 373K$ the CBMC simulations agree very well with the data of Eder but there is a significant deviation with the Sun *et al.* data. This deviation is similar to the one observed earlier for hexane at $T = 373K$ (see figure 4.11).

The inflection for heptane is found by Rakhmatkariev *et al.* [126] and Dubinin *et al.* [127] at room temperature and at slightly higher temperatures by Eder and Lercher [160–163] and Sun *et al.* [131]. As is shown in figure 4.14, the isotherm data of Sun *et al.* at high temperatures were not obtained at sufficiently high pressures to notice inflection behavior. Therefore, the conclusion of Sun *et al.* that the inflection behavior of n-heptane occurs in a temperature window is not supported by our results. In the case of heptane the results clearly show that with increasing temperature the inflection behavior becomes more pronounced.

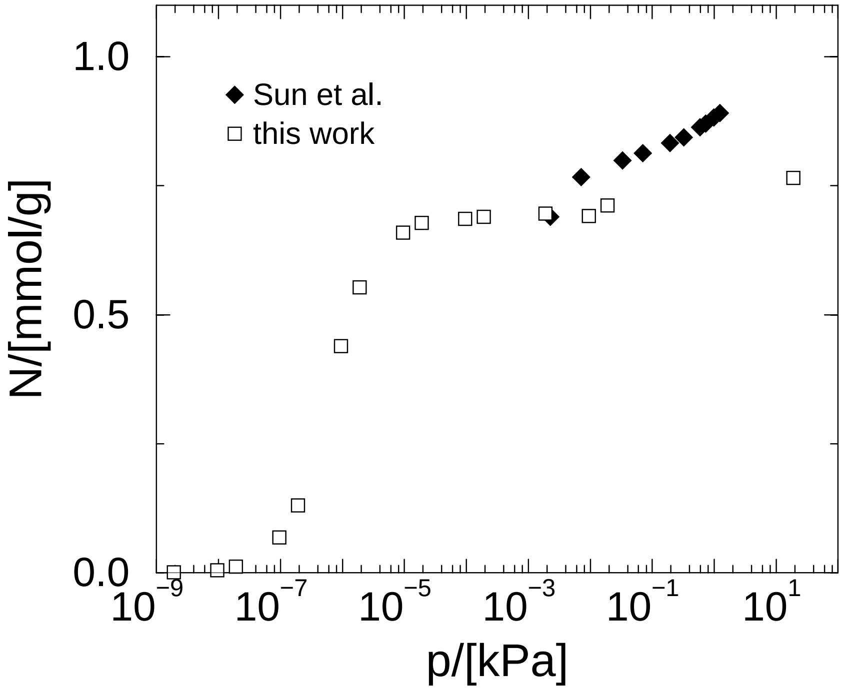

Figure 4.8: Comparison of adsorption isotherms of octane in Silicalite.

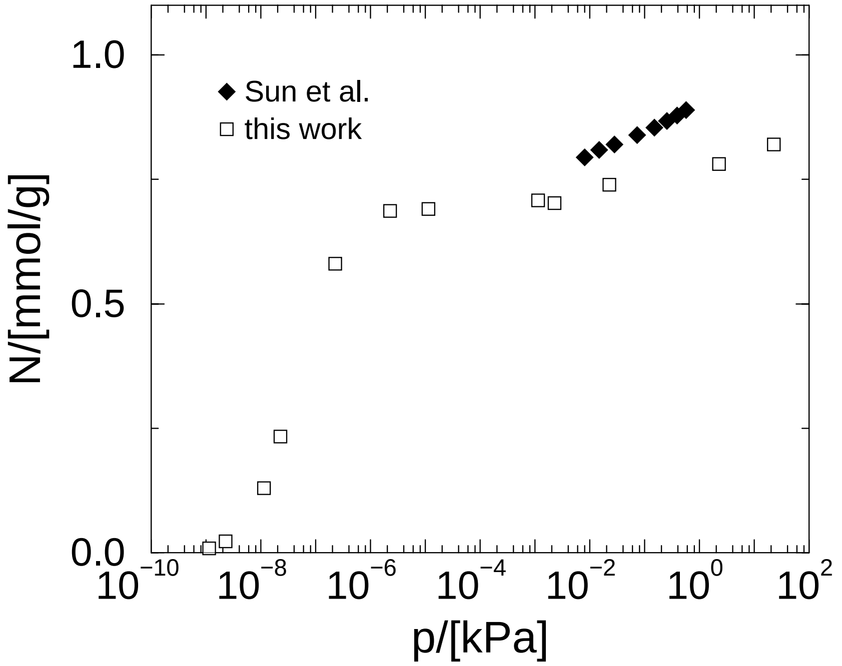

Figure 4.9: Comparison of adsorption isotherms of nonane in Silicalite.

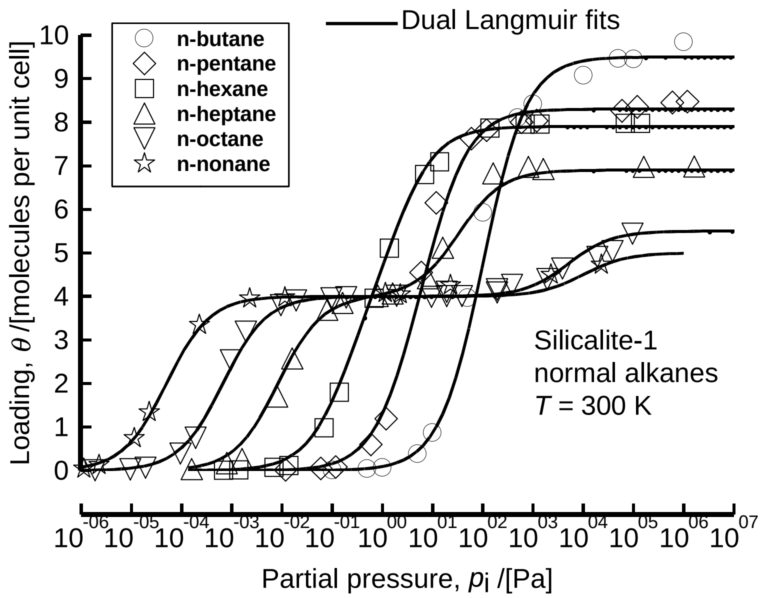

Figure 4.10: Simulated isotherms for C_4-C_9 linear alkanes in Silicalite at 300 K.

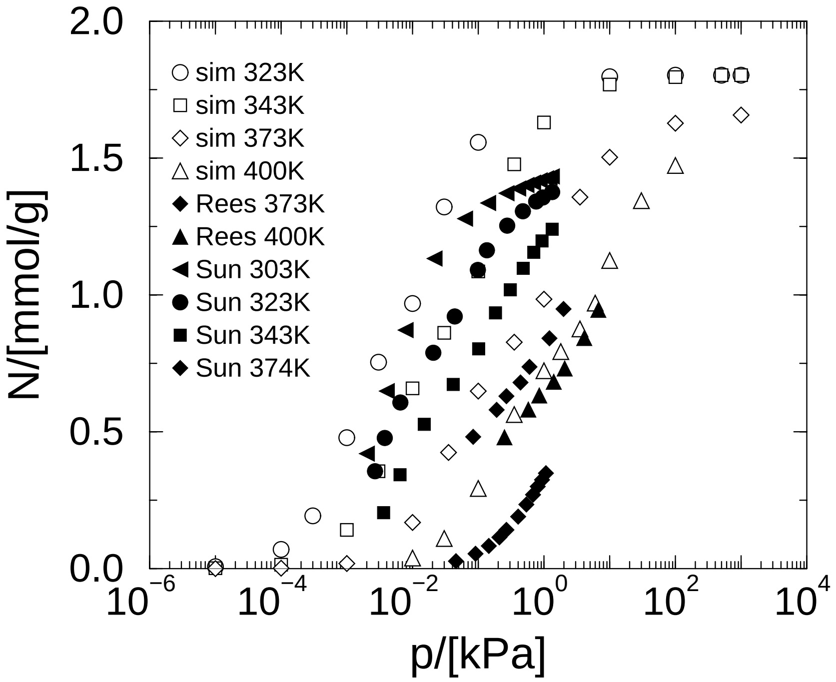

Figure 4.11: Adsorption isotherms of hexane in Silicalite at various temperatures. The open symbols are experimental data of Sun *et al.* [131], Richard and Rees [128], and Yang and Rees [132] and the closed symbols are simulation results.

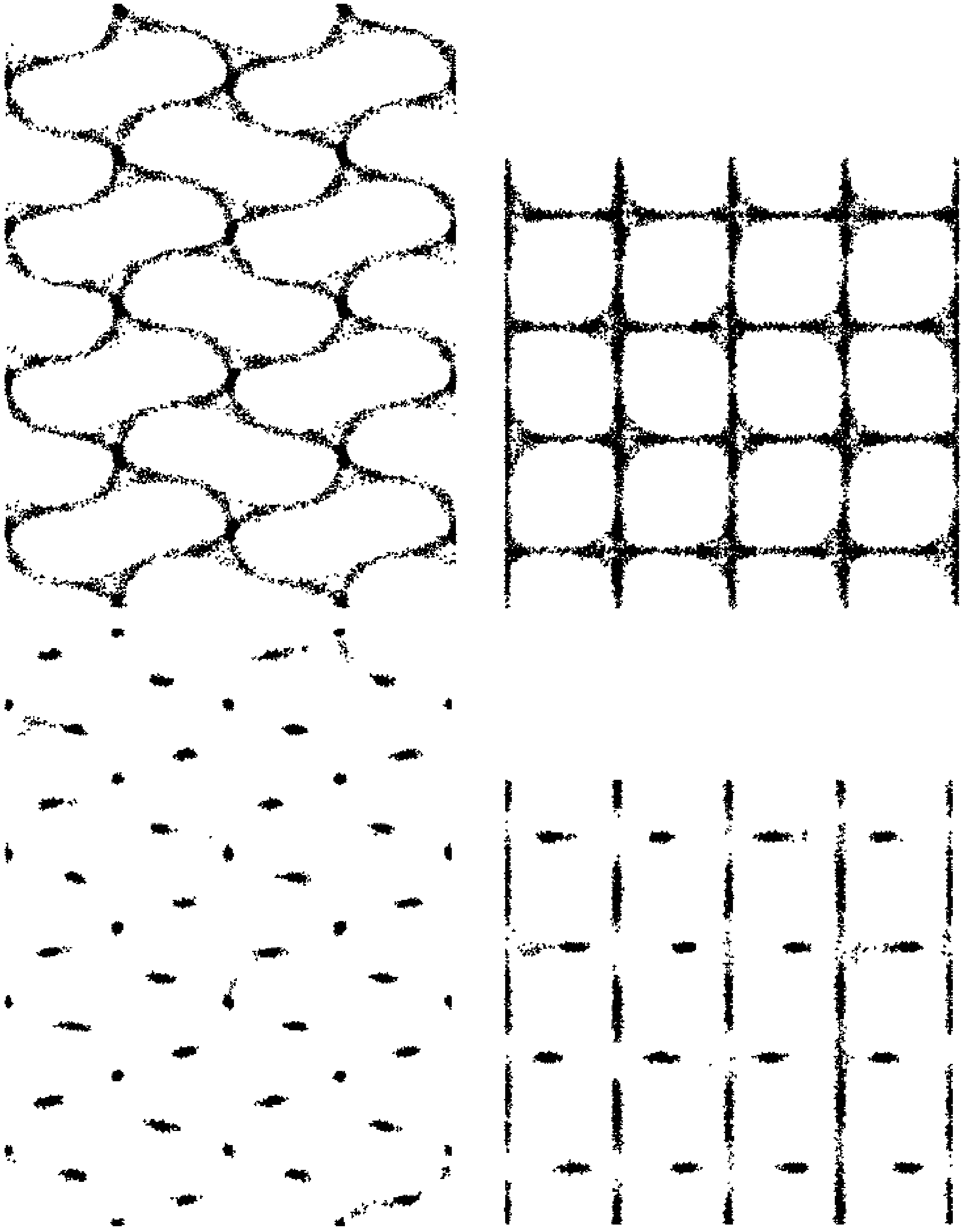

Figure 4.12: Probability distribution of hexane in Silicalite at T = 405K: (left figures) projection on the x-z plane, (right figures) projection on the x-y plane; low pressures 0.01 [kPa] (top figures) and high pressures 1000 [kPa] (bottom figures). At intervals of 200 cycles the center of mass of the hexane molecules are computed and at this position a dot is drawn this is repeated until 10000 dots have been plotted. The lines are the zeolite structure (only a quarter of the total zeolite used in the simulation is shown).

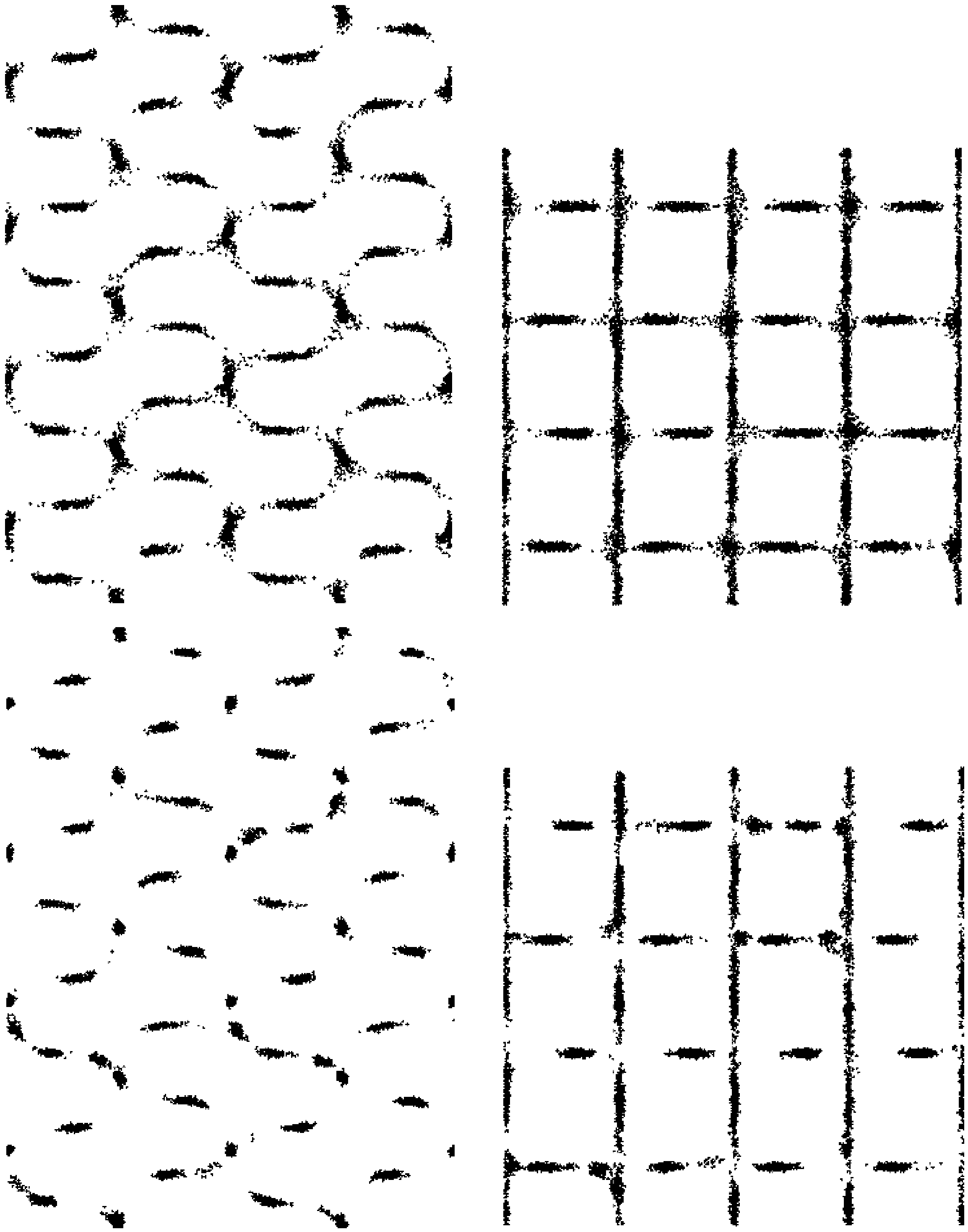

Figure 4.13: Probability distribution of butane (top figures) and pentane (bottom figures) in Silicalite at $T = 300K$: (left figures) projection on the x-z plane projection, (right figures) projection on the x-y plane at high pressures 100 [kPa]. At intervals of 200 cycles the center of mass of the molecules are computed and at this position a dot is drawn this is repeated until 10000 dots have been plotted.

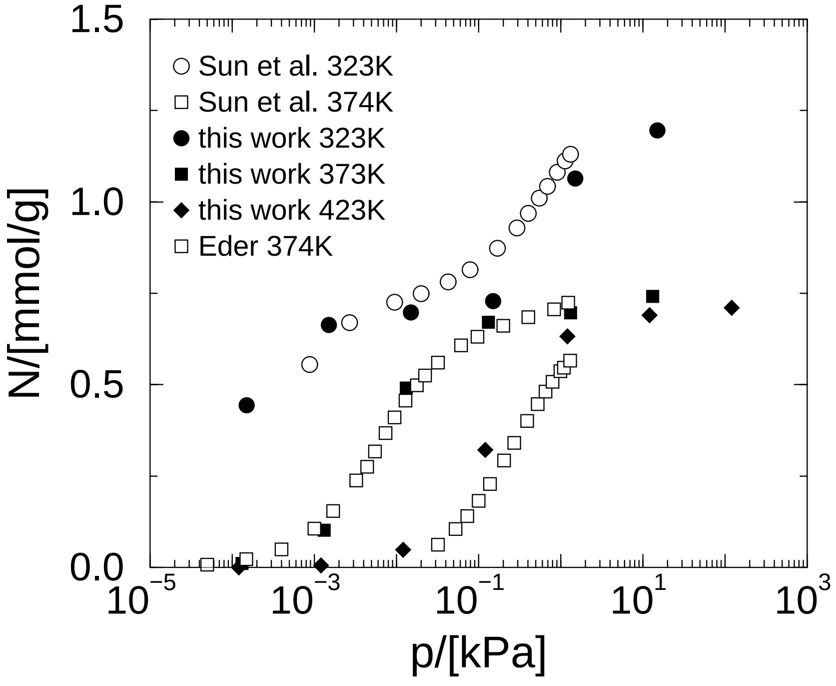

Figure 4.14: Adsorption isotherms of heptane in Silicalite at various temperatures.

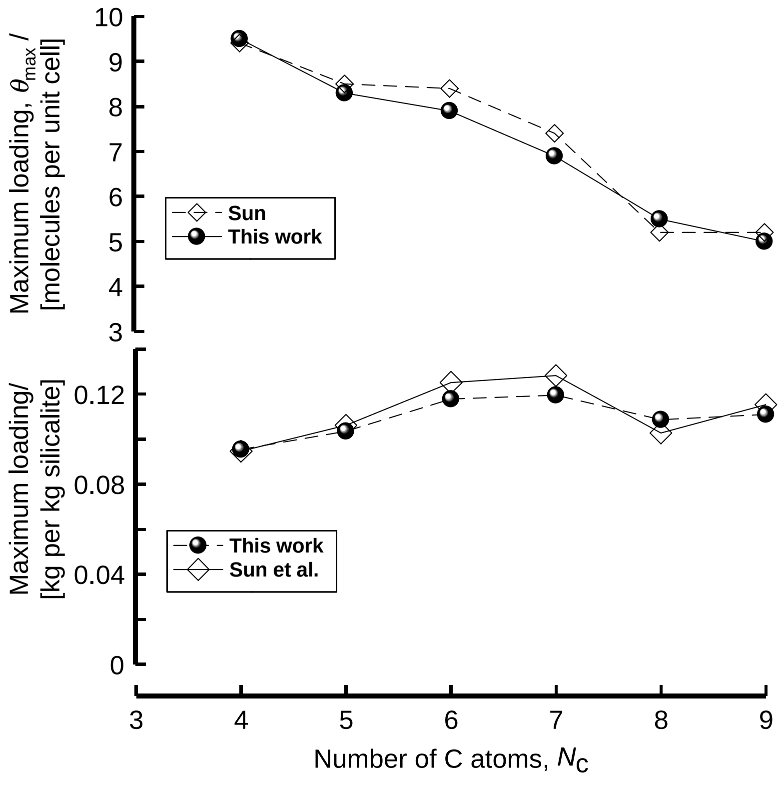

Figure 4.15: Comparison of the maximum loading for linear alkanes obtained from simulations with experimental data of Sun *et al.* [136].

A possible explanation of the peculiar behavior of heptane and hexane was given by Smit and Maesen [20] in terms of a commensurate freezing of hexane and heptane in the zigzag channels of Silicalite. Only hexane and heptane have a size that is commensurate with the size of the zigzag channel. This effect is illustrated in figure 4.12 in which we compare density distribution of the center of mass of hexane at low pressure and high pressure. At low pressure we observe a uniform distribution of the molecules in the intersections, straight and zigzag channels. This distribution completely changes at high pressures where the molecules are localized into the zigzag channels in such a way that the intersections are free. This allows a complete filling of the straight channels, in which we observe a nearly uniform distribution. It is interesting to compare this distribution of hexane with the distribution of pentane and butane at high loadings (see figure 4.13). For butane we observe a nearly uniform distribution. For pentane this distribution is less uniform, but the dots are not as clearly clustered as for hexane indicating that the strong localization in the zigzag channels is not present. Recently, this effect has also been found by using FT-Raman spectroscopy and temperature-programmed desorption [165].

Another evidence that the packing efficiency of hexane and heptane are higher than that of other linear alkanes can be obtained by plotting the maximum loading expressed in kg per kg of Silicalite against the number of carbon atoms; see figure 4.15; there is a clear maximum loading for hexane and heptane. Expressed in terms of molecules per unit cell, the maximum loading decreases with increasing carbon number in a monotonous fashion.

4.5 Branched alkanes

Compared to linear alkanes much less experimental data are available on the adsorption of branched alkanes in Silicalite. Adsorption isotherms of isobutane have been reported by Sun *et al.* [136] and Zhu *et al.* [135, 166], for various hexane isomers by Cavalcante and Ruthven [137], and for 2-methylheptane by Eder [160, 162, 163].

Simulations of branched alkanes have been reported in refs. [142, 167]. June *et al.* showed that at infinite dilution the branched alkanes prefer the intersections. These observations were confirmed by the simulations of Smit and co-workers [21, 142]. Here we investigate the sorption behavior of branched alkanes at higher loadings.

As a first approximation, we have assumed that the interaction CH group of the branched alkane with the zeolite is identical to the interaction of a CH_2 group (see table 4.2). Experimentally the heats of adsorption of isobutane have been obtained by several groups, see table 4.4. The data of Zhu *et al.* is significantly higher than the other datasets, which might be due to impurities in the sample [152]. For 2-methylpentane Cavalcante and Ruthven [137] obtained -68 [kJ/mol] Eder and Lercher [160–163] report for 2-methylpentane an heat of adsorption of -90 [kJ/mol]. Figure 4.17 shows that for the 2-methylalkanes our model gives very good results. For isobutane our simulations are in good agreement with the data of Sun *et al.* but deviate significantly from the data of Zhu *et al.*

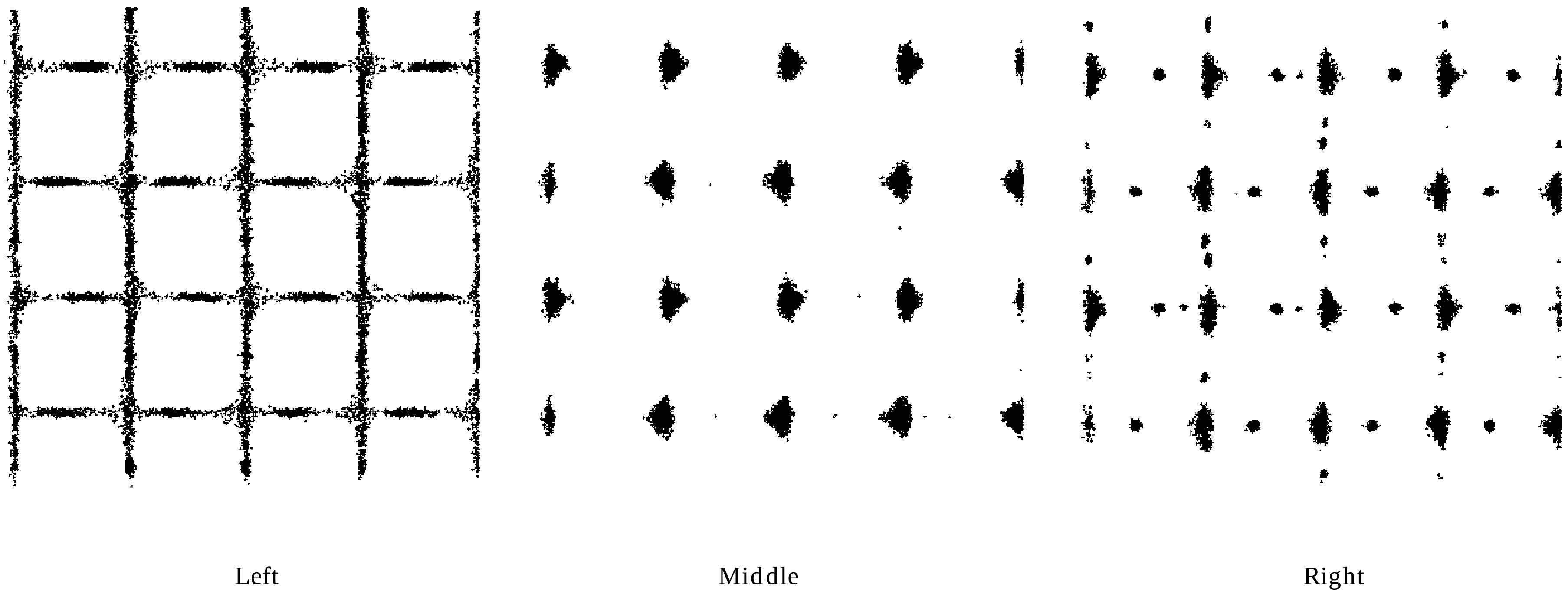

Figure 4.16: Probability distributions of n-butane at 0.1 kPa (left), isobutane at 0.1 kPa (middle) and isobutane at 200 kPa (right) on Silicalite at 300K. The zigzag channels are from the left to the right and the straight channels are perpendicular to the zigzag channels (projection on the x-y plane). These figures were obtained by plotting the centers of mass of the molecules (blue dots) every 200 Monte Carlo cycles until 10000 points were collected.

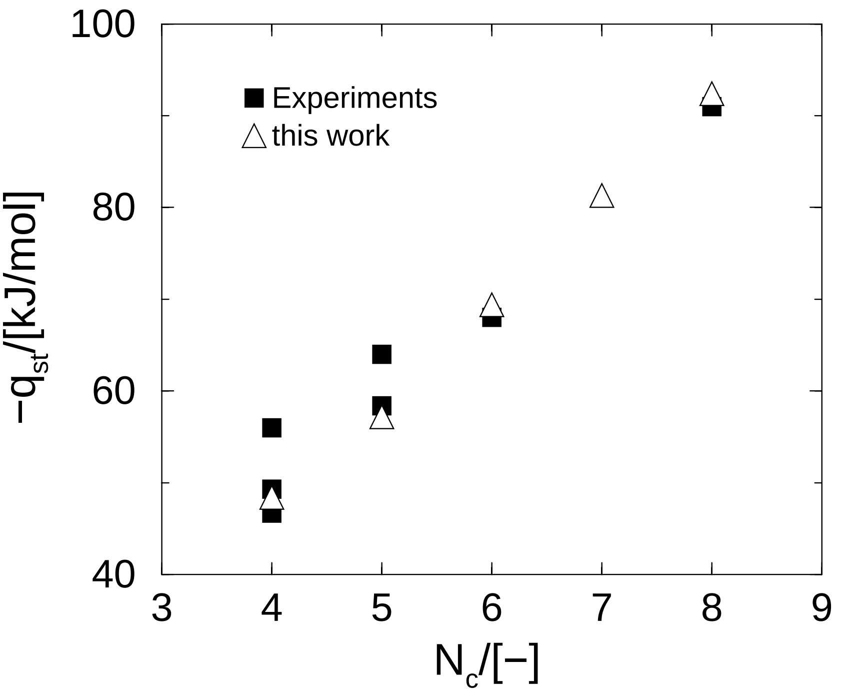

Figure 4.17: Heats of adsorption ($-q_{st}$) as a function of the number of carbon atoms N_c of the branched (2-methyl) alkanes adsorbed in Silicalite.

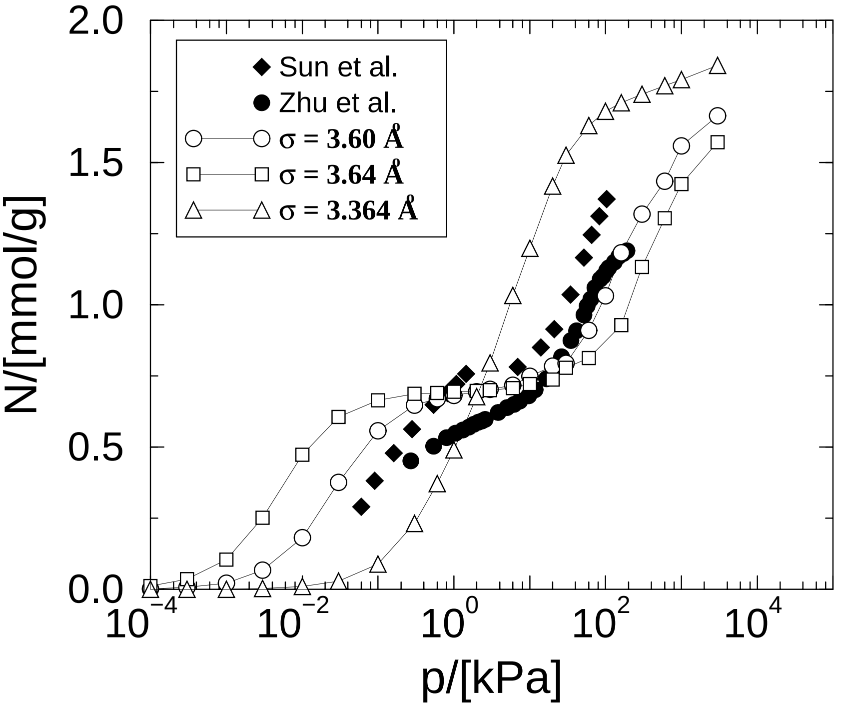

Figure 4.18: Adsorption isotherms of isobutane in Silicalite. Molecular simulations (open symbols) using the models of Vlugt *et al.* [36] (σ = 3.60Å, circles), Smit *et al.* [142] (σ = 3.64Å, squares) and June *et al.* [141] (σ = 3.364Å, triangles), see table 4.1. Experimental data (closed symbols) from Zhu *et al.* [135] (circles) and Sun *et al.* [136] (diamonds).

In figure 4.18, the simulated adsorption isotherm of isobutane is compared with the experimental isotherms of Sun *et al.* [136] and Zhu *et al.* [135]. The agreement is very good. Both the experiments and the simulations show an inflection at a loading of 0.7 [mmol/g], this corresponds to a loading of 4 molecules per unit cell. To investigate this inflection, we have plotted the siting of at a pressure of 0.1 kPa and 200 kPa at 300K and compared this with the siting of butane, see figure 4.16. The differences are striking. Whereas n-butane has an equal probability to be in the straight channel, zigzag channel or intersection, isobutane has a strong preference for the intersection. Let us now compare the siting of isobutane before (low loading, figure 4.16 (middle)) and after (high loading, figure 4.16 (right)) the inflection point in the isotherm. Below a loading of 4 molecules per unit cell, isobutane occupies only the intersections. At a loading of 4 molecules per unit cell, the intersections are fully occupied and to achieve higher loadings, isobutane must also seek residence in the other channels. This, however, is energetically very demanding and requires a significantly higher driving force (pressure) resulting in the inflection point.

It is important to note the Lennard-Jones size parameter $\sigma_{\mathrm{CH_i-O}}$ has a large influence on this inflection. June *et al.* [141] has chosen a rather small value of $\sigma = 3.364$Å, while Smit *et al.* [142] and Schuring *et al.* [168] have used $\sigma = 3.64$Å. The model of June *et al.* has been used by many authors to study the diffusion of hydrocarbons in Silicalite [71, 169–172]. In figure 4.18, we have plotted the isotherm of isobutane for the different models for the alkane-zeolite interactions together with available experimental data. Although the value of σ between the models differs by less than 10%, the differences in the computed isotherms are huge. Furthermore, the model of June *et al.* deviates significantly from the other data and does not reproduce the inflection in the isotherm at a loading of four molecules per unit cell (equivalent to approximately 0.7 mmol/g) [21, 173], while this inflection is present in both other models. This inflection is also not reproduced using the all-atom CVFF model [80, 174].

The simulated isotherms for 2-methylalkanes at 300K temperature are shown in figure 4.19. The continuous lines in this figure are fits of the CBMC simulations using the dual-site Langmuir model which will be discussed in section 4.6.

For the longer branched alkanes adsorption isotherms have been measured by Cavalcante and Ruthven [137] for 2-methylpentane and by Eder and Lercher for 2-methylheptane [160, 162, 163]. In figure 4.20 we compare the experimental data [137] with our simulation results for 2-methylpentane. Considering the fact that we have optimized our parameters for linear alkanes using experimental data at room temperature, the agreement at these elevated temperatures is surprisingly good. This figure also makes clear that the pressures in the experiments were not sufficiently high to observe an inflection. Similar agreement between the experiments of Eder [160, 162, 163] for 2-methylheptane at $T = 372$K and our simulations are observed (see figure 4.21). For the range of pressures studied both simulations and experiments do not exhibit an inflection behavior.

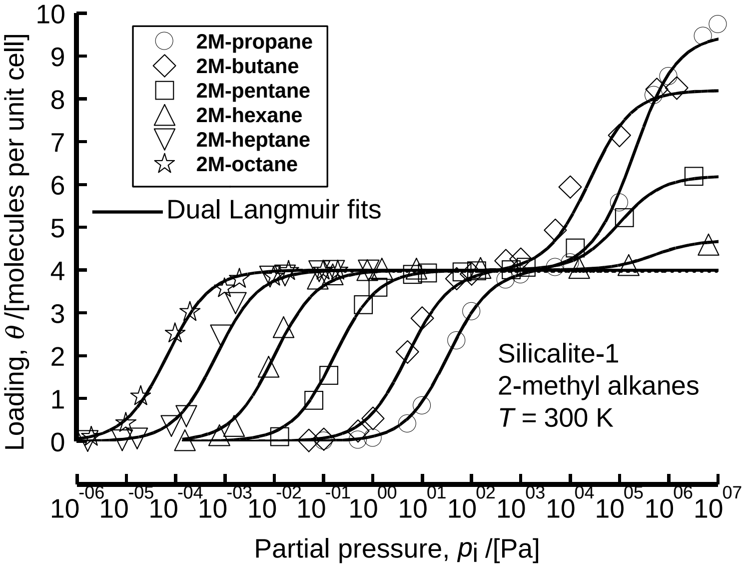

Figure 4.19: Simulated isotherms for branched alkanes in Silicalite at 300 K.

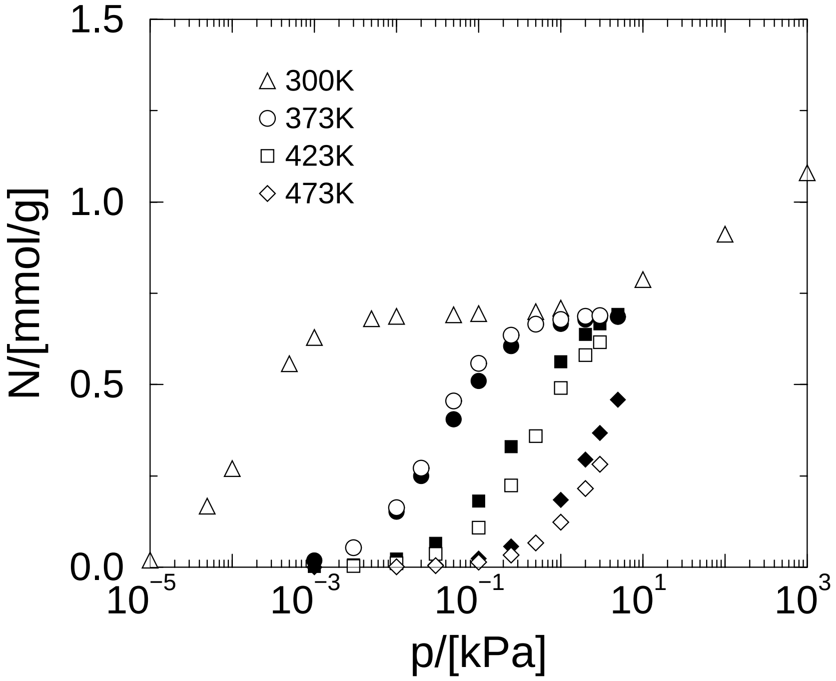

Figure 4.20: Adsorption isotherms of 2-methylpentane in Silicalite at various temperatures.

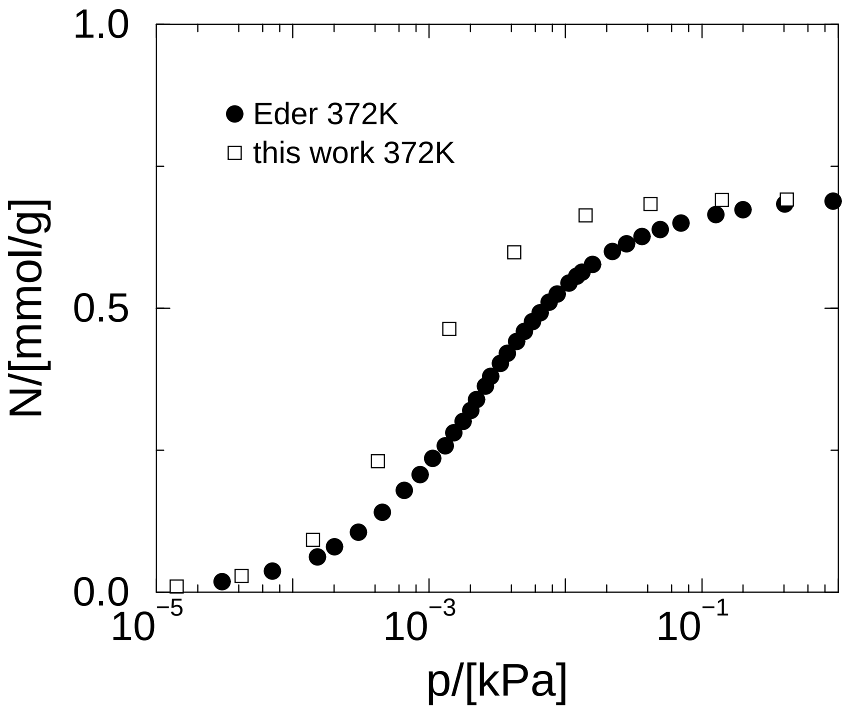

Figure 4.21: Adsorption isotherms of 2-methylheptane in Silicalite.

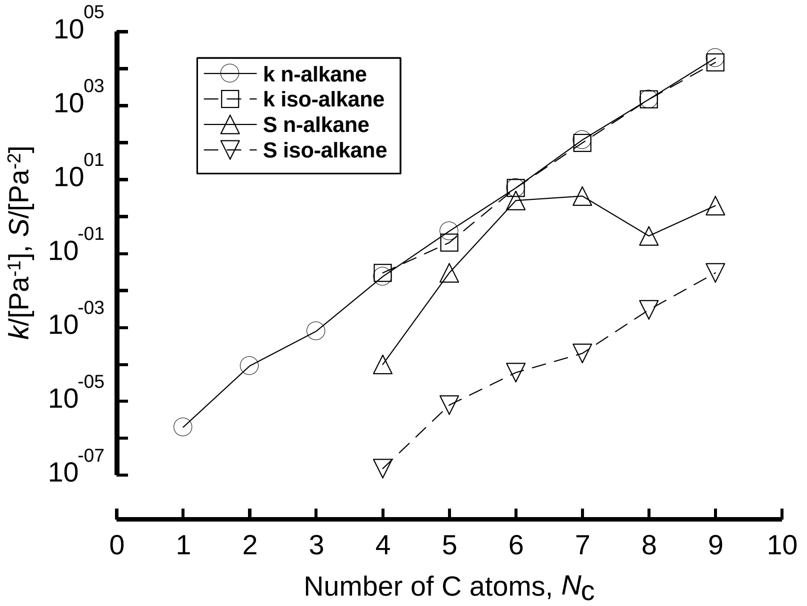

Figure 4.22: Parameters k and S of the dual-site Langmuir model for linear and branched alkanes as a function of the number of carbon atoms.

4.6 Fitting of simulated isotherms with dual-site Langmuir model

The isotherm inflection behavior observed for branched alkanes (see figure 4.19) and for linear alkanes with 6 or more C atoms (see figure 4.10) cannot be modeled using a simple Langmuir isotherm. Sun *et al.* [131,136] have used a 6-parameter virial type equation to fit these isotherms. In this section, we develop a much simpler approach based on the molecular insight obtained from the simulations. From the discussion regarding the inflection behavior of isobutane it becomes clear that one must account for differences in the ease with which a molecule can be adsorbed at the intersections and within the channel interiors. We therefore adopt a dual-site Langmuir model [3,175] for purposes of fitting the isotherms

$$\theta = \frac{\theta_A k_A p}{1 + k_A p} + \frac{\theta_B k_B p}{1 + k_B p} = \frac{(\theta_A k_A + \theta_B k_B)p + (\theta_A + \theta_B) k_A k_B p^2}{1 + (k_A + k_B)p + k_A k_B p^2}, \tag{4.1}$$

where we identify sites A and B, with the respective maximum loading capacities θ_A and θ_B, expressed in molecules per unit cell, p is the partial pressure of the component. The dual-site Langmuir constants for adsorption at the two sites A and B are k_A and k_B (expressed in Pa^{-1}). We take site A to be the one with the higher Langmuir constant. From figures 4.10 and 4.19, it is clear that inflection in Silicalite occurs at a loading of 4 molecules per unit cell and so the maximum capacity of site A, so $\theta_A = 4$. From figures 4.10 and 4.19 we conclude that θ_A should be taken equal to 4 for all (linear and branched) alkanes (θ_A is therefore not used as a fitting parameter). The maximum total loading $\theta_{max} = \theta_A + \theta_B$ for the linear alkanes from the simulations agree with the experimental data of Sun *et al.* [176] (see figure 4.15). In our description of the data we have used the values of θ_{max} corresponding to our simulation results; this is therefore also not a fit parameter. All our CBMC results shown in figures 4.10 and 4.19 were described by fitting the two remaining Langmuir constants k_A and k_B to equation 4.1. The fitted curves describe the simulation results exceedingly well; see figures 4.10 and 4.19. The values of the fit parameters for linear and branched alkanes are presented in figure 4.22 in the form

$$k = \frac{(\theta_A k_B + \theta_B k_B)}{\theta_A}; \qquad S = k_A k_B. \tag{4.2}$$

The fitted parameter k is practically identical for linear and branched alkanes. The S parameter, on the other hand, is about two to three orders of magnitude lower for the branched alkanes as compared to the linear ones. This causes the inflection behavior for branched alkanes to be much more prominent. The information presented in figure 4.22 could be extrapolated to estimate the isotherms for alkanes with higher carbon numbers. We note in passing that the constant $k \times \theta_{max}$ presented in figure 4.22 corresponds remarkably well with the Henry coefficients shown in figure 4.3.

4.7 Conclusions

The Configurational-Bias Monte Carlo technique has been used for simulating the adsorption isotherms for linear and branched (2-methyl) alkanes on Silicalite. The important observations and conclusions arising from our studies are as follows.

- For branched alkanes inflection behavior was observed for all carbon numbers studied, which ranged from 4 to 9. This inflection was found to occur at a loading of 4 molecules per unit cell. Below this loading the branched alkanes are seen to be located predominantly at the intersections of the straight and zigzag channels. To obtain loadings higher

Table 4.3: Parameters for the torsion potential of the branched alkanes (equation 4.4), a CH_3 group connected to a CH group is denoted by CHb_3, the letter i is used to indicate either an CH_3 or CH_2 group, *i.e.* $i = 2, 3$. In case of a CH group the total torsion potential is the sum of two contributions.

	C_0/k_B [K]	C_1/k_B [K]	C_2/k_B [K]	C_3/k_B [K]
CH_i-CH_2-CH-CHb_3	373.0512	919.0441	268.1541	-1737.216
CH_i-CH_2-CH_2-CH	1009.728	2018.446	136.341	-3164.520
CH_i-CH_2-CH_2-CH_i	1009.728	2018.446	136.341	-3164.520

than 4, the branched alkane must seek residence in the channel interiors which is more demanding and therefore requires disproportionately higher pressures; this leads to the inflection behavior.

- Linear alkanes with 6 and more carbon atoms also were found to exhibit inflection behavior. Hexane and heptane show inflection due to commensurate “freezing”; the length of these molecules is commensurate with the length of the zigzag channels. This leads to a higher packing efficiency than for other linear alkanes.

- Available experimental data from the literature confirm the accuracy of the predictions of the CBMC simulations for both linear and branched alkanes. However, in the latter case the number of experimental data are much less as compared to that available for linear alkanes.

- The temperature dependency of the isotherms are also properly modeled by the CBMC simulations.

- For purposes of fitting the CBMC simulated isotherms,the dual-site Langmuir model has been found to provide an excellent description. In this model we distinguish between two sites with differing ease of adsorption: site A, representing the intersections between the straight and zigzag channels and site B, representing the channel interiors.

4.8 Appendix A: Alkane model

In our study we focus on linear alkanes and branched alkanes with a single chain-end branch with the structure $(CH_3)_2$-CH-$(CH_2)_n$-CH_3. The pseudo-atoms in a given chain are assumed to be connected by rigid bonds ($d_{CC} = 1.53$ Å). Bond-bending is modeled by a harmonic potential [88]

$$u^{bend}(\theta_i) = \frac{1}{2}k_\theta(\theta_i - \theta_{eq})^2 \tag{4.3}$$

with $\theta_{eq} = 113°$ and the equilibrium angle for all hydrocarbons and with a force constant equal to $k_\theta = 62500$ K rad^{-2}. Changes in the torsional angles are controlled by [177]:

$$u^{tors}(\phi_i) = C_0 + C_1\cos(\phi_i) + C_2\cos^2(\phi_i) + C_3\cos^3(\phi_i) \tag{4.4}$$

with parameters shown in table 4.3. The *pseudo*-atoms in different molecules, or belonging to the same molecule, but separated by more than three bonds, interact which each other through

a Lennard-Jones potential

$$u_{ij}^{lj} = \begin{cases} 4\epsilon_{ij}\left[\left(\frac{\sigma_{ij}}{r_{ij}}\right)^{12} - \left(\frac{\sigma_{ij}}{r_{ij}}\right)^{6}\right] & r_{ij} \leq r_{cut} \\ 0 & r_{ij} > r_{cut} \end{cases} \tag{4.5}$$

where r_{ij} is the distance between sites i and j and r_{cut} the cut-off radius. The Lennard-Jones parameters used are shown in table 4.2.

4.9 Appendix B: Discussion of the experimental data

4.9.1 Heats of adsorption

In our model we have used the heats of adsorption and the Henry coefficients to fit our model. Unfortunately, these is significant scatter in the experimental data which makes it difficult to refer to the literature for the experimental data. In our comparison with the simulation results, we have made a selection of the experimental data. This appendix provides a short justification of this selection. The available experimental data for the heats of adsorption are summarized in table 4.4.

The experimental data for methane are in the range −18, −22 [kJ/mol]. In our simulations we have used −20 [kJ/mol]. For ethane the experimental data on pure Silicalite converge to a value of −31 [kJ/mol] and for propane to a value of −40 [kJ/mol]. For the longer alkanes we have used for butane −50 [kJ/mol]. For pentane the data scatter significantly. The data reported by Sun *et al.* [131] suggests that the heat of adsorption of pentane is lower than the heat of adsorption of hexane also the data in refs. [126, 127, 178] do not give a consistent result. We have used −60 [kJ/mol] which is consistent with the data for butane and hexane. For hexane the experimental data agree much better. These data converge well to a value of −71 [kJ/mol]. For the longer alkanes only a few data have published which makes it difficult to compare the consistency. We have used for heptane −83 [kJ/mol], for octane −92 [kJ/mol], for nonane −108 [kJ/mol], and for decane −120 [kJ/mol].

Table 4.4: Experimental heat of adsorption of various alkanes (q_{st}) in Silicalite / ZSM5.

T/[K]	Si / Al ratio	$-q_{st}$/[kJ/mol]	ref.
		methane	
298	300	20.9	[179]
300	∞	18.1	[180, 181]
300	∞ (Linde S-115)	20.4	[149]
300	∞	20.5	[182]
300	∞	20.0	[151]
300	∞	20.9	[183, 184]
300	∞	20	[136]
300	$>$ 3000	18.6	[135]
300	$>$ 1300	18.0	[166]
300	52	28	[185]
300	∞	18.7	[186]
300	∞	20.9	[187]
423	∞	22.5	[188]
		ethane	
293	34	40.0	[178]
293	130	45	[178]
298	∞	30.5	[189]
298	300	31.1	[179]
300	∞	31.1	[187]
300	30 (Na,ZSM5)	38.0	[190]
300	∞ (Linde S-115)	32.8	[149]
300	∞	29.9	[182]
300	∞	31	[17]
300	∞	33	[136]
300	$>$ 3000	30.7	[135]
300	$>$ 1300	34.4	[166]
301	∞	34	[191]
318	1230	30	[192]
333	132	30	[128]
		propane	
293	34	44.5	[178]
293	130	46.5	[178]
298	∞	38	[189]
298	300	41.4	[179]
300	∞	40.7	[182]
300	∞	40	[136]
300	$>$ 3000	40.9	[135]
300	$>$ 1300	45.9	[166]
300	∞	42.2	[193]
318	1230	40	[192]
318	135 (Na,H-ZSM5)	36.7	[192]
323	35	46	[162]
325	∞ (Linde S-115)	39.9	[149]
333	132	39	[128]
423	∞	36.5	[188]

Table 4.4 continued ...			
T/[K]	Si / Al ratio	$-q_{st}$/[kJ/mol]	ref.
		butane	
293	34	49.5	[178]
300	∞	48.7	[194]
300	∞	51	[17]
300	∞	50.4	[182]
300	∞	51	[136]
300	> 3000	53.0	[135]
300	> 1300	56.1	[166]
301	∞	54.8	[191, 195, 196]
303	132	50	[128]
323	35	58	[162]
325	∞ (Linde S-115)	48.3	[149]
400	10 (Na,ZSM5)	55	[197]
400	10 (H,ZSM5)	53	[197]
400	24 (Na,ZSM5)	52	[197]
400	24 (H,ZSM5)	50	[197]
400	44 (Na,ZSM5)	50	[197]
400	∞	48	[197]
400	380	37.8	[134]
423	∞	49.5	[188]
		2-methylpropane	
300	∞	56	[136]
300	∞	49.3	[182]
300	> 3000	46.7	[135]
300	> 1300	65.6	[166]
301	∞	49.0	[191]
323	35	52	[162]
400	380	50.2	[198]
423	∞	51	[188]
		pentane	
293	34	54	[178]
300	∞	41.8	[131]
303	∞	64.5	[126, 127]
323	35	70	[162]
400	380	50–56	[134]
		2-methylbutane	
323	35	64	[162]
400	380	58.4	[198]
		hexane	
300	∞	71	[2]
300	∞	71.5	[124, 199]
300	∞	71	[17]
300	∞	70.5	[131]
318	135 (Na,H-ZSM5)	71	[192]
323	35	82	[162]
333	132	60	[128]
373	∞	72	[161]
400	380	71–78	[134]

Table 4.4 continued ...			
T/[K]	Si / Al ratio	$-q_{st}$/[kJ/mol]	ref.
2-methylpentane			
323	35	90	[162]
400	380	61.5	[198]
400	∞	68	[137]
heptane			
300	∞	83.4	[131]
303	∞	84.5	[126, 127]
373	∞	84	[161]
400	380	84–88	[134]
octane			
300	∞	92.1	[131]
373	∞	96	[161]
400	380	89.4	[134]
nonane			
300	∞	107.7	[131]
373	∞	107	[161]
decane			
300	∞	112	[17]
300	∞	120.5	[131]
303	∞	110.5	[124]

4.9.2 Henry coefficients

Adsorption isotherms of methane in Silicalite have been determined by several groups [149, 151, 182, 184, 186, 200, 201]. At low pressures the data from Hufton and Danner [182], Yamazaki *et al.* [184], Ott *et al.* [201], Rees *et al.* [151], and Golden and Sircar [186] are in very good agreement. From these adsorption isotherms we have determined the Henry coefficients and we have used $H = 7.5 \times 10^{-6}$ [mmol / g / Pa] as experimental value for the Henry coefficient.

For ethane, the data of Hufton and Danner [182, 202], Richard and Rees [128], and Hampson and Rees [189] are in good agreement with each other. We have combined the low pressure data of Hufton and Danner [182, 202], Richard and Rees [128], and Hampson and Rees [189]. Fitting all these data with equal weight yielded a Henry coefficient $H = 1.4 \times 10^{-4}$ [mmol / g / Pa]. This is consistent with the values reported in refs. [182, 189].

The adsorption isotherms of propane of Abdul-Rehman *et al.* [149] and Hampson and Rees [189] are in good agreement with each other. The data of Richard and Rees [128] deviate slightly. Note that the isotherm of Richard and Rees was measured at a temperature of 291.5K, while the other data are taken at 300 K. This temperature difference can explain the difference between the data sets. In our calculations, we have used $H = 1.25 \times 10^{-3}$ [mmol / g / Pa].

For butane isotherms have been measured by Thamm [195], Stach *et al.* [124], Richard and Rees [128], Abdul-Rehman [149], and Shen and Rees [194]. These isotherms gave a Henry coefficient of approximately 1.5×10^{-2} [mmol / g / Pa].

Adsorption isotherms of pentane in Silicalite have been measured by Rakhmatkariev *et al.* [126] and Dubinin *et al.* [127]. Dubinin *et al.* [127] report data at low pressures yielding a Henry coefficient of 0.187 [mmol / g / Pa].

For hexane adsorption isotherms have been measured by Stach *et al.* [124] and Richard and Rees [128]. We have used the average of the two Henry coefficients, namely 3.05 [mmol / g / Pa]. For the longer alkanes we could not find sufficiently reliable isotherms at low pressures to compute a Henry coefficient at room temperature.

Chapter 5

Adsorption of mixtures of alkanes in Silicalite*

5.1 Introduction

In the previous chapter we have shown that our model gives a satisfactory description of the adsorption isotherms of pure n-alkanes and 2-methylalkanes for C_4–C_9 on Silicalite. In this chapter, we investigate the mixture isotherms of various alkane isomers. Experimentally, the measurement of an isotherm is more complicated for mixtures than for pure components. One not only has to measure the weight increase of the zeolite as a function of pressure, but also the change in composition of the gas mixture. To the best of our knowledge, only adsorption isotherms of mixtures of short alkanes have been measured [149, 205]. In ref. [148] we have shown that for mixtures of ethane and methane our model gives a reasonable prediction of the mixture isotherms. Here we concentrate on the mixtures of C_4 through C_7 isomers.

Using the Maxwell-Stefan theory, we will closer investigate the influence of isotherm inflection on the diffusivity. When we assume that the Maxwell-Stefan diffusion coefficient (sometimes also called the corrected diffusion coefficient) is independent of the loading, the loading dependence of the conventional Fick diffusion coefficient will be completely determined by the adsorption isotherm. We will demonstrate that on the basis of mixture isotherms we can predict the membrane permeation efficiency without having to know the diffusion coefficients exactly.

5.2 Mixture Isotherms

In the previous chapter, we have focussed on adsorption of pure linear and branched alkanes on Silicalite and found that our model is able to reproduce experimental data very well. Here, we will use the same model and simulation technique to study mixtures. In figures 5.1–5.4, the mixture isotherms of C_4, C_5, C_6, and C_7 isomers are presented. We focus on a mixture of a linear alkane and the 2-methyl isomer with a 50%-50% mixture in the gas phase. Details about these simulations can be found in chapter 4. For all mixtures we see the following trends. At low pressure the linear and branched alkanes adsorb independently. The adsorption of the two components is proportional to the Henry coefficients of the pure components. At a total mixture loading of 4 molecules per unit cell the adsorption of the branched alkanes reaches a maximum and decreases with increasing pressure. For C_5, C_6 and C_7 mixtures, the branched alkane is completely removed from the zeolite. The adsorption of the linear alkanes however increases with increasing pressure till saturation is reached.

*This chapter is based on refs. [36, 203, 204].

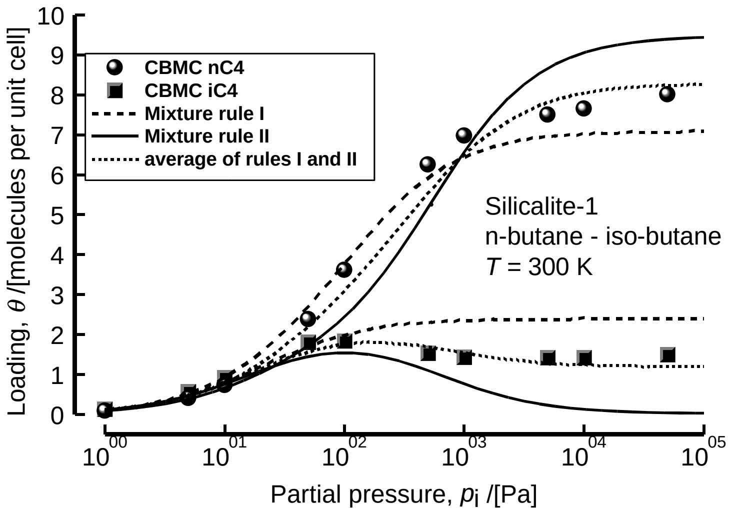

Figure 5.1: Adsorption isotherm of a 50%-50% mixture of butane and isobutane in Silicalite.

It is interesting to investigate the reasons why the branched alkanes are squeezed out by the linear alkanes at high pressures. For the C_6 and C_7 isomers the Henry coefficient of the branched alkanes is slightly larger. One would therefore expect that these branched alkanes would adsorb better. This is indeed observed at low pressures; at high pressures, however, other considerations have to be taken into account. We will explain this on the basis of the mixture behavior for C_6 isomers. As can been seen from figure 5.3 the total loading exhibits inflection behavior at $\theta_1 + \theta_2 = 4$. Until this loading there is no competition between C_6 and 2-methylpentane (2MP) and both are almost equally easily adsorbed. Examination of the probability distributions of the linear and branched isomers 100 Pa reveals that all the 2MP molecules are located at the intersections between the straight channels and the zigzag channels whereas C_6 are located everywhere (see ref. [203]). A further important aspect to note is orientation of the 2MP molecules; these have their heads (*i.e.* the branched end) at the intersections and their tails sticking out into the zigzag or straight channels. The C_6 molecules fit nicely into both straight and zigzag channels [20]; these molecules have a higher "packing efficiency" than 2MP. As the pressure is increased beyond 100 Pa, it is more efficient to obtain higher loadings by "replacing" the 2MP with C_6; this entropic effect is the reason behind the curious maximum in the 2MP isotherm. A similar explanation holds for the C_5 and C_7 isomers. To further test our hypothesis that because of entropic reasons the branched alkanes are squeezed out the zeolite, we have performed a simulation in which we have removed the attractive part of the Lennard-Jones potential interacting between the hydrocarbon atoms and hydrocarbon-zeolite atoms. In such a system with only "hard-sphere" interactions there is no energy scale involved and the only driving force is entropy. Also in this system we have observed that the branched alkane is squeezed out at high pressures, which proves that this squeezing out of the branched alkanes by the linear isomer is an entropic effect.

There is an important advantage in being able to describe the inflection behavior accurately with the help of the dual-site Langmuir model (DSL); this is because it would then be possible to predict the mixture isotherm from only pure component data. For single components, we have

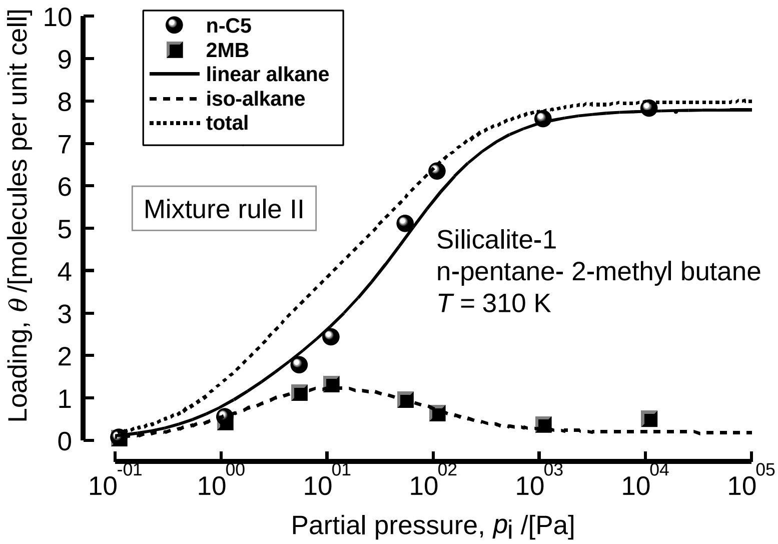

Figure 5.2: Adsorption isotherm of a 50%-50% mixture of pentane and 2-methylbutane in Silicalite.

shown in section 4.6 that the DSL gives a good description for the adsorption isotherms of linear and branched alkanes on Silicalite. Here, we consider the case that there are two adsorption sites in the zeolite. There are two ways to set up the mixture rule. In the first approach (I) we apply this rule to each of the two sites A and B separately. For each site we apply the multicomponent extension of the Langmuir isotherm [3]; for a mixture of components 1 and 2, therefore, this rule yields:

$$\begin{aligned}\theta_1 &= \frac{\theta_{A1}k_{A1}p_1}{1+k_{A1}p_1+k_{A2}p_2}+\frac{\theta_{B1}k_{B1}p_1}{1+k_{B1}p_1+k_{B2}p_2}\\ \theta_2 &= \frac{\theta_{A2}k_{A2}p_2}{1+k_{A1}p_1+k_{A2}p_2}+\frac{\theta_{B2}k_{B2}p_2}{1+k_{B1}p_1+k_{B2}p_2}\end{aligned} \tag{5.1}$$

where k_{Ai} and k_{Bi} are the Langmuir constants for species i for sites A and B, p_i is the partial pressure of the component i in the gas phase. We expect this mixture scenario to hold when each of the two components 1 and 2 is present in both sites.

The second scenario (II) is to apply the mixture rule to the combination of sites (A+B). This scenario is appropriate to situations in which one of the components is excluded from one particular site (say B); therefore we set up the mixing rule for the total of (A+B), *i.e.* the entire zeolite. To derive this mixing rule, the most convenient starting point is the right equality of equation 4.1 and the guidelines outlines in the book of Ruthven [3]. This yields for a two-component system the following set of equations

$$\begin{aligned}\theta_1 &= \frac{(\theta_{A1}k_{A1}+\theta_{B1}k_{B1})p_1+(\theta_{A1}+\theta_{B1})k_{A1}k_{B1}p_1^2}{1+(k_{A1}+k_{B1})p_1+k_{A1}k_{B1}p_1^2+(k_{A2}+k_{B2})p_2+k_{A2}k_{B2}p_2^2}\\ \theta_2 &= \frac{(\theta_{A2}k_{A2}+\theta_{B2}k_{B2})p_2+(\theta_{A2}+\theta_{B2})k_{A2}k_{B2}p_2^2}{1+(k_{A1}+k_{B1})p_1+k_{A1}k_{B1}p_1^2+(k_{A2}+k_{B2})p_2+k_{A2}k_{B2}p_2^2}\end{aligned} \tag{5.2}$$

There are also some qualitative differences between the various alkanes. The maximum in the

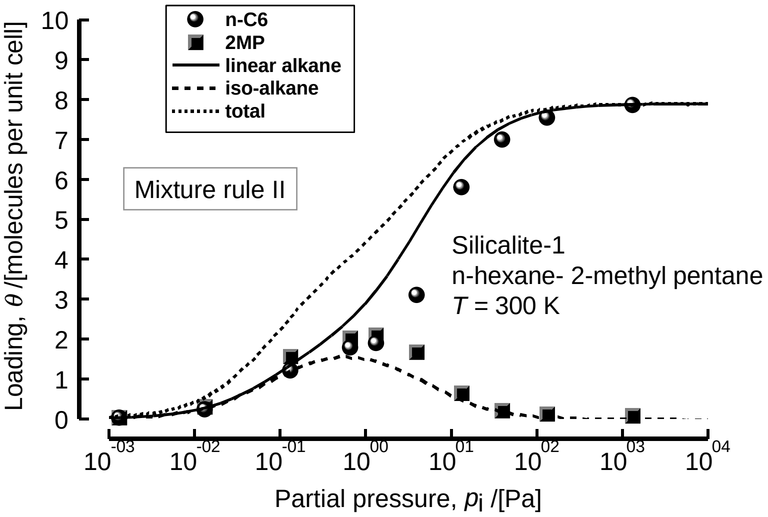

Figure 5.3: Adsorption isotherm of a 50%-50% mixture of hexane and 2-methylpentane in Silicalite.

isotherm of isobutane in the butane-isobutane mixture is very small and at saturation the ratio of the loadings of butane and isobutane is approximately 5.6:1 (see figure 5.1). For the pentane isomers the maximum is more pronounced and at saturation the concentration of the branched alkane is much lower, about one-sixth that of the linear alkane (see figure 5.2). For the hexane isomers at maximum loading the branched alkane is completely squeezed out of the zeolite. For the heptane isomers a table-mountain maximum is observed (see figure 5.4); here too the branched alkane is completely squeezed out at high pressures.

We see from figures 5.2–5.4 that the simulated isotherms conform very well to the mixture rule II based on the dual-site Langmuir model. For alkanes with carbon atoms in the 5-7 range, we need to set up the mixture rule considering the total Silicalite matrix (including sites A and B) as one entity. This is because the branched alkanes do not easily occupy site B (channel interiors) and for some pressure range the channel interiors are completely devoid of the branched isomers. The simulated isotherm for the 50%-50% mixture of butane-isobutane behaves differently, however. Neither mixture rule, I or II, is completely successful. An average of the two mixture rules, on the other hand, is very successful.

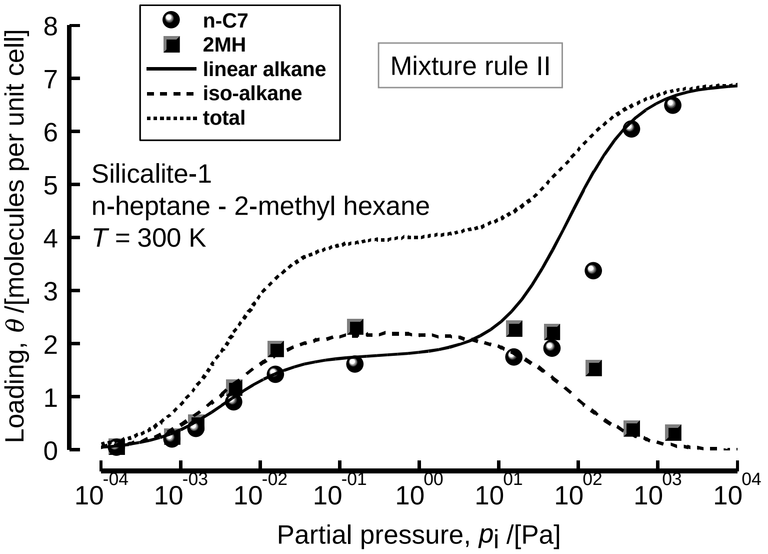

Figure 5.4: Adsorption isotherm of a 50%-50% mixture of heptane and 2-methylhexane in Silicalite.

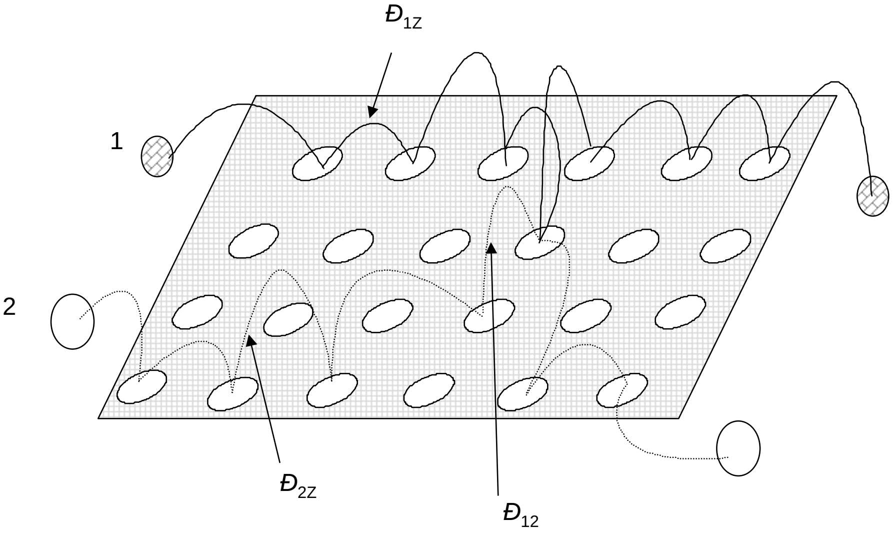

Figure 5.5: Pictorial representation of the Maxwell-Stefan diffusivities.

5.3 Consequences for Diffusion

5.3.1 The Maxwell-Stefan theory for zeolite diffusion

Using the Maxwell-Stefan theory for microporous diffusion, the following expression can be derived for diffusion of species i in a zeolite [206, 207]:

$$-\frac{1}{RT}\frac{d\mu_i}{dz} = \sum_{j=1}^{j=n} \frac{\theta_j}{\theta_{max}} \frac{u_i - u_j}{Đ_{ij}} + \frac{u_i}{Đ_{iZ}};\ i = 1, 2, \cdots, n \tag{5.3}$$

where $-d\mu_i/dz$ is the force acting on species i tending to move it within the zeolite at a velocity u_i, $Đ_{iZ}$ is the Maxwell-Stefan diffusivity describing the interaction between component i and the zeolite (Z), and $Đ_{ij}$ is the Maxwell-Stefan describing the interchange between components i and j within the zeolite structure. The $Đ_{iZ}$ are also called the corrected diffusivity in the literature [3]. Figure 5.5 is a pictorial representation of the three Maxwell-Stefan diffusivities describing diffusion of a binary mixture consisting of species 1 and 2. Procedures for estimation of the $Đ_{iZ}$ and the interchange diffusivity $Đ_{ij}$ are discussed by Krishna in refs. [206, 207]. If there is no possibility of interchange between species 1 and 2, the first term on the right side of equation 5.3 can be ignored. Writing equation 5.3 in terms of the diffusion fluxes N_i

$$N_i = \rho\theta_i u_i \tag{5.4}$$

we get

$$-\frac{\theta_i}{RT}\frac{d\mu_i}{dz} = \sum_{j=1}^{j=n} \frac{\theta_j N_i - \theta_i N_j}{\rho\theta_{max}Đ_{ij}} + \frac{N_i}{\rho Đ_{iZ}};\ i = 1, 2, \cdots, n \tag{5.5}$$

where θ_i is the molecular loading within the zeolite, expressed in molecules per unit cell, θ_{max} is the maximum molecular loading, $\theta_{max} = (\theta_A + \theta_B)$, and ρ represents the number of unit cells per m^3 of Silicalite.

The chemical potential gradients are related to the gradients in the component loadings by

$$\frac{\theta_i}{RT}\frac{d\mu_i}{dz} = \sum_{j=1}^{j=n} \Gamma_{ij}\frac{d\theta_j}{dz};\ \Gamma_{ij} = \frac{\theta_i}{p_i}\frac{\partial p_i}{\partial \theta_j};\ i, j = 1, 2, \cdots, n \tag{5.6}$$

where we have defined a matrix of thermodynamic correction factors $[\Gamma]$. The elements Γ_{ij} of this matrix can be determined from a knowledge of the sorption isotherms. Combining these equations we can write down an explicit expression for the fluxes N_i using n-dimensional matrix notation

$$(N) = -\rho\,[B]^{-1}\,[\Gamma]\,\frac{d\,(\theta)}{dz} \tag{5.7}$$

where the elements of the matrix $[B]$ are

$$B_{ii} = \frac{1}{Đ_{iZ}} + \sum_{j \neq i} \frac{\theta_j}{Đ_{ij}} \frac{1}{\theta_{max}};\ B_{ij} = -\frac{\theta_i}{Đ_{ij}} \frac{1}{\theta_{max}}\ \ (i \neq j) \tag{5.8}$$

The more commonly used Fick diffusivity matrix is defined as

$$(N) = -\rho\,[D]\,\frac{d\,(\theta)}{dz} \tag{5.9}$$

Comparing these equations we obtain the following inter-relation between the Fick and the Maxwell-Stefan diffusivities

$$[D] = [B]^{-1} [\Gamma] \tag{5.10}$$

Since the thermodynamic correction factor matrix $[\Gamma]$ is generally non-diagonal, the matrix of Fick diffusivities is also generally non-diagonal. Generally speaking the Maxwell-Stefan diffusivities $Đ_{iZ}$ are better behaved than the elements of Fick diffusivity matrix $[D]$. The latter diffusivities are strongly influenced by the thermodynamic non-idealities in the system. In this work we examine, in turn, the influence of $[\Gamma]$ on the diffusion behavior of single components and binary mixtures in Silicalite for which the isotherms are described by the dual-site Langmuir model.

5.3.2 Diffusion of a single component in Silicalite

For single component diffusion equations 5.5 and 5.8 degenerate to their scalar forms

$$\Gamma = \frac{\theta}{p}\frac{\partial p}{\partial \theta} \tag{5.11}$$

and

$$D = \Gamma Đ \tag{5.12}$$

For the DSL model isotherm, the thermodynamic factor can be determined by analytic differentiation of equation 4.1; the result is

$$\begin{aligned}\Gamma \;=\; & \frac{\left[1 + (k_A + k_B)\,p + k_A k_B p^2\right]^2}{\left[(\theta_A k_A + \theta_B k_B) + 2\theta_{max} k_A k_B p\right]\left[1 + (k_A + k_B)\,p + k_A k_B p^2\right]}\frac{\theta}{p} \\ - & \left[(\theta_A k_A + \theta_B k_B)\,p + \theta_{max} k_A k_B p^2\right]\left[(k_A + k_B) + 2k_A k_B p\right]\frac{\theta}{p}\end{aligned} \tag{5.13}$$

This correction factor shows two extrema: a maximum at the inflection point $\theta_A = 4$ and a minimum at a loading $\theta_A < \theta < \theta_B$. This behavior is illustrated for adsorption of benzene on Silicalite at temperatures of 303K and 323K; see figure 5.6. Since the Fick diffusivity is proportional to the thermodynamic factor, it can be expected to also exhibit two extrema. This is indeed verified by the experimental data of Shah *et al.* [208] for Fick diffusivity at 303K and 323K; see figure 5.6. The Maxwell-Stefan diffusivities, calculated from equation 5.12 are seen to be practically constant, emphasizing the importance of thermodynamic correction factors on the diffusion behavior.

5.3.3 Diffusion of binary mixtures

For diffusion of a binary mixture in Silicalite equations 5.5 and 5.8 reduce to

$$(N) = -\rho\,[D]\,\frac{d\,(\theta)}{dz}; \quad [D] = \begin{bmatrix} \frac{1}{Đ_{1Z}} + \frac{\theta_2}{Đ_{12}}\frac{1}{\theta_{max}} & -\frac{\theta_1}{Đ_{12}\theta_{max}} \\ -\frac{\theta_2}{Đ_{12}\theta_{max}} & \frac{1}{Đ_{2Z}} + \frac{\theta_2}{Đ_{12}}\frac{1}{\theta_{max}} \end{bmatrix}^{-1} \begin{bmatrix} \Gamma_{11} & \Gamma_{12} \\ \Gamma_{21} & \Gamma_{22} \end{bmatrix} \tag{5.14}$$

The interchange mechanism is often ignored and the following formulation used

$$(N) = -\rho\,[D]\,\frac{d\,(\theta)}{dz}; \; [D] = \begin{bmatrix} Đ_{1Z} & 0 \\ 0 & Đ_{2Z} \end{bmatrix} \begin{bmatrix} \Gamma_{11} & \Gamma_{12} \\ \Gamma_{21} & \Gamma_{22} \end{bmatrix} \tag{5.15}$$

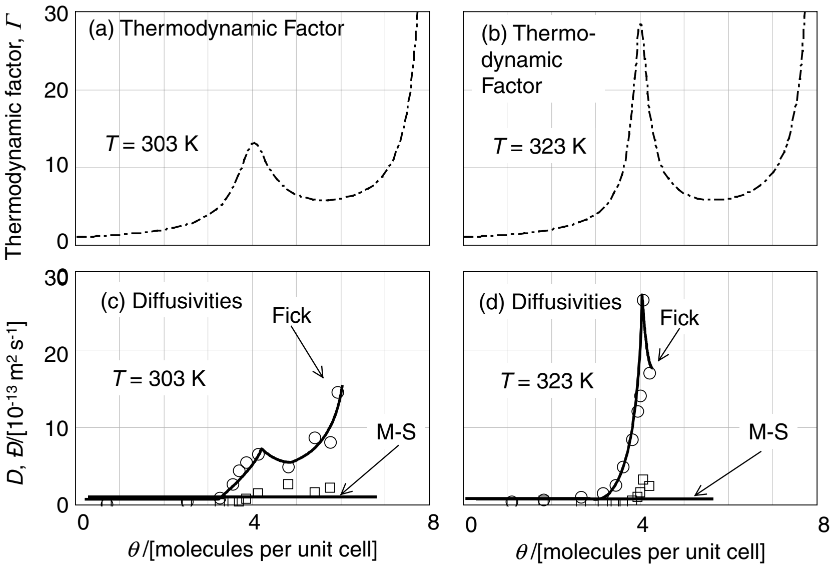

Figure 5.6: Thermodynamic correction factors (top) and diffusivities (bottom) for diffusion of benzene in Silicalite at (left) 303K and (right) 323K. The experimental diffusivity data are from Shah *et al.* [208].

Recent work of Van de Graaf *et al.* [209] and Kapteijn *et al.* [210] has shown that for diffusion of binary mixtures in Silicalite, the complete Maxwell-Stefan formulation, equation 5.14, taking interchange into account provides a much better description of binary permeation experimental results across a Silicalite membrane than with a model ignoring the interchange mechanism (portrayed by $Đ_{12}$).

To calculate the Γ_{ij} we need the sorption isotherms for mixtures. However, experimental data on sorption isotherms of mixtures are scarce. To illustrate the influence of Γ_{ij} on the diffusion we consider a mixture of n-hexane (n-C_6) and 3-methylpentane (3MP) and use the Configurational-Bias Monte Carlo (CBMC) simulation technique described earlier (see chapters 2 and 4) to generate the pure component and 50%-50% mixture isotherm data at 362K. The results of these CBMC simulations are shown in figure 5.7. The continuous lines in 5.7 are DSL fits of the pure component isotherms (parameter values are given in the caption). The mixture isotherms are well represented by the DSL mixture model (equation 5.2, mixing rule II) as can be seen in figure 5.7 wherein the mixture isotherms are predicted using only pure component data. The branched alkane 3MP exhibits a maximum with respect to molecular loading within the Silicalite structure, this is similar for a mixture of 2MP and hexane.

The four elements of Γ_{ij} can be obtained by analytic differentiation of equation 5.6. The result is

$$[\Gamma] = \frac{\begin{bmatrix} A_3 (B_2 - \theta_2 B_4)/p_1 & A_3 \theta_1 B_4 / p_1 \\ B_3 \theta_2 A_4 / p_2 & B_3 (A_2 - \theta_1 A_4)/p_2 \end{bmatrix}}{A_2 B_2 - \theta_1 A_4 B_2 - \theta_2 A_2 B_4} \tag{5.16}$$

where

$$\begin{aligned}
A_2 &= (\theta_{1A}k_{1A} + \theta_{1B}k_{1B}) + 2(\theta_{1A} + \theta_{1B})\,k_{1A}k_{1B}p_1 \\
A_3 &= (\theta_{1A}k_{1A} + \theta_{1B}k_{1B})\,p_1 + (\theta_{1A} + \theta_{1B})\,k_{1A}k_{1B}p_1^2 \\
A_4 &= (k_{1A} + k_{1B}) + 2k_{1A}k_{1B}p_1 \\
B_2 &= (\theta_{2A}k_{2A} + \theta_{2B}k_{2B}) + 2(\theta_{2A} + \theta_{2B})\,k_{2A}k_{2B}p_2 \\
B_3 &= (\theta_{2A}k_{2A} + \theta_{2B}k_{2B})\,p_2 + (\theta_{2A} + \theta_{2B})\,k_{2A}k_{2B}p_2^2 \\
B_4 &= (k_{2A} + k_{2B}) + 2k_{2A}k_{2B}p_2
\end{aligned} \tag{5.17}$$

To demonstrate the consequences of the influence of Γ_{ij} on diffusion, consider the permeation of hydrocarbon isomers across a Silicalite membrane (figure 5.8). To obtain the values of the permeation fluxes N_i we need to solve the set of two coupled partial differential equations:

$$\frac{\partial(\theta)}{\partial t} = \frac{\partial}{\partial z}\left([D]\,\frac{\partial(\theta)}{\partial z}\right) \tag{5.18}$$

subject to the initial and boundary conditions

$$t = 0;\ 0 \le z \le \delta;\ \theta_{iz} = 0 \tag{5.19}$$

$$t > 0;\ z = 0;\ i = 1,2 \tag{5.20}$$

$$\theta_{i0} = \frac{(\theta_{iA}k_{iA} + \theta_{iB}k_{iB})\,p_{i0} + (\theta_{iA} + \theta_{iB})\,k_{iA}k_{iB}p_{i0}^2}{1 + (k_{1A} + k_{1B})\,p_{10} + k_{1A}k_{1B}p_{10}^2 + (k_{2A} + k_{2B})\,p_{20} + k_{2A}k_{2B}p_{20}^2}$$

The set of two coupled partial differential equations (equation 5.18) subject to the initial and boundary conditions (equations 5.19 and 5.20) were solved using the method of lines [211] to determine the fluxes, as described in ref. [212]. In the calculations presented here we assume that the pure component Maxwell-Stefan diffusivities are identical for the isomers, *i.e.* $Đ_{1Z} = Đ_{2Z}$; this assumption is a conservative one from the viewpoint of separation of the isomers as we expect the branched isomer to have a lower mobility within the Silicalite structure. The simulations were carried out with the complete Maxwell-Stefan model for [D], *i.e.* equation 5.14. Since the interchange coefficient $Đ_{12}$ has a value intermediate between $Đ_{1Z}$ and $Đ_{2Z}$ [213] we must also have $Đ_{1Z} = Đ_{2Z} = Đ_{12}$. A further point to note is that in the calculation of the fluxes we have made the assumption that the Maxwell-Stefan diffusivities are independent of the loading. Though this assumption is not always true (see refs. [214, 215]), the values of the ratio of fluxes, *i.e.* selectivity for separation, is not expected to be influenced by this assumption.

The transient fluxes for the C_6 isomers are presented in figure 5.9 in dimensionless form. Examination of the transient fluxes reveals a slight maximum in the flux of the branched alkanes; this maximum is a direct consequence of the corresponding maximum in mixture isotherms; see figure 5.7. The ratio of the fluxes of n-C_6 and 3MP is found to be 32. There is some evidence in the published literature for permeation of a 50%-50% mixture of n-C_6 and 3MP at 362K across a Silicalite membrane [216] to suggest that this high selectivity values for separation of the C_6 isomers can be realized in practice. These high selectivities are entirely due to the strong inflection observed for the branched alkane; this is described by a much lower value of the Henry coefficient k_B for site B than for the linear alkane. If both sites A and B had the same sorption capability, then the selectivity for the separation would be close to unity. Another important point to note is that in the membrane permeation experiment we must ensure that the values of the upstream partial pressures of the hydrocarbon isomers are high enough (say higher than 5 kPa) to ensure that the branched alkane is virtually "excluded". More details about temperature and pressure dependence of the permeation selectivity can be found in ref. [203].

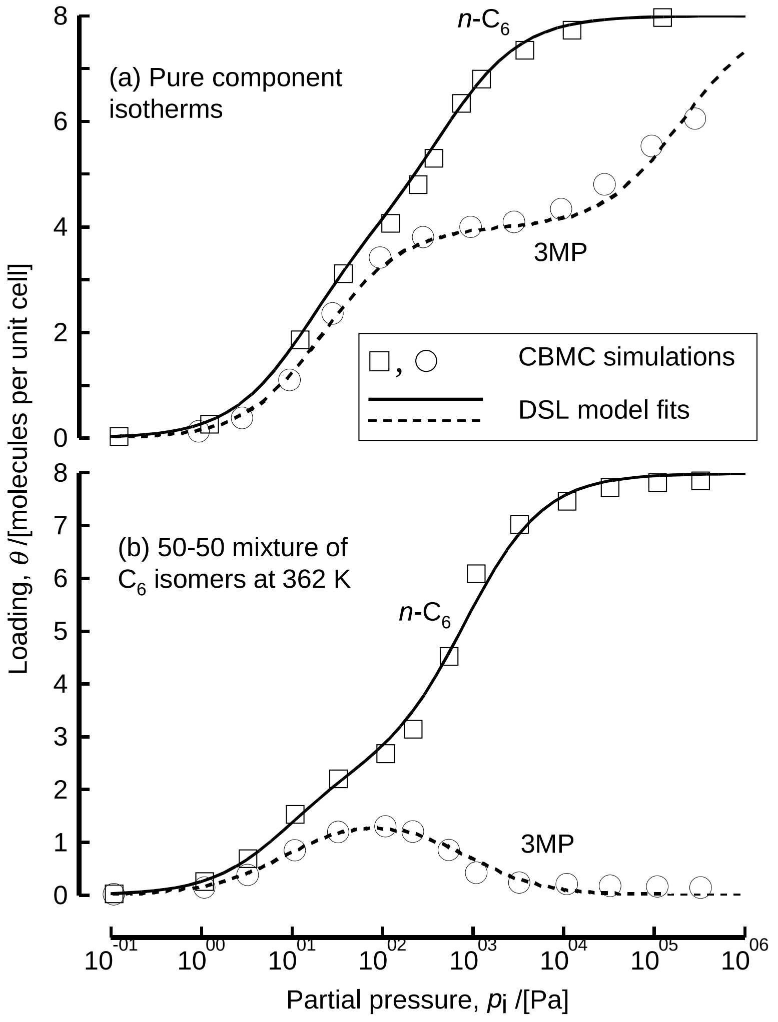

Figure 5.7: Pure component and 50%-50% mixture isotherms at 362K in Silicalite. The open square and circle symbols represent the CBMC simulations for (1) n-C_6 and (2) 3MP respectively. The continuous and dashed lines are the dual-site Langmuir (DSL) fits with the parameter values determined only from pure component CBMC simulation data. The dual-site Langmuir parameter values are for n-C_6 : $\theta_{1A} = 4$, $\theta_{1B} = 4$, $k_{1A} = 0.07\,\text{Pa}^{-1}$, $k_{1B} = 2 \times 10^{-3}\text{Pa}^{-1}$ and for 3MP: $\theta_{2A} = 4$, $\theta_{2B} = 4$, $k_{2A} = 0.045\,\text{Pa}^{-1}$, $k_{2B} = 5 \times 10^{-6}\,\text{Pa}^{-1}$.

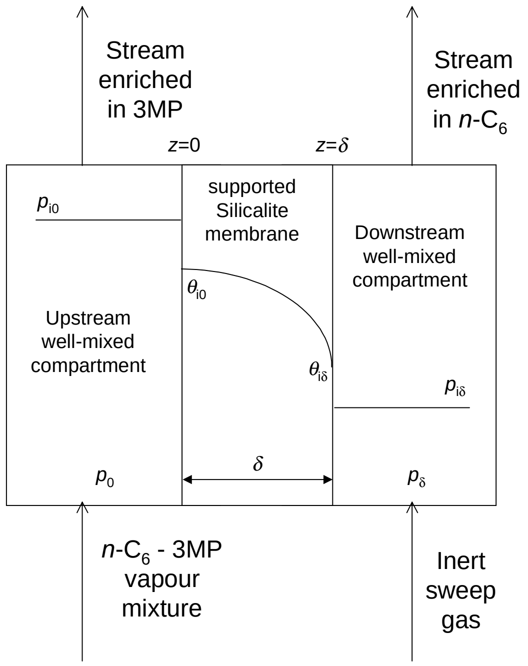

Figure 5.8: Schematic representation of a Silicalite membrane separation process for separation of C_6 isomers.

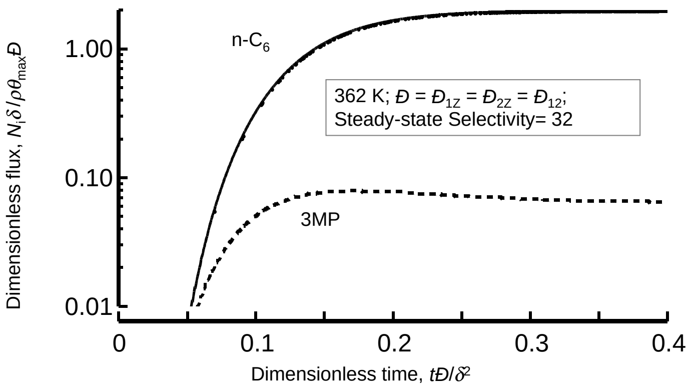

Figure 5.9: Transient diffusion fluxes for permeation of n-C_6 and 3MP across a Silicalite membrane. The conditions used in the simulations are identical to those used in the experiments of Funke *et al.* [216]. The upstream and downstream compartments are maintained at a total pressure of 84 kPa (atmospheric pressure at Boulder, Colorado, USA). In the upstream compartment the hydrocarbons account for 18 mole %, the remainder being inert gas helium. The partial pressures of n-C_6 and 3MP in the upstream compartment work out to 0.18×42 kPa for each isomer. An excess of sweep gas in the downstream compartment ensures that the partial pressures of the hydrocarbons are virtually zero.

5.4 Conclusions

- CBMC simulations of isotherms of 50%-50% binary mixtures of C_5, C_6 and C_7 hydrocarbon isomers showed some remarkable and hitherto unreported features. The loading of the branched isomer in all three binary mixture reaches a maximum when the total mixture loading corresponds to 4 molecules per unit cell. Higher loadings are obtained by "squeezing out" of the branched alkane from the Silicalite and replacing these with the linear alkane. This "squeezing out" effect is found to be entropic in nature; the linear alkanes have a higher packing efficiency and higher loadings are more easily achieved by replacing the branched alkanes with the linear alkanes.

- The mixture isotherms can be predicted quite accurately by applying the appropriate mixture rule to the dual-site Langmuir model. This model allows the mixture isotherm to be predicted purely on the basis of the parameters describing the isotherms of the pure components, linear and branched alkane.

- The sorption selectivity exhibited by Silicalite for the linear alkane in preference to the branched alkane in mixtures of C_5, C_6 and C_7 hydrocarbon isomers, provides a potential for the development of a novel separation technique based on entropy driven sorption selectivity [203].

Chapter 6

Diffusion of Isobutane in Silicalite studied by Transition Path Sampling*

6.1 Introduction

From both Monte Carlo (MC) simulations and experiments, it has been found that at low loading, branched alkanes are preferentially adsorbed at the intersections of Silicalite (see section 4.5); these intersections are located where a straight channel and a zigzag channel cross (see figure 4.1). Similar results have been obtained for benzene [92, 218, 219]. These bulky molecules diffuse via a hopping mechanism from one intersection to the next. This hopping, however, is a very infrequent event due to the large free energy barrier between two intersections [142]. Therefore, conventional Molecular Dynamics (MD) techniques cannot be used to study this process. A naive way of computing the hopping rate would be to perform MD simulations at higher temperatures, for which MD can be used efficiently [168]. By assuming that the temperature dependence of the diffusion coefficient is described by the Arrhenius equation one can extrapolate to a lower (desired) temperature. This method will not be able to produce accurate results when the extrapolation is performed over a large temperature range, not only because of extrapolation errors but also because the diffusion mechanism might be different at lower temperatures. For an extensive overview of diffusion in zeolites the reader is referred to the famous book of Kärger and Ruthven [220].

Recently, Smit *et al.* [142] have used transition state theory (TST) [30, 221] to calculate the hopping rate of branched alkanes in Silicalite; this technique has also been used by Brickmann and co-workers to study the diffusion of Xeon [222, 223] and aromatic molecules [224, 225] in the zeolite NaY; the activated diffusion of benzene in NaY has also been studied by Jousse and Auerbach using this technique [226]. Unfortunately, this method needs a priori information about the possible transition state. Although in principle the calculated hopping rate does not depend on the exact location of this transition state, the error bars of this calculated hopping rate do. Therefore, it might be advantageous to use a method in which this information is not required. This can be done with the transition path sampling method [227,228]. This method has been applied for the calculation of transition rates of ion pair dissociation in water [229], proton transfer in a protonated water trimer [230, 231], rearrangement of a Lennard-Jones cluster [232], isomerization of alanine dipeptide [233], and isomerization of a diatomic molecule in a Weeks-Andersen-Chandler (WCA) fluid [234].

In this chapter, we will use transition path sampling to study the hopping of the smallest branched alkane, isobutane, in the zeolite Silicalite. In section 6.2, we will briefly summarize

*This chapter is based on ref. [217].

this technique. In section 6.3, we will briefly focus on the simulation and model details and their implications, while in section 6.4 we will present our results and a comparison with experimental data. In appendix A, we will show how to calculate a free energy profile for a hydrocarbon in a zeolite with an arbitrary channel structure. This free energy profile is required to make an estimate of the diffusion coefficient using TST. It turns out that the Lennard-Jones size parameter describing the alkane-zeolite interactions has a large effect on this free energy barrier. In appendix B, we will briefly discuss the pseudo code of a bitwise time-reversible multiple timestep algorithm which is strictly speaking required in transition path ensemble simulations. In appendix C, we discuss how to apply parallel tempering for transition path ensemble simulations.

6.2 Transition Path Sampling

In this section, we will briefly summarize the transition path sampling method for deterministic paths which has been developed by David Chandler and co-workers based on earlier ideas of Pratt [235]. This method is not only able to calculate the hopping rate (and therefore also the diffusion coefficient) between two stable sites (here: the intersections of Silicalite). For a more complete discussion about this simulation technique, the reader is referred to refs. [227,232,234].

6.2.1 Introduction

Consider a dynamical system with two stable states, A and B, in which transitions from A to B are rare. This could be, for example, intersections of the zeolite Silicalite in which a branched alkane is preferentially adsorbed. The transition rate k from A to B can be calculated from the time derivative of an autocorrelation function $C(t)$,

$$\begin{aligned} k &= \frac{dC(t)}{dt} \qquad\qquad t_{mol} < t \ll t_{rxn} \\ C(t) &= \frac{\langle h_A(x_0)\, h_B(x_t)\rangle}{\langle h_A(x_0)\rangle}, \end{aligned} \tag{6.1}$$

provided that the relaxation time t_{rxn} of the system $[A, B]$ is much larger than the molecular relaxation time t_{mol} of the system in region A or B. As we will see in section 6.3, k is directly related to the diffusion coefficient. In equation 6.1, x_t represents the momenta $\mathbf{p}$ and positions $\mathbf{q}$ of the system at time t while x_0 represents the positions and momenta at time 0. We will consider only deterministic trajectories for which x_t is completely determined by the initial conditions x_0, *i.e.* $x_t = x_t(x_0)$. The functions h_A and h_B characterize the regions A and B, $h_{A,B}(x) = 1$ when $x \in A, B$, respectively, and $h_{A,B}(x) = 0$ otherwise. Note that A and B must be chosen in such a way that A and B do not overlap, *i.e.* $A \cap B = \varnothing$.

Since the function x_t is fully determined by the initial condition x_0, the ensemble averages in equation 6.1 can be written as an integration over the initial conditions weighted with the equilibrium distribution $\mathcal{N}(x_0)$

$$C(t) = \frac{\int dx_0 \mathcal{N}(x_0)\, h_A(x_0)\, h_B(x_t(x_0))}{\int dx_0 \mathcal{N}(x_0)\, h_A(x_0)} \tag{6.2}$$

We can also look at this equation as the ensemble average of $h_B(x_t)$ weighted with the equilibrium distribution $\mathcal{N}(x_0) \times h_A(x_0)$. In other words, $C(t)$ is the fraction of trajectories that start in A with distribution $\mathcal{N}(x_0)$ and reach B after time t. Since we are sampling over paths this ensemble is called the path ensemble. A procedure to sample this ensemble would be to

perform a molecular dynamics simulation to generate a new path of length t and subsequently use a Monte Carlo procedure to decide whether to accept or reject this new path. In this way, we generate an ensemble of paths which we can use to compute ensemble averages. In section 6.2.2 we will discuss the details on how to perform such a simulation.

In the remaining part of this chapter we will only consider a canonical ensemble of initial conditions x_0, *i.e.*

$$\mathcal{N}(x_0) = \exp[-\beta\mathcal{H}(x_0)] \tag{6.3}$$

Alternatively, one could use an ensemble in which the total energy, total momentum or total angular momentum of the system is conserved.

In principle, we could compute $C(t)$ from an "ordinary" path ensemble simulation. This would imply that we generate an ensemble of paths of length t that start at A and we would count all the paths that are at time t in B. However, since the transition from A to B is a rare event, the number of paths that end in B is so small that such an approach would require very long simulations. Therefore, we need to help the system explore the regions of interest. Suppose that region B can be defined by the value of an order parameter λ; $x_t \in B$ if $\lambda_{min} \leq \lambda(x_t) \leq \lambda_{max}$. In principle, one could use more order parameters to characterize region B. For equation 6.1, we can write

$$C(t) = \frac{\int dx_0 \exp[-\beta\mathcal{H}(x_0)]\, h_A(x_0)\, h_B(x_t(x_0))}{\int dx_0 \exp[-\beta\mathcal{H}(x_0)]\, h_A(x_0)} = \int_{\lambda_{min}}^{\lambda_{max}} d\lambda P(\lambda, t) \tag{6.4}$$

in which

$$P(\lambda, t) = \frac{\int dx_0 \exp[-\beta\mathcal{H}(x_0)]\, h_A(x_0)\, \delta[\lambda - \lambda(x_t(x_0))]}{\int dx_0 \exp[-\beta\mathcal{H}(x_0)]\, h_A(x_0)} \tag{6.5}$$

$P(\lambda, t)$ can be interpreted as the probability for the system to be in a state with a certain λ after time t given that the system is in A at time 0. Because $P(\lambda, t)$ is quite small in B (*i.e.* transitions from A to B are rare), it is advantageous to use umbrella sampling [29, 32] to compute $P(\lambda, t)$. By defining overlapping regions B_i by

$$x_t \in B_i \qquad \text{if} \qquad \lambda_{min}(i) \leq \lambda(x_t) \leq \lambda_{max}(i) \tag{6.6}$$

in such a way that $\cup B_i$ equals the whole phase space, one is able to calculate

$$\begin{aligned} P(\lambda, t, i) &= \frac{\int dx_0 \exp[-\beta\mathcal{H}(x_0)]\, h_A(x_0)\, h_{B_i}(x_t(x_0))\, \delta[\lambda - \lambda(x_t(x_0))]}{\int dx_0 \exp[-\beta\mathcal{H}(x_0)]\, h_A(x_0)\, h_{B_i}(x_t(x_0))} \\ &= \frac{\int dx_0 f(x_0, t, i)\, \delta[\lambda - \lambda(x_t(x_0))]}{\int dx_0 f(x_0, t, i)} \end{aligned} \tag{6.7}$$

in which

$$f(x_0, t, i) = \exp[-\beta\mathcal{H}(x_0)]\, h_A(x_0)\, h_{B_i}(x_t(x_0)) \tag{6.8}$$

$f(x_0, t, i)$ is the ensemble of all paths starting in A and ending in B_i at time t. In the next subsection, we will discuss how to sample from this distribution and similar distributions. Because

$$P(\lambda, t, i) \propto P(\lambda, t, j) \qquad i \neq j \tag{6.9}$$

one is able to calculate $C(t)$ by matching the distributions $P(\lambda, t, i)$ and integrate over region B. A disadvantage of this method is that the distributions $P(\lambda, t, i)$ can become quite steep,

especially when transitions from A to B are very rare. To sample more uniformly in window i, one can introduce a weight-function $W(\lambda(x_t), i)$ and sample from the distribution

$$\pi_i = f(x_0, t, i) \times \exp\left[W(\lambda(x_t), i)\right] \tag{6.10}$$

instead of from the distribution $f(x_0, t, i)$. The correct distribution is recovered using [29]

$$P(\lambda, t, i) = \frac{\langle \delta\left[\lambda - \lambda(x_t)\right] \exp\left[-W(\lambda(x_t))\right]\rangle_{\pi_i}}{\langle \exp\left[-W(\lambda(x_t))\right]\rangle_{\pi_i}} \tag{6.11}$$

As is shown in refs. [232, 234], it is advantageous to rewrite $C(t)$ as

$$\begin{aligned}
C(t) &= \frac{\langle h_A(x_0)\, h_B(x_t(x_0))\rangle}{\langle h_A(x_0)\rangle} \\
&= \frac{\langle h_A(x_0)\, h_B(x_t(x_0))\rangle}{\langle h_A(x_0)\, h_B(x_{t'}(x_0))\rangle} \times \frac{\langle h_A(x_0)\, h_B(x_{t'}(x_0))\rangle}{\langle h_A(x_0)\rangle} \\
&= C(t') \times \frac{\langle h_A(x_0)\, h_B(x_t(x_0))\, H_B(x_0, T)\rangle}{\langle h_A(x_0)\, h_B(x_{t'}(x_0))\, H_B(x_0, T)\rangle} \\
&= C(t') \times \frac{\int dx_0 \exp\left[-\beta\mathcal{H}(x_0)\right] h_A(x_0)\, H_B(x_0, T)\, h_B(x_t(x_0))}{\int dx_0 \exp\left[-\beta\mathcal{H}(x_0)\right] h_A(x_0)\, H_B(x_0, T)\, h_B(x_{t'}(x_0))} \\
&= C(t') \times \frac{\langle h_B(t)\rangle_{F(x_0,T)}}{\langle h_B(t')\rangle_{F(x_0,T)}}
\end{aligned} \tag{6.12}$$

in which $t, t' \in [0, T]$ and

$$H_B(x_0, T) = \max_{0 \leq t \leq T} h_B(x_t(x_0)) \tag{6.13}$$

The distribution

$$F(x_0, T) = \exp\left[-\beta\mathcal{H}(x_0)\right] h_A(x_0)\, H_B(x_0, T) \tag{6.14}$$

can be interpreted as the ensemble of trajectories starting in A and visiting B at least once in the time interval $[0, T]$. In this way, one has to perform only a single calculation of $C(t')$ when one would like to calculate the time derivative of $C(t)$

$$k = \frac{dC(t)}{dt} = \frac{C(t')}{\langle h_B(t')\rangle_{F(x_0,T)}} \times \frac{d\left[\langle h_B(t)\rangle_{F(x_0,T)}\right]}{dt} \tag{6.15}$$

while the functions $\langle h_B(t)\rangle_{F(x_0,T)}$ and $\langle h_B(t')\rangle_{F(x_0,T)}$ can be calculated from a (single) separate transition path sampling simulation.

6.2.2 Monte Carlo sampling from the distribution $F(x_0, T)$

In this section, we will present three types of Monte-Carlo trial moves to sample the distribution $F(x_0, T)$. Sampling of the distribution $f(x_0, t, i)$ is almost similar. We will use the symbols n and o for respectively the new and old configuration.

Shooting

In a shooting move, first one picks a time t' randomly from the interval $[0, T]$ and one adds a random displacement to the old positions ($\mathbf{q}_{t'}(o)$) and old momenta ($\mathbf{p}_{t'}(o)$):

$$\mathbf{p}_{t'}(n) = \mathbf{p}_{t'}(o) + \delta\mathbf{p}; \quad \mathbf{q}_{t'}(n) = \mathbf{q}_{t'}(o) + \delta\mathbf{q} \tag{6.16}$$

The components $\delta\mathbf{p}$ and $\delta\mathbf{q}$ are chosen at random from uniform distributions in the finite intervals $[-\Delta_{\mathbf{p}}, \Delta_{\mathbf{p}}]$ and $[-\Delta_{\mathbf{q}}, \Delta_{\mathbf{q}}]$, respectively. Note that in the original papers of Chandler and co-workers [232, 234] only changes in momentum were considered. However, for systems with large gradients in potential energies (for example a sorbate in a zeolite) one is able to sample the path ensemble much better when also position changes are applied. This is particularly important at low temperatures for which the contribution of the kinetic energy to the total energy is quite low.

Second, one has to construct a new path by integrating backward and forward to obtain $x_0(n)$ and $x_T(n)$, respectively. To obey detailed balance, the new path has to be accepted with a probability

$$\begin{aligned} \mathrm{acc}(o \to n) &= \min\left(1, \frac{F(x_0(n), T)\, P_g(n \to o)}{F(x_0(o), T)\, P_g(o \to n)}\right) \\ &= h_A(x_0(n))\, H_B(x_0(n), T) \times \\ &\quad \min\left(1, \frac{\exp[-\beta\mathcal{H}(x_0(n))]\, P_g(n \to o)}{\exp[-\beta\mathcal{H}(x_0(o))]\, P_g(o \to n)}\right) \end{aligned} \tag{6.17}$$

In this equation, $P_g(i \to j)$ is the probability to generate a trial move from state i to state j. When one assumes that the total energy along the transition path is conserved exactly, one is able to compute the second factor on the r.h.s. on the last line of equation 6.17 without having to integrate the equations of motion. This means that one can reject paths with an unfavorable energy immediately [236].

For symmetric generation probabilities like in equation 6.16 the factors $P_g(o \to n)$ and $P_g(n \to o)$ cancel. However, one can construct trial moves for which $P_g(o \to n) \neq P_g(n \to o)$. A well-known example of such a trial move is Configurational-Bias Monte Carlo (CBMC, see chapter 2). This can, for example, be used to change the orientation of the tail of a long branched molecule like 2-methylpentane, as such a reorientation will not be observed on the time-scales of MD in a narrow channel of a zeolite. It is important to note that one is able to construct many variations of the shooting trial move, for example, one can use rotation moves or choose the time t' with a bias. However, one has to ascertain that the new configuration at time t' does not differ too much from the old configuration at t' because otherwise the new path will not start in A or end in B.

Shifting

In a shifting move, one translates the initial conditions in time by an amount Δt:

$$x_0(n) = x_{\Delta t}(x_0(o)) \tag{6.18}$$

To have a symmetric generation of Δt, one has to choose

$$P_g(\Delta t) = P_g(-\Delta t) \tag{6.19}$$

Due to energy conservation along a trajectory, the acceptance/rejection rule for this trial move equals

$$\mathrm{acc}(o \to n) = h_A(x_0(n))\, H_B(x_0(n), T) \tag{6.20}$$

Although shifting trial moves do not sample the phase space ergodically because the energy of the path is not changed, they greatly improve statistics.

Parallel Tempering

Although in principle shooting and shifting moves sample the path ensemble ergodically, it can be difficult to sample different classes of pathways if they are not connected in path space. This can be solved by parallel tempering [237], which is discussed for transition path sampling in appendix C.

6.2.3 Transition State Ensemble

Traditionally, a transition state is defined as saddle points in the potential energy surface. In complex systems, however, saddle points are dense on the potential energy surface and enumeration of saddle points is neither possible nor can it provide insight into the transition mechanism. We therefore adopt a statistical notion of transition states which is identical to the procedure described in ref. [232] and define a configuration x to be a transition state if, for a given kinetic energy U_{kin}, the probability to reach A equals the probability to reach B after a time τ, which is in the order of t_{mol}. This collection of points $[x, U_{kin}]$ is called the transition state ensemble. In a transition path ensemble simulation, randomly selected points $[x, U_{kin}]$ of several transition paths are analyzed and investigated if they are a transition state. For such a configuration, a large number of MD trajectories with random initial momenta are computed. The fraction of trajectories that reach region A and B, respectively, is recorded. When these fractions are equal within certain error bars this configuration is labeled as a transition state. In detail, the following procedure is used:

1. Select a random point (here: isobutane molecule) of a transition path. For this point $[x, U_{kin}]$, we generate n_1 random momenta p from a Maxwell-Boltzmann distribution. These momenta are rescaled in such a way that the total initial kinetic energy of the system (U_{kin}) is a constant. The value of n_1 should be large enough to have some reasonable initial statistics on the probability of reaching regions A and B.

2. For each n_1 momenta, the equations of motion are integrated. If the system reaches A or B, or when the time of the integration exceeds τ, the integration is stopped.

3. From the n_1 integrations, we obtain estimates for p_A and p_B, which are respectively $\bar{p}_A$ and $\bar{p}_B$:

$$\bar{p}_A = \frac{n_A}{n_1}; \quad \bar{p}_B = \frac{n_B}{n_1} \tag{6.21}$$

in which n_A, n_B are the number of paths that reach A,B. The errors in these estimates are approximately

$$\sigma_A \approx \sqrt{\frac{\bar{p}_A (1 - \bar{p}_A)}{n_1}}; \quad \sigma_B \approx \sqrt{\frac{\bar{p}_B (1 - \bar{p}_B)}{n_1}} \tag{6.22}$$

When

$$|\bar{p}_A - \bar{p}_B| > \sigma_A + \sigma_B \tag{6.23}$$

the point $[x, U_{kin}]$ is rejected as a transition state. Otherwise, n_2 additional random momenta are generated and new values for $\bar{p}_A$, $\bar{p}_B$, σ_A and σ_B are computed. In case that after n_1+n_2 integrations, $|\bar{p}_A - \bar{p}_B| < \sigma_A+\sigma_B$, the point $[x, U_{kin}]$ is accepted as a transition state.

6.2.4 Integrating the equations of motion

When one would like to sample deterministic paths ($x_t = x_t(x_0)$), it is important that the equations of motion are integrated using a time-reversible integrator. Recently, Martyna, Tuckerman, and co-workers have shown how to systematically derive time reversible, area preserving MD algorithms from the Liouville formulation of classical mechanics [97,238]. A complication however is that using such integrators on a computer that uses (conventional) floating point precision arithmetics, the algorithm is not time-reversible anymore because of rounding errors of the computer.

In a conventional MD simulation it is generally accepted that not having bitwise time-reversibility is not a problem at all, but in a transition path ensemble simulation this means that a conventional floating point implementation of the shifting and shooting trial move will result in paths that are not deterministic (*i.e.* $x_t \neq x_t(x_0)$). To obey detailed balance in a Metropolis MC algorithm, the acceptance probability should approach 1 when the new trial configuration approaches the old configuration. When the paths are not integrated exactly time-reversible, a trial path that is generated by a shooting move might not start in region A or end in region B, even if the trial configuration of the selected point of the path is identical to the old configuration. Not obeying detailed balance in a MC simulation may lead to erroneous results [29,239].

A way to overcome this problem is the use of exact bitwise reversible integrators [240]. In our simulations, we have compared conventional time-reversible integrators with a bitwise (exact) time-reversible version of the multiple time-step algorithm of refs. [97,238] and we did not find any difference at all in the final results; see appendix B for a brief description of this algorithm. Therefore we conclude that although exact time-reversibility is strictly speaking required for transition path ensemble simulations, conventional time-reversible integrators seem to be suitable as well. However, strictly speaking one should test this carefully for all simulations. Note that if exact time-reversibility or accuracy in which the equations of motion are integrated have an effect on ensemble averages in the transition path ensemble, it would mean that transition path sampling simulations are completely useless.

6.3 Simulation and model details

We have used the model for alkane-zeolite and alkane-alkane interactions that has been described extensively in section 4.2. The following modifications of this model have been applied:

- Two bonded united atoms have a harmonic bond-stretching potential

$$u^{\text{stretch}}(l) = \frac{1}{2}k_l(l - l_0)^2 \tag{6.24}$$

  in which $l_0 = 1.54$Å and $k_l/k_B = 96500$ K Å^{-2} [57]. The reason for using this harmonic potential instead of fixed bond-lengths is that one is able to integrate the equations of motion time-reversible.

- We have added a dummy hydrogen atom to a CH group of isobutane to prevent a branched alkane from inverting itself; this dummy atom does not have any interaction with the zeolite. This unphysical inversion happens at high temperatures or on top of the barrier because the energy barrier for the inversion of a united-atom model of isobutane without dummy hydrogen atom is much lower than the energy barrier between two intersections. The dummy atom does not affect thermodynamic properties but it can lead to artificial dynamics.

Table 6.1: Hopping rates (events per second) and diffusion coefficients for diffusion in the straight (st) and zigzag (zz) channel as computed by transition state theory.

$\sigma/$ [Å]	$k_{st}/$ [s^{-1}]	$k_{zz}/$ [s^{-1}]	$D_{xx}/$ [m^2/s]	$D_{yy}/$ [m^2/s]	$D_{zz}/$ [m^2/s]	$D/$ [m^2/s]
3.364	5.1×10^8	1.4×10^8	1.4×10^{-10}	5.0×10^{-10}	2.0×10^{-10}	2.8×10^{-10}
3.60	1.7×10^7	6.4×10^6	6.4×10^{-12}	1.7×10^{-11}	8.3×10^{-12}	1.1×10^{-11}
3.64	5.0×10^6	1.8×10^6	1.8×10^{-12}	5.0×10^{-12}	2.3×10^{-12}	3.0×10^{-12}

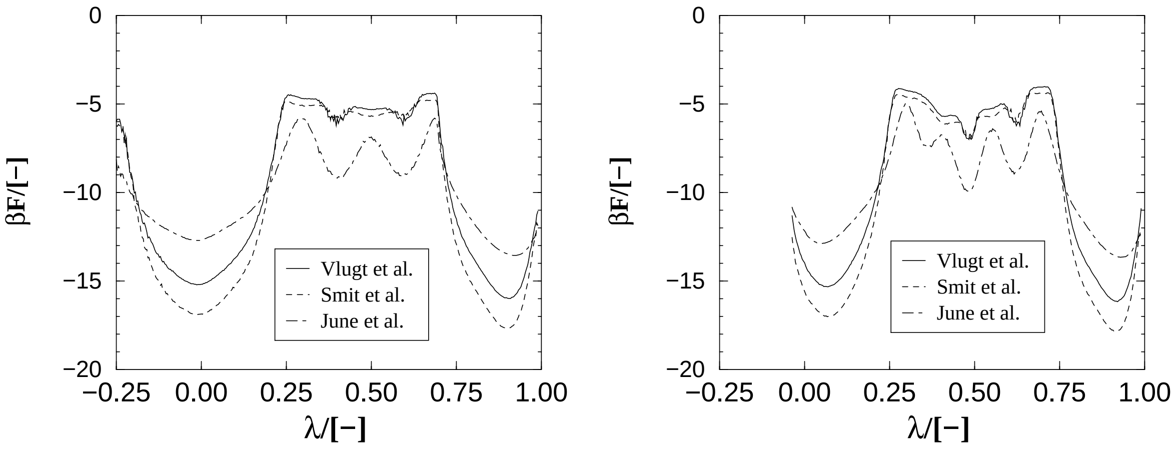

Figure 6.1: Free energy of a single isobutane molecule in the straight channel (left) or in the zigzag channel (right) of Silicalite as a function of the position in the straight channel for different force fields [36, 141, 142]. The two intersections are located at $\lambda = 0$ and $\lambda = 1$ (equation 6.25). See appendix A for details about these calculations.

- In our transition path ensemble simulations, we have used truncated and shifted Lennard-Jones interactions with $r_{cut} = 10$Å. Tail corrections have not been applied.

The use of a rigid zeolite is a quite crude assumption because it has been shown by many authors that the flexibility of the zeolite framework has a large effect on the diffusivity [170, 219, 241]. Furthermore, using a rigid zeolite also implies that sorbate molecules cannot exchange energy with the zeolite which means that the motion of a single sorbate molecule in a zeolite is ballistic. In a transition path ensemble simulation the hopping rate is calculated using a canonical ensemble of initial conditions; this implies that no energy with the zeolite is exchanged during the transition from A to B, but that energy can transfered when the molecules are in the stable states A or B. This corresponds to a conventional MD algorithm in which the initial conditions are generated from a Maxwell-Boltzmann distribution. The disadvantage of a flexible zeolite however is that those simulations take more than an order of magnitude more CPU time, which is the main reason why we have omitted this flexibility of the framework.

In section 4.5, we have showed that the Lennard-Jones size parameter σ for the alkane-zeolite interactions has a large effect on the adsorption isotherm. Here, we demonstrate that there is also a large effect on the free energy barrier between two intersections.

To demonstrate this effect, in figure 6.1 we have plotted the free energy profile of an isobutane molecule along a straight channel and a zigzag channel of Silicalite which has been calculated using the CBMC technique, see chapter 2. Details about this type of calculation can be found in ref. [142] and in appendix A. To map the coordinates of an isobutane molecule onto a single order parameter λ, we have defined λ in such a way that for a channel between intersec-

tions A and B, $\lambda_A = 0$ and $\lambda_B = 1$:

$$\lambda(\mathbf{x}) = 1 - \frac{|\mathbf{x} - \mathbf{x}_B|}{|\mathbf{x}_A - \mathbf{x}_B|}, \tag{6.25}$$

in which $\mathbf{x}_A$ and $\mathbf{x}_B$ are the centers of the stable regions A and B and $\mathbf{x}$ is the position of the CH group of isobutane. Indeed, the precise value of σ_{CH_i-O} has a large effect on the height of the barrier. In the model of June *et al.* the height of the barrier is reduced by almost 50% compared to the model of ref. [36]. Another important feature is that this free energy profile shows several local minima and maxima in which isobutane can be stuck when TST with dynamical corrections is used. To compute the hopping rate using TST, we have used the same procedure as in ref. [142]. We have also assumed that the hopping rate is completely determined by the largest free energy barrier. As can be seen in table 6.1, the hopping rates of the different force fields differ by two orders of magnitude.

In our transition path ensemble simulations, we have used at least 10^6 cycles in every simulation. In every cycle, it is decided at random do to a shooting move in which the momenta are changed (10%), a shooting move in which isobutane is displaced (10%), or a shifting move (80%). All maximum displacements were chosen in such a way that 33% of all trial moves are accepted. The equations of motion were integrated using a multiple time-step algorithm [97,238] in which the largest time-step was 10^{-3} ps, which results in an average relative deviation of the total energy of around 10^{-5} (see the definition in ref. [97]). The stable regions A and B were defined as all positions within a distance of 2.5Å of the center of an intersection of Silicalite. A typical simulation takes 2 weeks (!) on a Linux PC equipped with an AMD K7 (Athlon) 500 MHz processor.

From the hopping rates for the zigzag channel (k_{zz}) and straight channel (k_{st}) one is able to compute the diffusion tensor at zero loading [142,242,243]:

$$D_{xx} = \frac{1}{4} k_{zz} a^2; \quad D_{yy} = \frac{1}{4} k_{st} b^2; \quad D_{zz} = \frac{1}{4} \frac{k_{zz} k_{st}}{k_{zz} + k_{st}} c^2 \tag{6.26}$$

in which a, b and c are the unit vectors in the diffusion lattice of Silicalite ($a = 20.1$Å, $b = 19.9$Å and $c = 26.8$Å. In the z-direction, the diffusion length is two times the length of the unit cell of Silicalite.). As the total diffusivity D is proportional to the total mean square displacement per unit of time, *i.e.*

$$D = \frac{1}{6} \lim_{t \to \infty} \frac{\langle \mathbf{r}(t) \rangle}{t} \tag{6.27}$$

we can write

$$D = \frac{D_{xx} + D_{yy} + D_{zz}}{3} \tag{6.28}$$

In equation 6.26, we have assumed that two successive crossings are uncorrelated, which is a reasonable assumption for isobutane but maybe invalid for longer 2-methylalkanes because of the orientation of the tail of the molecule. To study the concentration dependence of the diffusion tensor, it would be interesting to use these microscopic hopping rates in a kinetic Monte Carlo scheme [244,245].

6.4 Results

6.4.1 Calculating the hopping rate

In figure 6.2, we have plotted the function $\langle h_B(t) \rangle_{F(x_0,T)}$ both for the straight and zigzag channel for $T = 15$ ps. For long times, as expected, this function approaches a straight line. In figure 6.3,

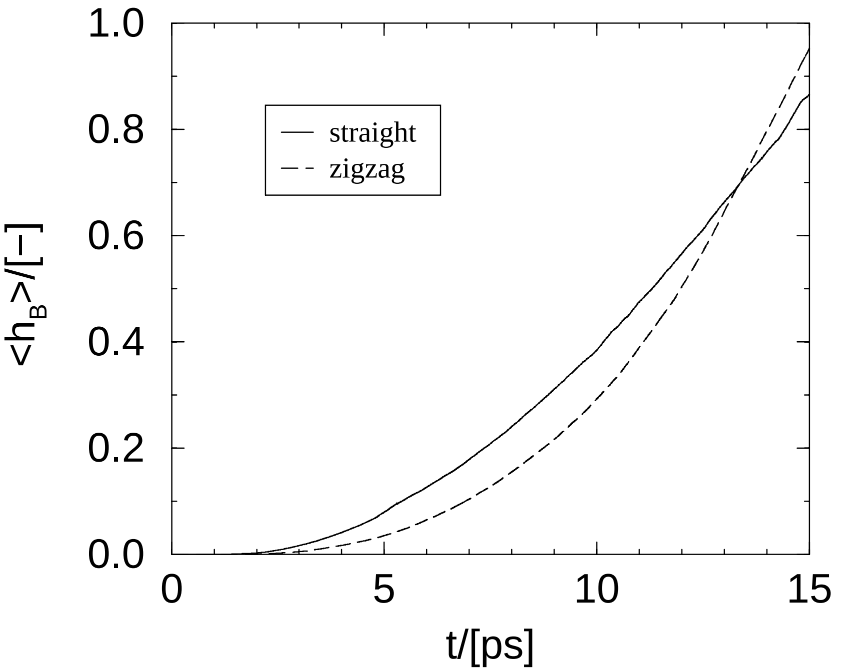

Figure 6.2: The function $\langle h_B(t) \rangle_{F(x_0,T)}$ both for diffusion in the straight and zigzag channel. $T = 15$ps.

we have plotted the function $P(\lambda, t)$ for $t = 6.0$ ps which has been computed by using umbrella sampling. Clearly, this function has several local minima and maxima that are also present in the free energy profiles (see figure 6.1). By integrating over region B we obtain $p_{st} = 6 \times 10^{-10}$ and $p_{zz} = 8 \times 10^{-10}$.

By combining all results we obtain $k_{st} = 0.4 \times 10^3 s^{-1}$ and $k_{zz} = 0.16 \times 10^3 s^{-1}$. Using equations (6.26) and (6.28) we obtain $D_{xx} = 2 \times 10^{-16} m^2/s$, $D_{yy} = 4 \times 10^{-16} m^2/s$, $D_{zz} = 6 \times 10^{-16} m^2/s$ and $D = 4 \times 10^{-16} m^2/s$. Due to the large error-bars introduced by matching the histograms in the free energy calculations we can only say that the computed diffusivity is in the order of $10^{-15} - 10^{-16}$ m^2/s. When we compare this diffusivity with the diffusivity obtained by TST (see table 6.1) we obtain a transmission coefficient of around 10^{-4}. The diffusion coefficients are almost equal for the straight and zigzag channel, which can be explained by an almost equal channel diameter of the straight and zigzag channel.

The diffusivity of isobutane in Silicalite at 300 K has been measured by several groups using different experimental techniques; Hufton and Danner (chromatographic) [246] $2 \times 10^{-12} m^2/s$ at 297 K, Shah *et al.* (membrane permeation) [247] $1 \times 10^{-12} m^2/s$ at 298 K, Nijhuis *et al.* (multitrack) [248] $6 \times 10^{-13} m^2/s$, Bakker *et al.* (membrane permeation) [249] $4 \times 10^{-12} m^2/s$, Chiang *et al.* (chromatographic, extrapolated to 300 K by using Arrhenius law) [188] $5 \times 10^{-17} m^2/s$, Millot *et al.* (QENS, extrapolated to 300 K by using Arrhenius law) [250] $2 \times 10^{-13} m^2/s$, and Millot *et al.* (membrane permeation, extrapolated to 300 K by using Arrhenius law) [250] $5 \times 10^{-13} m^2/s$. Comparing the experimental results shows that the diffusion coefficients differ by one order of magnitude; the data of Chiang *et al.* is significantly lower. It is well established in literature that microscopic and macroscopic diffusivities can differ several orders of magnitude [220]. Most experimental diffusivities are several orders of magnitude higher than our simulation result.

An explanation for this is that the σ value of 3.6Å we have used is somewhat too high; the simulations of Bouyermaouen and Bellemans [170] report a diffusivity of $3 \times 10^{-11} m^2/s$ for MD simulations using $\sigma = 3.364$Å, which is an order of magnitude larger than most experimental

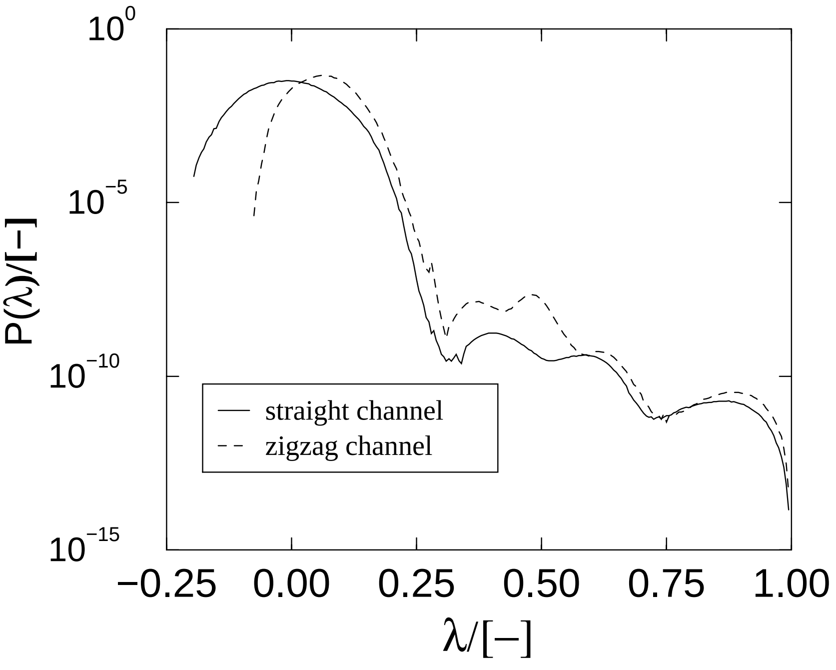

Figure 6.3: Probability $P(\lambda)$ to find a particle at position λ for $t = 6.0$ ps for both the straight and zigzag channel. This function has been constructed by matching 10 overlapping windows. The two intersections are located at $\lambda = 0$ and $\lambda = 1$ (equation 6.25).

results. For the same system but with a flexible zeolite they found $2 \times 10^{-10} m^2/s$. When we insert our TST results for $\sigma = 3.364$Å we obtain $2.8 \times 10^{-10} m^2/s$, which is an order of magnitude larger that the MD result. As the free energy barrier is largely reduced by using this low value of σ we do not expect that their simulations are effected by the inversion of isobutane.

Apparently, the optimal σ should be somewhere between 3.35Å and 3.60Å. Also, in our model we have assumed a rigid zeolite lattice to save CPU time, which may result in a diffusivity that is one order of magnitude too low [170, 219]. This suggest that one should carefully choose the model system.

6.4.2 Transition state ensemble

To locate possible transition states, we have used the procedure described in section 6.2.3 using $n_1 = 50$ and $n_2 = 150$. Every 10,000 MC steps in a simulation of $F(x_0, T)$, 200 randomly selected points of the current path were analyzed by assigning random momenta and integrating the equations of motion for at most 15,000 time-steps. This procedure was continued until 300 transition states have been identified. In figure 6.4, we have plotted the position of the branch for all transition states both for diffusion in the straight channel and in the zigzag channel. Clearly, the transition states are somewhat between the stable regions A and B (which is not very surprising of course).

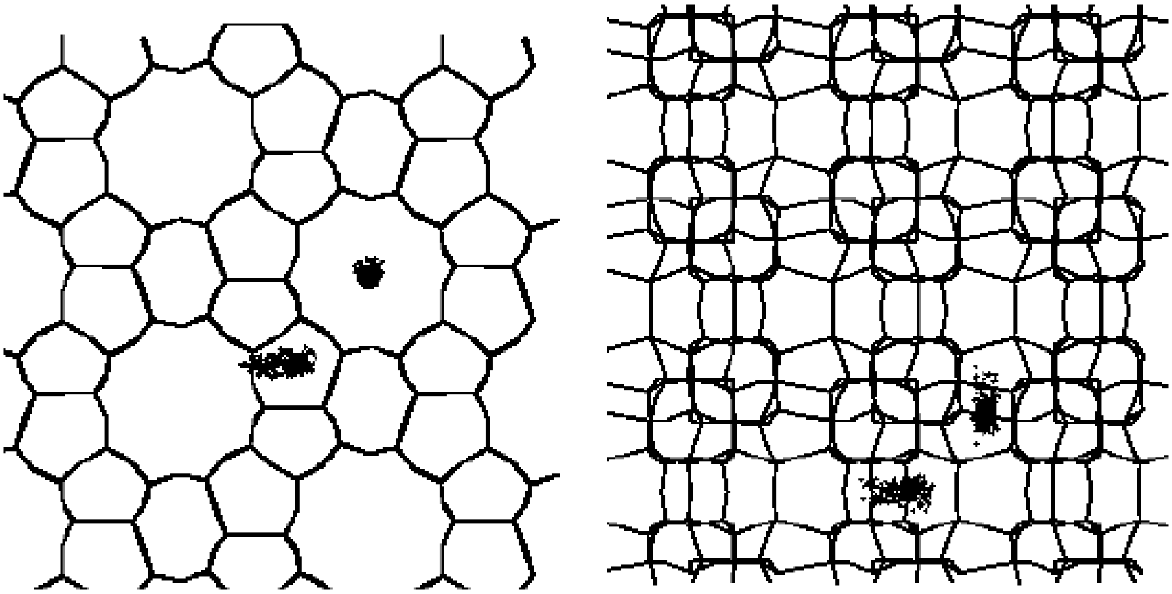

Figure 6.4: Schematic representation of all transition states (dots) both for diffusion in the straight channels and in the zigzag channels. Left: Top view, the straight channels are perpendicular to the plane. Right: Side view, the straight channels are from top to bottom while the zigzag channels are from left to right (but not in the plane).

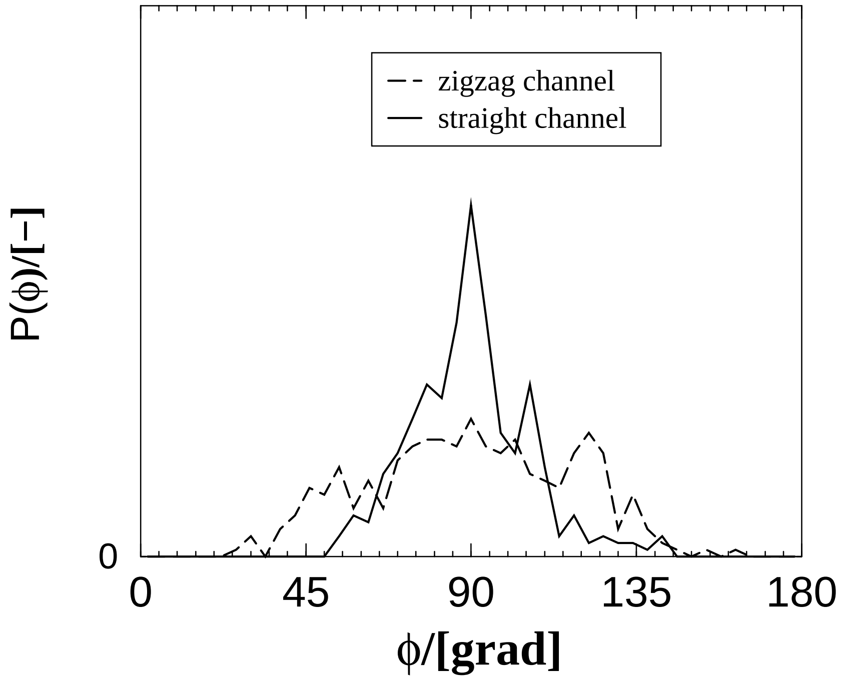

Figure 6.5: Probability distribution of the orientational order parameter ϕ of all generated transition states for both the straight and zigzag channel.

A more interesting property is the orientation of the molecules in the transition state. We have defined the orientational order parameter ϕ as the angle between a straight line connecting the centers of the stable regions A and B and the bond-vector $C_{\text{branch}} - H$ in which H is a dummy atom that prevents isobutane from inverting itself (see section 6.3). In figure 6.5, we have plotted the probability distribution of ϕ. It turns out that the distribution of ϕ has a maximum for approximately 90°, which is more pronounced for the straight channel than for the zigzag channel (which is quite obvious because the zigzag channel is not straight). This means that orientations in which all three methyl-groups all point either to region A or B are no transition states, which also suggests that for longer branched alkanes the orientation of the tail will decide to which stable state the molecule will move. This is in agreement with the transition state simulations of Smit *et al.* [142] who found that the transmission coefficient of 2-methylhexane in Silicalite is extremely low.

6.5 Conclusions

In summary, we have used transition path sampling to study the diffusion of isobutane in Silicalite. Our computed diffusion coefficient is significantly lower than the diffusion coefficient obtained by experiments or by the use of transition state theory. The difference with the experimental result might be due to either the use of a rigid zeolite or a Lennard-Jones size parameter describing the alkane-zeolite interactions that is too high. We found that not only the position of the center of mass but also the orientation of an isobutane molecule is important in the identification of transition states. It would be very interesting to compare transition path sampling with the scheme of Ruiz-Montero *et al.* [251]. This scheme is a modification of transition state theory with dynamical corrections which is suited to study systems with a low transmission coefficient efficiently.

6.6 Appendix A: Calculation of a free energy profile

To compute the hopping rate using TST, one has to know the free energy (F) as a function of the reaction coordinate (λ). For a branched alkane, it is conventional to use the position of the CH group for this. To compute the free energy for a given reaction coordinate, we can use CBMC to grow a chain molecule. In ref. [29] it is shown that the free energy $F(\lambda)$ at position λ is related to the average Rosenbluth factor $W(\lambda)$ (see equation 2.9);

$$\exp\left[-\beta F(\lambda)\right] = C \times \langle W(\lambda) \rangle \tag{6.29}$$

in which C is a constant which is determined by the reference frame of the free energy.

To compute the free energy as a function of the position in the channel of a zeolite, one should be able to map the reaction coordinate λ onto the position in the channel. For the straight channel in Silicalite this mapping is quite trivial, *i.e.* the reaction coordinate is the projection on a straight line from one intersection to another. However, if one would use the same method for the zigzag channel one would obtain a rather unphysical reaction coordinate because this zigzag channel is not straight, so the free energy as a function of the reaction coordinate λ will not be very meaningful.

To compute a more realistic realistic reaction coordinate, we will use a cord of N segments that connects the middles of two intersections; the endpoints $\mathbf{r}_1$ and $\mathbf{r}_N$ of this cord remain fixed.

The total energy U of this cord equals:

$$U = \sum_{i=1}^{i=N} u_i(\mathbf{r}_i) + k_{cord}[N-1] \times \sum_{i=1}^{i=N-1} |\mathbf{r}_{i+1} - \mathbf{r}_i|^2 \tag{6.30}$$

in which $u_i(\mathbf{r}_i)$ is the energy of a CH group at position $\mathbf{r}_i$. For sufficient large k_{cord} one can produce a cord of $N-1$ segments of equal length by minimizing the total energy of the cord (U). We have chosen k_{cord} is such a way that the differences in length of the segments ($\mathbf{r}_{i+1} - \mathbf{r}_i$) are less than 1%. The reason for the factor $N-1$ is to make sure the total energy of the spring part of U is independent of N. To see this, consider a cord of (constant) length l which is divided into $N-1$ segments. The energy of the spring part of this cord equals:

$$U = k_{cord}[N-1] \times \sum_{i=1}^{i=N-1} \left(\frac{l}{N-1}\right)^2 = k_{cord} l^2 \tag{6.31}$$

which is independent of N when the length of the cord l is approximately constant:

$$l \approx \sum_{i=1}^{i=N-1} |\mathbf{r}_{i+1} - \mathbf{r}_i|^2 \tag{6.32}$$

To be able to compare the free energy profile with the distribution $P(\lambda, t)$, we have plotted the free energy as a function of λ, which is defined in equation 6.25.

6.7 Appendix B: Bitwise time-reversible multiple time-step algorithm

To construct bitwise time-reversible trajectories, we have modified the original RESPA integrator from refs. [97, 238]; see table 6.2. In algorithm, the positions `Rx,Ry,Rz` and velocities `Vx,Vy,Vz` are integer multiplications of 2^{-i} (here: $i = 30$), although they are stored as floats. The forces `Fx,Fy,Fz` however are computed in floating point precision, which means that the calculation of the force does not have to be changed.

Table 6.2: FORTRAN77 pseudo code of a bitwise time-reversible multiple time-step integrator using `Nrespa` short (`S`) time-steps for every long (`L`) time-step of length `Tst`. The function `Bnt` rounds a float to the nearest integer with a precision of 2^{-30}; the FORTRAN77 function `nint` rounds off to the nearest integer. The mass of the particles equals `1/Rm`.

```
Function Bnt(X)
Double Precision Bnt,X
Integer*8 I

I   = Nint(X*Dble(2**30)
Bnt = (2.0d0**-30)*Dble(I)
```

```
Subroutine Integrate

Do Ires=1,Nrespa
  If(Ires.Eq.1) Then
    Do I=1,Natom
      Vx(I) = Bnt(Vx(I) + Bnt(0.5*Tst*Rm*Fx_L(I)))
      Vy(I) = Bnt(Vy(I) + Bnt(0.5*Tst*Rm*Fy_L(I)))
      Vz(I) = Bnt(Vz(I) + Bnt(0.5*Tst*Rm*Fz_L(I)))
    Enddo
  Endif
  Do I=1,Natom
    Vx(I) = Bnt(Vx(I) + Bnt(0.5*Tst*Rm*Fx_S(I)/Nrespa))
    Vy(I) = Bnt(Vy(I) + Bnt(0.5*Tst*Rm*Fy_S(I)/Nrespa))
    Vz(I) = Bnt(Vz(I) + Bnt(0.5*Tst*Rm*Fz_S(I)/Nrespa))
    Rx(I) = Bnt(Rx(I) + Bnt(Tst*Vx(I)/Nrespa))
    Ry(I) = Bnt(Ry(I) + Bnt(Tst*Vy(I)/Nrespa))
    Rz(I) = Bnt(Rz(I) + Bnt(Tst*Vz(I)/Nrespa))
  Enddo
  If(Ires.Eq.Nrespa) Then
    Call Force_S_L(Fx_S,Fy_S,Fz_S,Fx_L,Fy_L,Fz_L)
  Else
    Call Force_S(Fx_S,Fy_S,Fz_S)
  Endif
  Do I=1,Natom
    Vx(I) = Bnt(Vx(I) + Bnt(0.5*Tst*Rm*Fx_S(I)/Nrespa))
    Vy(I) = Bnt(Vy(I) + Bnt(0.5*Tst*Rm*Fy_S(I)/Nrespa))
    Vz(I) = Bnt(Vz(I) + Bnt(0.5*Tst*Rm*Fz_S(I)/Nrespa))
  Enddo
  If(Ires.Eq.Nrespa) Then
    Do I=1,Natom
      Vx(I) = Bnt(Vx(I) + Bnt(0.5*Tst*Rm*Fx_L(I)))
      Vy(I) = Bnt(Vy(I) + Bnt(0.5*Tst*Rm*Fy_L(I)))
      Vz(I) = Bnt(Vz(I) + Bnt(0.5*Tst*Rm*Fz_L(I)))
    Enddo
  Endif
Enddo
```

6.8 Appendix C: Parallel tempering

6.8.1 Introduction

Parallel tempering [18,86,237,252] is a very useful Monte Carlo technique for systems that suffer from ergodicity problems. For example, in transition path sampling there might be two different paths (C and D) that are separated by a high energy barrier in such a way that transitions between these paths occur very rarely when only shifting and shooting trial moves are used. For such a system, one would need a very long simulation to sample all possible paths.

In parallel tempering, N independent systems are simulated simultaneously. The total partition function of this system (Q) equals

$$Q = \prod_{i=1}^{i=N} Q_i \tag{6.33}$$

in which Q_i equals

$$Q_i = \sum_{x_i} f(x_i, \beta_i) \tag{6.34}$$

For example, for the canonical ensemble, the function $f(x_i, \beta_i)$ equals

$$f(x_i, \beta_i) = \exp\left[-\beta_i \mathcal{H}(x_i)\right] \tag{6.35}$$

in which $\beta_i = 1/(k_B T_i)$. Let us consider two different trial moves:

1. Displacement. A system i is selected with a fixed probability p_i. For this system, a new point in phase-space ($x_i(n)$) is generated from $x_i(o)$, we assume here that this generation is symmetric and that the other systems j are not affected ($x_j(n) = x_j(o)$, $j \neq i$). The ratio of acceptance probabilities equals

$$\frac{\mathrm{acc}(o \to n)}{\mathrm{acc}(n \to o)} = \frac{\prod_{k=1}^{k=N} f(x_k(n), \beta_k)}{\prod_{k=1}^{k=N} f(x_k(o), \beta_k)} = \frac{f(x_i(n), \beta_i)}{f(x_i(o), \beta_i)} \tag{6.36}$$

   Note that this expression does not depend on $f(x_j, \beta_j)$. For the canonical ensemble, this equation reduces to

$$\frac{\mathrm{acc}(o \to n)}{\mathrm{acc}(n \to o)} = \exp\left[-\beta_i\left(\mathcal{H}(x_i(n)) - \mathcal{H}(x_i(o))\right)\right] \tag{6.37}$$

   To sample all N systems equally well, p_i should be proportional to the time constant of a characteristic autocorrelation function.

2. Swapping. Two systems (i and j, $i \neq j$) are selected at random, the systems are swapped by choosing $x_i(n) = x_j(o)$ and $x_j(n) = x_i(o)$. The ratio of acceptance probabilities equals

$$\frac{\mathrm{acc}(o \to n)}{\mathrm{acc}(n \to o)} = \frac{\prod_{k=1}^{k=N} f(x_k(n), \beta_k)}{\prod_{k=1}^{k=N} f(x_k(o), \beta_k)} = \frac{f(x_j(o), \beta_i) f(x_i(o), \beta_j)}{f(x_i(o), \beta_i) f(x_j(o), \beta_j)} \tag{6.38}$$

   For the canonical ensemble, this equation reduces to

$$\frac{\mathrm{acc}(o \to n)}{\mathrm{acc}(n \to o)} = \exp\left[(\beta_i - \beta_j) \times \left(\mathcal{H}(x_i(o)) - \mathcal{H}(x_j(o))\right)\right] \tag{6.39}$$

   Such trial moves will be accepted when there is enough overlap between $f(x_i, \beta_i)$ and $f(x_j, \beta_j)$.

In practice, this means that a transition from path C to path D that, without swapping trial moves, rarely occurs in system i but quite frequently in system j ($j \neq i$, for example, because $\beta_j \ll \beta_i$), can also occur in system i. Additionally, due to accepted swapping trial moves the correlation time of subsequent elements of the Markov chain is largely reduced. When $f(x_i, \beta_i)$ and $f(x_j, \beta_j)$ are stored during the simulation, the computational cost in this trial move is negligible.

6.8.2 Application to transition path sampling

In this section, we will discuss two applications of parallel tempering in path ensemble simulations:

1. Simulation at different temperatures. When paths are sampled in the canonical ensemble, *i.e.*

$$F(x_0, T) = \exp\left[-\beta\mathcal{H}(x_0)\right] h_A(x_0) H_B(x_0, T) \tag{6.40}$$

one can simulate different systems with different β and apply swapping trial moves between different systems. However, when paths are sampled in the micro-canonical ensemble, *i.e.*

$$F(x_0, T) = \delta\left(\mathcal{H}(x_0) - \mathcal{H}_0\right) h_A(x_0) H_B(x_0, T) \tag{6.41}$$

the acceptance probability for swapping trial moves between systems with a different $\mathcal{H}_0$ is zero.

2. Umbrella sampling. To compute $P(\lambda, t)$, it is sometimes advantageous to define overlapping regions B_i by

$$x \in B_i \qquad \text{if} \qquad \lambda_{\min}(i) \leq \lambda(x_t) \leq \lambda_{\max}(i) \tag{6.42}$$

in such a way that $\cup B_i$ equals the whole phase space. When all regions are simulated simultaneously, one is able to perform trial moves that swap paths between two overlapping regions B_i and B_j ($i \neq j$). When no additional window potential $W(\lambda(x_t))$ is defined, such a trial move is accepted when both paths are in the overlapping region of B_i and B_j (*i.e.* $h_{B_i} = h_{B_j} = 1$). Note this holds both for simulations in the canonical as well as in the micro-canonical ensemble.

Of course, both techniques can also be combined to sample $P(\lambda, t, \beta)$ for different overlapping regional B_i and different temperatures β_i in a single simulation.

6.8.3 Model system

To illustrate this method, we have used a two-dimensional system consisting of 9 WCA particles:

$$u_{\mathrm{WCA}}(r) = \begin{cases} 1 + 4\left[\left(\frac{1}{r^{12}}\right) - \left(\frac{1}{r^{6}}\right)\right] & r \leq r_{\mathrm{WCA}} \\ 0 & r > r_{\mathrm{WCA}} \end{cases} \tag{6.43}$$

in which $r_{\mathrm{WCA}} = 2^{1/6}$. However, two particles (1 and 2) interact via a double well potential:

$$u_{\mathrm{dw}}(\lambda) = h\left[1 - \frac{(\lambda - w - r_{\mathrm{WCA}})^2}{w^2}\right]^2 \tag{6.44}$$

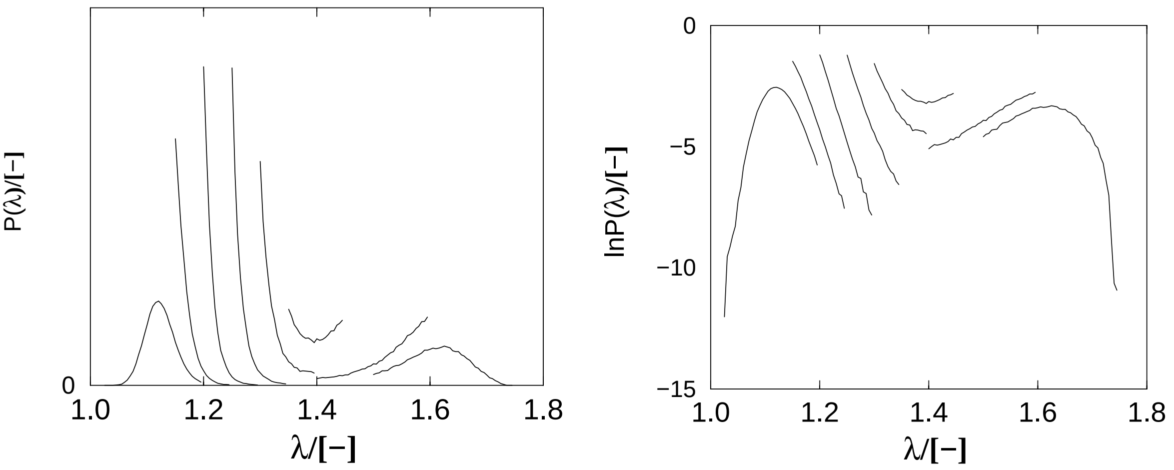

Figure 6.6: Probability distribution $P(\lambda, i)$ for all slices. $P(\lambda, i) \propto P(\lambda, j)$ for $i \neq j$.

in which λ is the distance between the particles. This system is described in detail in ref. [234]. We have used $w = 0.25$, $h = 6$, $\Delta t = 0.001$ and a box-size of 4 in both directions. We have chosen the regions A and B such that $x \in A$ when $\lambda < 1.3$ and $x \in B$ when $\lambda > 1.45$. All transition path ensemble simulations have been performed in the canonical ensemble using $\beta = 2$; the total impulse of the system is constrained to 0 in all dimensions. The total length of the paths was 5.0. We have defined 8 overlapping regions:

1. $0.00 < \lambda_1 < 1.20$
2. $1.15 < \lambda_2 < 1.25$
3. $1.20 < \lambda_3 < 1.30$
4. $1.25 < \lambda_4 < 1.35$
5. $1.30 < \lambda_5 < 1.40$
6. $1.35 < \lambda_6 < 1.45$
7. $1.40 < \lambda_7 < 1.60$
8. $1.50 < \lambda_8 < \infty$

In our simulations, there are three types of (randomly selected) trial moves:

1. Shifting ($(70 - x)$ %).
2. Shooting (30%). A randomly selected particle of a randomly selected slice of a randomly selected system is given a random displacement; the maximum displacement is adjusted such that 33% of the trial moves are accepted.
3. Swapping (x%). Two overlapping regions are selected at random. An attempt is made to swap the systems in these regions.

The total simulation consisted of 2×10^6 cycles; in every cycle the number of trial moves equals the number of slices (here: 8).

In figure 6.6, we have plotted the distributions $P(\lambda, i)$ for the various slices i. As there is considerable overlap between the slices, one is able to construct the function $P(\lambda)$ accurately.

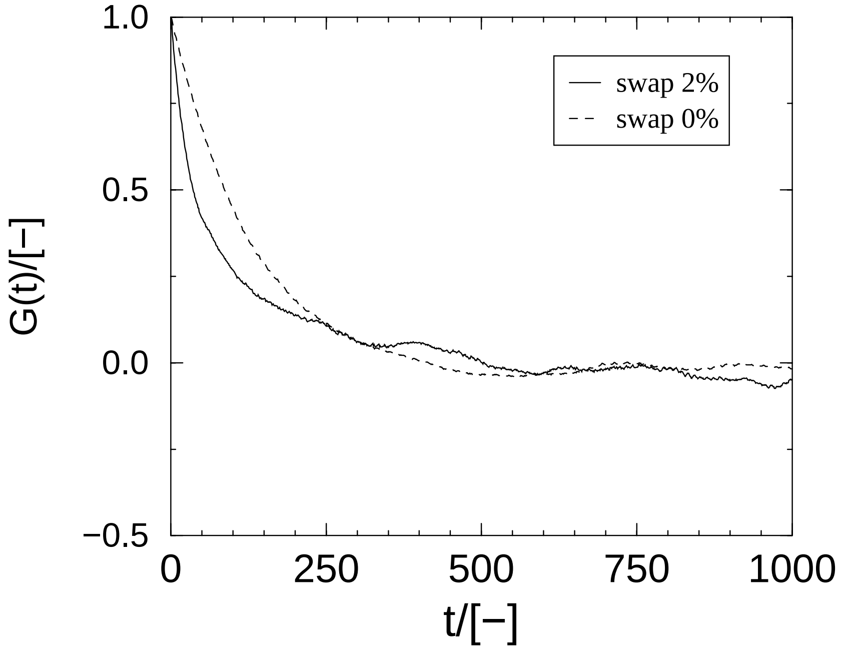

Figure 6.7: Energy autocorrelation function for $i = 1$.

To define the efficiency of these simulations, we have calculated the energy autocorrelation:

$$G(t) = \frac{\langle \delta E(t)\, \delta E(0) \rangle}{\langle \delta E^2 \rangle} \tag{6.45}$$

in which t is the number of Monte Carlo cycles and $\delta E = E - \langle E \rangle$. In figures 6.7, 6.8 and 6.9 we have plotted the function $G(t)$ with and without swapping trial moves for slices $i = 1$, $i = 5$ and $i = 8$. For $i = 1$ and $i = 8$, there is not much difference in efficiency, although the correlation time is larger when no swapping occur. The reason for this is that slice 7 and 8 have quite a large overlap and therefore a too large acceptance probability for swapping moves (32%). For $i = 5$ (and also for $i = 6$ and $i = 4$, not shown here) however, the difference is huge. Without swapping trial moves, the amount of trial moves to obtain a configuration with an independent energy is increased by a factor 3. The reason for this is that slice $i = 5$ is located at the maximum of the double well potential; when a path ends before the barrier the energy is much lower then when a path is just able to cross the barrier.

In summary, we have demonstrated the use of parallel tempering in transition path ensemble simulations. The use of parallel tempering has the potential to make these simulations more efficient.

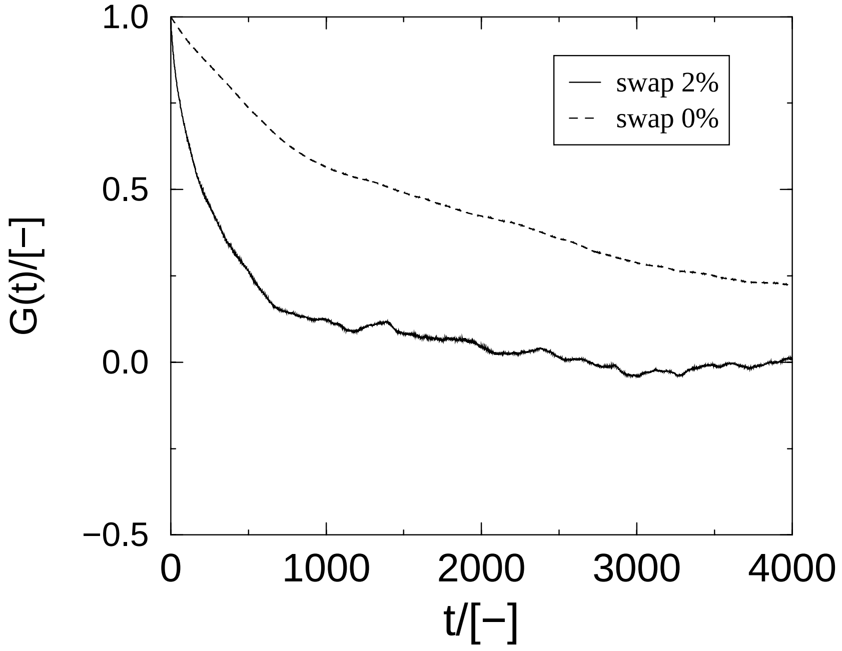

Figure 6.8: Energy autocorrelation function for $i = 5$.

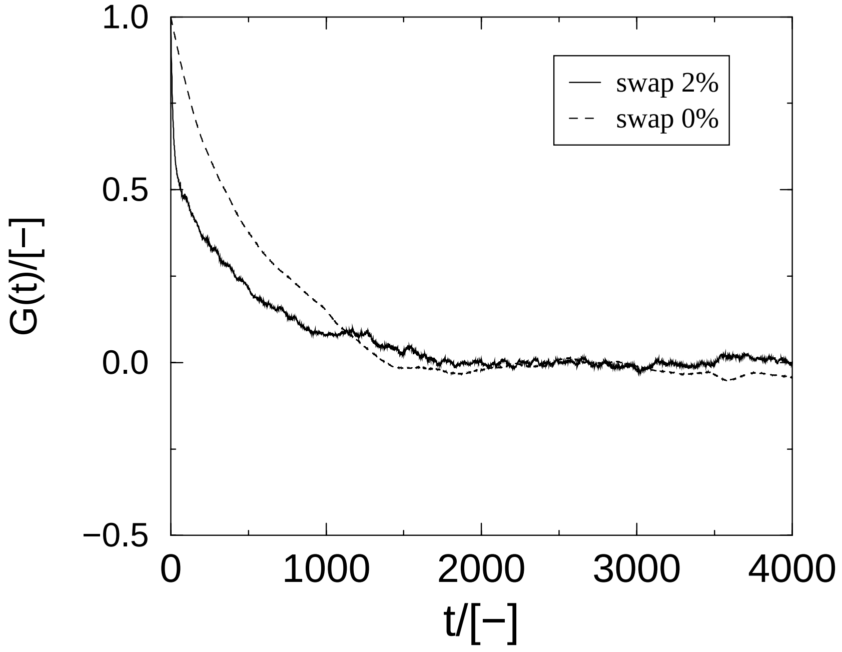

Figure 6.9: Energy autocorrelation function for $i = 8$.

Bibliography

[1] Meier, W.M.; Olson, D.H.; Baerlocher, Ch., *Atlas of Zeolite Structure Types*, 4th ed. Elsevier; Amsterdam, 1996.

[2] Flanigen, E.M; Bennett, J.M.; Grose, R.W.; Cohen, J.P.; Patton, R.L.; Kirchener, R.M.; Smith, J.V. *Nature* **1978**, *271*, 512–516.

[3] Ruthven, D.M., *Principles of Adsorption and Adsorption Processes* John Wiley; New York, 1984.

[4] Bekkum, H. van; Flaningen, E.M.; Jansen, J.C. (editors), *Introduction to Zeolite Science and Practice* Elsevier; Amsterdam, 1991.

[5] Maxwell, I.E.; Stork, W.H.J., in *Introduction to Zeolite Science and Practice*, Studies in Surface Science and Catalysis, edited by Bekkum, H. van; Flaningen, E.M.; Jansen, J.C. Elsevier; Amsterdam, 1991.

[6] Miller, S.J., in *Zeolites and Related Microporous Materials: State of the Art 1994*, Studies in Surface Science and Catalysis, edited by Weitkamp, J.; Karge, H.G.; Pfeifer, H.; Hölderich, W. Elsevier; Amsterdam, 1994, Vol. 84, pp. 2319–2326.

[7] Miller, S. J. *Micropor. Matt.* **1994**, *2*, 439–449.

[8] Ernst, S.; Kokotailo, G.T.; Kumar, R.; Weitkamp, J., in *Proc. Int. Congr. Catal., 9th*, edited by Phillips, M.J.; Ternan, M. Chem. Inst. Can.; Ottawa, Ont., 1988, Vol. 1, pp. 388–395.

[9] Ernst, S.; Weitkamp, J.; Martens, J.A.; Jacobs, P.A. *Appl. Catal.* **1989**, *48*, 137–148.

[10] Souverijns, W.; Martens, J.A.; Froment, G.F.; Jacobs, P.A. *J. Catal.* **1998**, *174*, 177–184.

[11] Mériaudeau, P.; Tuan, Vu.A.; Sapaly, G.; Nghiem, Vu.T.; Naccache, C., in *Proceedings of the 12th International Zeolite Conference*, Materials Research Society, edited by Tracy, M.M.J.; Marcus, B.K.; Bisher, M.E.; Higgins, J.B. Materials Research Society; Warrendale, PA., 1999, Vol. IV, pp. 2913–2920.

[12] Bendoraitis, J.G.; Chester, A.W.; Dwyer, F.G.; Garwood, W.E., in *New Developments in Zeolite Science and Technology*, Proc. of the 7th Int. Zeolite Conference, edited by Murakami, Y.; Iijima, A; Ward, J.W. Elsevier; Amsterdam, 1986, Vol. 28, pp. 669–675.

[13] Ernst, S.; Kumar, R.; Weitkamp, *Catal. Today* **1988**, *3*, 1–10.

[14] Maesen, Th.L.M.; Schenk, M.; Vlugt, T.J.H.; Jonge, J.P. de; Smit, B. *J. Catal.* **1999**, *188*, 403–412.

[15] Haag, W.O., in *Zeolites and Related Microporous Materials: State of the Art 1994*, Studies in Surface Science and Catalysis, edited by Weitkamp, J.; Karge, H.G.; Pfeifer, H.; Hölderich, W. Elsevier; Amsterdam, 1994, Vol. 84, pp. 1375–1394.

[16] For an ideal gas, the chemical potential μ is related to the density ρ by $\mu = \ln\left(\rho\Lambda^3\right)/\beta$.

[17] Stach, H.; Thamm, H.; Jänchen, J.; Fiedler, K.; Schirmer, W., in *New Developments in Zeolite Science and Technology*, Proc. of the 6th Int. Zeolite Conference, edited by Olsen, D.; Bisio, A. Butterworth; Guildford, UK, 1984, pp. 225–231.

[18] Falcioni, M.; Deem, M.W. *J. Chem. Phys.* **1999**, *110*, 1754–1766.

[19] http://www.iza-sc.ethz.ch/IZA-SC

[20] Smit, B.; Maesen, Th.L.M. *Nature* **1995**, *374*, 42–44.

[21] Vlugt, T.J.H.; Zhu, W.; Kapteijn, F.; Moulijn, J.A.; Smit, B.; Krishna, R. *J. Am. Chem. Soc.* **1998**, *120*, 5599–5600.

[22] Bates, S.P.; Santen, R.A. van *Advances in Catalysis* **1998**, *42*, 1–114.

[23] Auerbach, S.M. *Int. Rev. Phys. Chem.* **2000**, *19*, 155–198.

[24] Bezus, A.G.; Kiselev, A.V.; Lopatkin, A.A.; Du, P.Q. *J. Chem. Soc., Faraday Trans. II* **1978**, *74*, 367–379.

[25] Nusterer, E.; Blöchl, P.E.; Schwarz, K. *Chem. Phys. Let.* **1996**, *253*, 448–455.

[26] Schwarz, K.; Nusterer, E.; Blöchl, P.E. *Catalysis Today* **1999**, *50*, 501–509.

[27] Car, R.; Parrinello, M. *Phys. Rev. Lett.* **1985**, *55*, 2471–2474.

[28] Swope, W.C.; Andersen, H.C.; Berens, P.H.; Wilson, K.R. *J. Chem. Phys.* **1982**, *76*, 637–649.

[29] Frenkel, D.; Smit, B., *Understanding Molecular Simulations: from Algorithms to Applications* Academic Press; San Diego, 1996.

[30] Chandler, D. *J. Chem. Phys.* **1978**, *68*, 2959–2970.

[31] Metropolis, N.; Rosenbluth, A.W.; Rosenbluth, M.N.; Teller, A.N.; Teller, E. *J. Chem. Phys.* **1953**, *21*, 1087–1092.

[32] Allen, M.P.; Tildesley, D.J., *Computer Simulation of Liquids* Clarendon Press; Oxford, 1987.

[33] Rapaport, D.C., *The art of molecular dynamics simulation* Cambridge University Press; Cambridge, 1995.

[34] Deem, M.W. *AIChE Journal* **1998**, *44*, 2569–2596.

[35] Vlugt, T.J.H.; Martin, M.G.; Smit, B.; Siepmann, J.I.; Krishna, R. *Mol. Phys.* **1998**, *94*, 727–733.

[36] Vlugt, T.J.H.; Krishna, R.; Smit, B. *J. Phys. Chem. B* **1999**, *103*, 1102–1118.

[37] Vlugt, T.J.H. *Mol. Sim.* **1999**, *23*, 63–78.

[38] Consta, S.; Vlugt, T.J.H.; Wichers Hoeth, J.; Smit, B.; Frenkel, D. *Mol. Phys.* **1999**, *97*, 1243–1254.

[39] Meirovitch, H. *J. Phys. A* **1982**, *15*, L735–L741.

[40] Meirovitch, H. *J. Chem. Phys.* **1988**, *89*, 2514–2522.

[41] Grassberger, P. *Phys. Rev. E* **1997**, *56*, 3682–3693.

[42] Pablo, J.J.de ; Yan, Q.; Escobedo, F.A. *Annu. Rev. Phys. Chem.* **1999**, *50*, 377–411.

[43] Siepmann, J.I.; Frenkel, D. *Mol. Phys.* **1992**, *75*, 59–70.

[44] Frenkel, D.; Mooij, G.C.A.M.; Smit, B. *J. Phys.: Condens. Matter* **1992**, *4*, 3053–3076.

[45] Pablo, J.J.de ; Laso, M.; Suter, U.W. *J. Chem. Phys.* **1992**, *96*, 6157–6162.

[46] Siepmann, J.I., in *Computer simulation of biomolecular systems: theoretical and experimental applications*, edited by Gunsteren, W.F. van; Weiner, P.K.; Wilkinson, A.J. Escom Science Publisher; Leiden, 1993, pp. 249–264.

[47] Siepmann, J.I.; Karaborni, S.; Smit, B. *J. Am. Chem. Soc.* **1993**, *115*, 6454–6455.

[48] Siepmann, J.I.; Karaborni, S.; Smit, B. *Nature* **1993**, *365*, 330–332.

[49] Smit, B.; Karaborni, S.; Siepmann, J.I. *J. Chem. Phys.* **1995**, *102*, 2126–2140, erratum: *J. Chem. Phys.* **1998**, 109, 352.

[50] Martin, M.G.; Siepmann, J.I. *J. Am. Chem. Soc.* **1997**, *119*, 8921-8924.

[51] Mackie, A.D.; Tavitian, B.; Boutin, A.; Fuchs, A.H. *Mol. Sim.* **1997**, *19*, 1–15.

[52] Mundy, C.J.; Balasubramanian, S.; Bagchi, K.; Siepmann, J.I.; Klein, M.L. *Faraday Discuss.* **1996**, *104*, 17–37.

[53] Siepmann, J.I.; Martin, M.G.; Mundy, C.J.; Klein, M.L. *Mol. Phys.* **1997**, *90*, 687–693.

[54] Zhuravlev, N.D.; Siepmann, J.I. *Fluid Phase Equilibria* **1997**, *134*, 55–61.

[55] Cui, S.T.; Cummings, P.T.; Cochran, H.D. *Fluid Phase Equilibria* **1997**, *141*, 45–61.

[56] Nath, S.K.; Escobedo, F.A.; Pablo, J.J.de ; Patramai, I. *Ind. Eng. Chem. Res.* **1998**, *37*, 3195–3202.

[57] Nath, S.K.; Escobedo, F.A.; Pablo, J.J.de *J. Chem. Phys.* **1998**, *108*, 9905–9911.

[58] Chen, B.; Martin, M.G.; Siepmann, J.I. *J. Phys. Chem. B* **1998**, *102*, 2578–2586.

[59] Martin, M.G.; Siepmann, J.I. *J. Phys. Chem. B* **1998**, *102*, 2569–2577.

[60] Chen, B.; Siepmann, J.I. *J. Phys. Chem. B* **1999**, *103*, 5370–5379.

[61] Neubauer, B.; Tavitian, B.; Boutin, A.; Ungerer, P. *Fluid Phase Equilibria* **1999**, *161*, 45–62.

[62] Neubauer, B.; Delhommelle, J.; Boutin, A.; Tavitian, B.; Fuchs, A.H. *Fluid Phase Equilibria* **1999**, *155*, 167–176.

[63] Martin, M.G.; Siepmann, J.I. *J. Phys. Chem. B* **1999**, *103*, 4508–4517.

[64] Delhomelle, J.; Boutin, A.; Tavitian, B.; Mackie, A.D.; Fuchs, A.H. *Mol. Phys.* **1999**, *96*, 1517–1524.

[65] Martin, M.G.; Chen, B.; Siepmann, J.I. *J. Phys. Chem. B* **2000**, *104*, 2415–2423.

[66] Nath, S.K.; Pablo, J.J.de *Mol. Phys.* **2000**, *98*, 231–238.

[67] Neubauer, B.; Boutin, A.; Tavitian, B.; Fuchs, A.H. *Mol. Phys.* **1999**, *97*, 769–776.

[68] Errington, J.R.; Panagiotopoulos, A.Z. *J. Chem. Phys.* **1999**, *111*, 9731–9738.

[69] Smit, B.; Siepmann, J.I. *Science* **1994**, *264*, 1118–1120.

[70] Smit, B. *J. Phys. Chem.* **1995**, *99*, 5597–5603.

[71] Maginn, E.J.; Bell, A.T.; Theodorou, D.N. *J. Phys. Chem.* **1995**, *99*, 2057–2079.

[72] Bates, S.P.; Well, W.J.M. van; Santen, R.A. van; Smit, B. *J. Am. Chem. Soc.* **1996**, *118*, 6753–6759.

[73] Bates, S.P.; Well, W.J.M. van; Santen, R.A. van; Smit, B. *J. Phys. Chem.* **1996**, *100*, 17573–17581.

[74] Bates, S.P.; Well, W.J.M. van; Santen, R.A. van; Smit, B. *Mol. Sim.* **1997**, *19*, 301–318.

[75] Bandyopadhyay, S.; Yashonath, S. *J. Phys. Chem. B* **1997**, *101*, 5675–5683.

[76] Well, W.J.M. van; Cottin, X.; Haan, J.W. de; Santen, R.A. van; Smit, B. *Angew. Chem. (Int. Ed.)* **1998**, *37*, 1081–1083.

[77] Well, W.J.M. van; Cottin, X.; Haan, J.W. de; Smit, B.; Nivarthy, G.; Lercher, J.A.; Hooff, J.H.C. van; Santen, R.A. van *J. Phys. Chem. B* **1998**, *102*, 3945–3951.

[78] Well, W.J.M. van; Cottin, X.; Smit, B.; Hooff, J.H.C. van; Santen, R.A. van *J. Phys. Chem. B* **1998**, *102*, 3952–3958.

[79] Well, W.J.M. van; Janchen, J.; Haan, J.W. de; Santen, R.A. van *J. Phys. Chem. B* **1999**, *103*, 1841–1853.

[80] Macedonia, M.D.; Maginn, E.J. *Mol. Phys.* **1999**, *96*, 1375–1390.

[81] Macedonia, M.D.; Maginn, E.J. *Fluid Phase Equilibria* **1999**, *160*, 19–27.

[82] Macedonia, M.D.; Moore, D.D.; Maginn, E.J.; Olken, M.M. *Langmuir* **2000**, *16*, 3823–3834.

[83] Dijkstra, M. *J. Chem. Phys.* **1997**, *107*, 3277–3288.

[84] Dijkstra, M. *Thin Solid Films* **1999**, *330*, 14–20.

[85] Deem, M.W.; Bader, J.S. *Mol. Phys.* **1996**, *87*, 1245–1260.

[86] Wu, M.G.; Deem, M.W. *Mol. Phys.* **1999**, *97*, 559–580.

[87] Wu, M.G.; Deem, M.W. *J. Chem. Phys.* **1999**, *111*, 6625–6632.

[88] Ploeg, P. van der; Berendsen, H.J.C. *J. Chem. Phys.* **1982**, *76*, 3271–3276.

[89] Jorgensen, W.L.; Madura, J.D.; Swenson, C.J. *J. Am. Chem. Soc.* **1984**, *106*, 6638–6646.

[90] In section 2.4, we will show that one has to be careful to split the potential energy because different interactions might not be independent.

[91] Esselink, K.; Loyens, L.D.J.C.; Smit, B. *Phys. Rev. E* **1995**, *51*, 1560–1568.

[92] Snurr, R.Q.; Bell, A.T.; Theodorou, D.R. *J. Phys. Chem.* **1993**, *97*, 13742–13752.

[93] Mooij, G.C.A.M.; Frenkel, D. *Mol. Sim.* **1996**, *17*, 41–55.

[94] Loyens, L.D.J.C.; Smit, B.; Esselink, K. *Mol. Phys.* **1995**, *86*, 171–183.

[95] In such a cell-list algorithm, particles are placed on a grid with a size of at least the cut-off radius. Particles will only have interactions with particles in the same or neighboring cells.

[96] Widom, B. *J. Chem. Phys.* **1963**, *39*, 2802–2812.

[97] Martyna, G.J.; Tuckerman, M.; Tobias, D.J.; Klein, M.L. *Mol. Phys.* **1996**, *87*, 1117–1157.

[98] MPI: A Message-Passing Interface Standard (http://www.mpi-forum.org)

[99] http://www-unix.mcs.anl.gov/mpi/mpich

[100] http://www.redhat.com

[101] http://www.mpi.nd.edu/lam/

[102] http://molsim.chem.uva.nl/cluster

[103] http://molsim.chem.uva.nl/tampert/cluster

[104] Wilson, E.K. *Chemical and Engineering News* **2000**, *10*, 27–31.

[105] For a small number of chains we do not expect large differences between the machines.

[106] I would like to thank Daan Frenkel for this suggestion.

[107] Smit, B.; Siepmann, J.I. *J. Phys. Chem.* **1994**, *98*, 8442–8452.

[108] Bernardo, D.N.; Ding, Y.; Krogh-Jespersen, K.; Levy, R.M. *J. Phys. Chem. B* **1994**, *98*, 4180–4187.

[109] This algorithm looks a bit like the Eurovision Song Contest; in order to participate in this event one has to win the National Song Contest (a chain has to be selected on a processor before it can compete with other chains from other processors). Who likes singing anyway ?!?

[110] Rosenbluth, M.N.; Rosenbluth, A.W. *J. Chem. Phys.* **1955**, *23*, 356–359.

[111] Consta, S.; Wilding, N.B.; Frenkel, D.; Alexandrowicz, Z. *J. Chem. Phys.* **1999**, *110*, 3220–3228.

[112] Although the limit $u_i \to -\infty$ does not exist in statistical mechanics, it does exist for the function $p_i(u_i)$.

[113] When simulating molecules with internal (bond and torsion) potentials, it may be advantageous to generate trial segments according to the intra-molecular Boltzmann distribution. Alternatively, it is also possible to take bonded intra-molecular interactions into account in equation 3.2. However, this will lead to an inefficient algorithm because in that case many trial directions will be found closed on the basis on their internal energy.

[114] Frenkel, D., in *Computer Simulation in Chemical Physics*, NATO ASI, edited by Allen, M.P.; Tildesley, D.J. Kluwer; Dordrecht, 1993, pp. 93–152.

[115] There is no need to split u_{intra} into short-range and long-range parts.

[116] One has to go where no feeler has gone before.

[117] Escobedo, F.A.; Pablo, J.J.de *J. Chem. Phys.* **1995**, *102*, 2636–2652.

[118] Vendruscolo, M. *J. Chem. Phys.* **1997**, *106*, 2970–2975.

[119] Wick, C.D.; Siepmann, J.I. *Macromolecules* **2000**, *submitted.*

[120] Hoogerbrugge, P.J.; Koelman, J.M.V.A. *Europhys. Lett.* **1992**, *19*, 155–160.

[121] Groot, R.D.; Warren, P.B. *J. Chem. Phys.* **1997**, *107*, 4423–4435.

[122] Pagonabarraga, I.; Hagen, M.H.J.; Frenkel, D. *Europhys. Lett.* **1998**, *42*, 377–382.

[123] Press, W.H.; Flannery, B.P.; Teukolsky, S.A.; Vetterling, W.T., *Numerical Recipes: The art of scientific computing* Cambridge University Press; Cambridge, 1986.

[124] Stach, H.; Lohse, U.; Thamm, H.; Schirmer, W. *Zeolites* **1986**, *6*, 74–90.

[125] Lohse, U.; Fahlke, B. *Chem. Techn.* **1983**, *35*, 350–353.

[126] Rakhmatkariev, G.U.; Zhalalov, Kh.R.; Akhmedov, K.S. *Uzb. Khim. Zh.* **1988**, *3*, 68–70.

[127] Dubinin, M.M.; Rakhmatkariev, G.U.; Isirikyan, A.A. *Izv. Akad. Nauk SSSR, Ser. Khim.* **1989**, *10*, 2333-2335.

[128] Richard, R.E.; Rees, L.V.C. *Langmuir* **1987**, *3*, 335–340.

[129] Well, W.J.M. van; Wolthuizen, J.P.; Smit, B.; Hooff, J.H.C. van; Santen, R.A. van *Angew. Chem. (Int. Ed.)* **1995**, *34*, 2543–2544.

[130] Olsen, D.H.; Reischmann, P.T. *Zeolites* **1996**, *17*, 434–436.

[131] Sun, M.S.; Talu, O.; Shah, D.B. *J. Phys. Chem.* **1996**, *100*, 17276–17280.

[132] Yang, Y.; Rees, L.V.C. *Micropor. Matt.* **1997**, *12*, 117–122.

[133] Yang, Y.; Rees, L.V.C. *Micropor. Matt.* **1997**, *12*, 223-228.

[134] Millot, B.; Méthivier, A.; Jobic, H. *J. Phys. Chem. B* **1998**, *102*, 3210–3215.

[135] Zhu, W.; Graaf, J.M. van de; Broeke, L.J.P. van den; Kapteijn, F.; Moulijn, J.A. *Ind. Eng. Chem. Res.* **1998**, *37*, 1934–1942.

[136] Sun, M.S.; Shah, D.B.; Xu, H.H.; Talu, O. *J. Phys. Chem.* **1998**, *102*, 1466–1473.

[137] Cavalcante Jr., C.L.; Ruthven, D.M. *Ind. Eng. Chem. Rev.* **1995**, *34*, 177–184.

[138] Ryckaert, J.P.; Bellemans, A. *Faraday Discuss. Chem. Soc.* **1978**, *66*, 95–106.

[139] It is important to note that the united-atom approach is not suitable to describe solid or high density liquid phases [253–255]. In our case, however, the zeolite itself is the most important factor that determines the configuration of the alkane molecules so we feel that this approach is justified here.

[140] In ref. [256] it is shown that small changes in zeolite structure may have a large effect on adsorption isotherms when molecules are tightly fitting. Therefore, flexibility of the framework should be included in such simulations.

[141] June, R.L.; Bell, A.T.; Theodorou, D.N. *J. Phys. Chem.* **1992**, *96*, 1051–1060.

[142] Smit, B.; Loyens, L.D.J.C.; Verbist, G.L.M.M. *Faraday Discuss.* **1997**, *106*, 93–104.

[143] Verlet, L.; Weis, J.J. *Mol. Phys.* **1972**, *24*, 1013–1024.

[144] One could, for example, fit σ_{OO} and ϵ_{OO} and use the Jorgensen mixing rules [89] and the alkane-alkane interactions from table 4.2 to compute the alkane-zeolite interaction parameters. The advantage of this approach is that the number of parameters that have to be fitted is reduced to two. Alternatively, one could also include interactions with the Si atoms of the framework which will lead to four adjustable parameters.

[145] Smit, B. *Mol. Phys.* **1995**, *85*, 153–172.

[146] In ref. [257] it is shown that MC schemes in which different trial moves are performed in a fixed order also sample the correct distribution.

[147] Panagiotopoulos, A.Z. *Int. J. Thermophys.* **1989**, *10*, 447.

[148] Du, Z.; Vlugt, T.J.H.; Smit, B.; Manos, G. *AIChE Journal* **1998**, *44*, 1756–1764.

[149] Abdul-Rehman, H.B.; Hasanain, M.A.; Loughlin, K.F. *Ind. Eng. Chem. Res.* **1990**, *29*, 1525–1535.

[150] The data in ref. [149] have been corrected for the binder by assuming that this binder does not contribute to the adsorption.

[151] Rees, L.V.C.; Brückner, P.; Hampson, J. *Gas Sep. Purif.* **1991**, *5*, 67–75.

[152] Weidong Zhu, personal communication.

[153] Gregg, S.J.; Sing, K.S.W., *Adsorption, Surface Area and Porosity* Academic Press; London, 1982.

[154] Evans, R., in *Liquides aux Interfaces/Liquids at interfaces*, Les Houches, Session XLVIII, 1988, edited by Charvolin, J.; Joanny, J.F.; Zinn-Justin, J. North Holland; Amsterdam, 1990, pp. 1–98.

[155] Radhkrishnan, R.; Gubbins, K.E. *Phys. Rev. Lett.* **1997**, *79*, 2847–2850.

[156] Maris, T.; Vlugt, T.J.H.; Smit, B. *J. Phys. Chem. B* **1998**, *102*, 7183–7189.

[157] Recently, there is a discussion in the literature whether pseudo-one-dimensional phase transitions can occur in molecular sieves [155, 156].

[158] Recent simulations by Du *et al.* [148] indicate that for ethane at high pressure also an inflection may be observed. However, experimental evidence for this inflection is still lacking.

[159] Lohse, U.; Thamm, H.; Noack, M.; Fahlke, B. *J. Incl. Phen.* **1987**, *5*, 307–313.

[160] Eder, F., Thermodynamics and siting of alkane sorption in molecular sieves Ph.D. thesis, Universiteit Twente, 1996.

[161] Eder, F.; Lercher, J.A. *Zeolites* **1997**, *8*, 75–81.

[162] Eder, F.; Lercher, J.A. *J. Phys. Chem. B* **1997**, *101*, 1273–1278.

[163] Eder, F.; Stockenhuber, M.; Lercher, J.A. *J. Phys. Chem. B* **1997**, *101*, 5414–5419.

[164] Eder, F. and Lercher, J.A. Unpublished data (used with permission of the authors).

[165] Ashtekar, S.; McLeod, A.S.; Mantle, M.D.; Barrie, P.J.; Gladden, L.F.; Hastings, J.J. *J. Phys. Chem. B* **2000**, *in press*.

[166] Zhu, W.; Kapteijn, F.; Moulijn, J.A. *Phys. Chem. Chem. Phys.* **2000**, *2*, 1989–1995.

[167] June, R.L.; Bell, A.T.; Theodorou, D.N. *J. Phys. Chem.* **1990**, *94*, 1508–1516.

[168] Schuring, D.; Jansen, A.P.J.; Santen, R.A. van *J. Phys. Chem. B* **2000**, *104*, 941–948.

[169] Runnebaum, R.C.; Maginn, E.J. *J. Phys. Chem. B* **1997**, *101*, 6394–6408.

[170] Bouyermaouen, A.; Bellemans, A. *J. Chem. Phys.* **1998**, *108*, 2170–2172.

[171] Leonidas, N.G.; Theodorou, D.N. *J. Phys. Chem. B* **1999**, *103*, 3380–3390.

[172] Webb III, E.B.; Grest, G.S.; Mondello, M. *J. Phys. Chem. B* **1999**, *103*, 4949–4959.

[173] I would like to thank Marcus G. Martin for pointing this out.

[174] Hagler, A.T.; Lifson, S.; Dauber, P. *J. Am. Chem. Soc.* **1979**, *101*, 5122–5130.

[175] Micke, A.; Bülow, M; Kocirik, M.; Struve, P. *J. Chem. Phys.* **1994**, *98*, 12337–12344.

[176] Sung, W.; Park, P.J. *Phys. Rev. Lett.* **1996**, *77*, 783–786.

[177] Wang, Y.; Hill, K.; Harris, J.G. *J. Phys. Chem.* **1994**, *100*, 3276–3285.

[178] Doelle, H.J.; Heering, J.; Riekert, L.; Marosi, L. *J. Catal.* **1981**, *71*, 27–40.

[179] Savitz, S.; Siperstein, F.; Gorte, R.J.; Myers, A.L. *J. Phys. Chem. B* **1998**, *102*, 6865–6872.

[180] Hyun, S.H.; Danner, R.P. *AIChE Symp. Ser.* **1982**, *78(219)*, 19–28.

[181] Hufton, J.R. *J. Phys. Chem.* **1991**, *95*, 8836–8839.

[182] Hufton, J.R.; Danner, R.P. *AIChE Journal* **1993**, *39*, 954–961.

[183] Yamazaki, T.; Watanuki, I.; Ozawa, S.; Ogino, Y. *Nippon Kagaku Kaishi* **1987**, *8*, 1535–1540.

[184] Yamazaki, T.; Watanuki, I.; Ozawa, S.; Ogino, Y. *Langmuir* **1988**, *4*, 433–438.

[185] Papp, H.; Hinsen, W.; Do, N.T.; Baerns, M. *Therm. Acta* **1984**, *82*, 137–148.

[186] Golden, T.C.; Sircar, S. *J. Colloid Interface Sci.* **1989**, *162*, 182–188.

[187] Dunne, J. A.; Mariwala, R.; Rao, M.; Sircar, S.; Gorte, R. J.; Myers, A. L. *Langmuir* **1996**, *12*, 5888–5895.

[188] Chiang, A.S.; Dixon, A.G.; Ma, Y.H. *Chem. Eng. Sci.* **1984**, *39*, 1461–1468.

[189] Hampson, J.A.; Rees, L.V.C. *J. Chem. Soc. Faraday Trans.* **1993**, *89*, 3169–3176.

[190] Dunne, J.A.; Rao, M.; Sircar, S.; Gorte, R.J.; Myers, A.L. *Langmuir* **1996**, *12*, 5896–5904.

[191] Thamm, H. *Zeolites* **1987**, *7*, 341–346.

[192] Bülow, M.; Schodder, H.; Rees, L.V.C.; Richards, R.E., in *New Developments in Zeolite Science and Technology*, Proc. of the 7th Int. Zeolite Conference, edited by Murakami, Y.; Iijima, A; Ward, J.W. Elsevier; Amsterdam, 1986, pp. 579–586.

[193] Kiselev, A.V.; Lopatkin, A.A.; Shulga, A.A. *Zeolites* **1985**, *5*, 261–267.

[194] Shen, D.; Rees, L.V. *Zeolites* **1991**, *119*, 684–689.

[195] Thamm, H.; Stach, H.; Schirmer, W.; Fahlke, B. *Z. phys. Chemie, Leipzig* **1982**, *263*, 461–469.

[196] Thamm, H.; Stach, H.; Fiebig, W. *Zeolites* **1983**, *3*, 95–97.

[197] Lechert, H.; Schweiter, W., in *New Developments in Zeolite Science and Technology*, Proc. of the 6th Int. Zeolite Conference, edited by Olsen, D.; Bisio, A. Butterworth; Guildford, UK., 1984, pp. 210–216.

[198] Millot, B.; Méthivier, A.; Jobic, H.; Clemençon, I.; Rebours, B. *Langmuir* **1999**, *15*, 2534–2539.

[199] Thamm, H.; Regent, N.I. *Z. Chem.* **1982**, *22*, 232–233.

[200] Ding, T.; Ozawa, S.; Ogino, Y. *Zhejiang Daxue Xuebao* **1988**, *22*, 124.

[201] Otto, K.; Montreuil, C.N.; Todor, O.; McCabe, R.W.; Gandhi, H.S. *Ind. Eng. Chem. Res.* **1991**, *30*, 2333–2340.

[202] Hufton, J.R.; Danner, R.P. *Chem. Eng. Sci.* **1991**, *46*, 2079–2091.

[203] Krishna, R.; Smit, B.; Vlugt, T.J.H. *J. Phys. Chem. A* **1998**, *102*, 7727–7730.

[204] Krishna, R.; Vlugt, T.J.H.; Smit, B. *Chem. Eng. Sci.* **1999**, *54*, 1751–1757.

[205] Dunne, J.A.; Rao, M.; Sircar, S.; Gorte, R.J.; Myers, A.L. *Langmuir* **1997**, *13*, 4333–4341.

[206] Krishna, R. *Chem. Eng. Sci.* **1993**, *48*, 845–861.

[207] Krishna, R. *Gas Separation and Purification* **1993**, *7*, 91–104.

[208] Shah, D.B.; Guo, C.J.; Hayhurst, D.T. *J. Chem.Soc. Farad. Trans.* **1995**, *91*, 1143–1146.

[209] Graaf, J. van de; Kapteijn, F.; Moulijn, J.A. *A.I.Ch.E.J* **1999**, *45*, 497–511.

[210] Kapteijn, F.; Moulijn, J.A.; Krishna, R. *Chem. Eng. Sci.* **2000**, *55*, 2923–2930.

[211] Schiesser, W.E., *The numerical method of lines: Integration of partial differential equations* Academic Press; San Diego, 1991.

[212] Krishna, R.; Broeke, L.J.P. van den *Chem. Eng. Jl* **1995**, *57*, 155–162.

[213] Krishna, R. *Chem. Eng. Sci.* **1990**, *45*, 1779–1791.

[214] Taylor, R.; Krishna, R., *Multicomponent Mass Transfer* John Wiley and Sons; New York, 1993.

[215] Krishna, R.; Wesselingh, J.A. *Chem. Eng. Sci.* **1997**, *52*, 861–911.

[216] Funke, H.H.; Argo, A.M.; Falconer, J.L.; Noble, R.D. *Ind. Eng. Chem. Res.* **1997**, *36*, 137–143.

[217] Vlugt, T.J.H.; Dellago, C.; Smit, B. *J. Chem. Phys.* **2000**, *submitted.*

[218] Snurr, R.Q.; Bell, A.T.; Theodorou, D.R. *J. Phys. Chem.* **1994**, *98*, 5111–5119.

[219] Forester, T.R.; Smith, W. *J. Chem. Soc. Faraday Trans.* **1997**, *93*, 3249–3257.

[220] Kärger, J.; Ruthven, D.M., *Diffusion in Zeolites and other Microporous Solids* Wiley & Sons; New York, 1992.

[221] Voter, A.F.; Doll, J.D. *J. Chem. Phys.* **1985**, *82*, 80–92.

[222] Mosell, T.; Schrimpf, G.; Hahn, C.; Brickmann, J. *J. Phys. Chem.* **1996**, *100*, 4571–4581.

[223] Mosell, T.; Schrimpf, G.; Brickmann, J. *J. Phys. Chem.* **1996**, *100*, 4582–4590.

[224] Mosell, T.; Schrimpf, G.; Brickmann, J. *J. Phys. Chem. B* **1997**, *101*, 9476–9484.
[225] Mosell, T.; Schrimpf, G.; Brickmann, J. *J. Phys. Chem. B* **1997**, *101*, 9485–9494.
[226] Jousse, F.; Auerbach, S.M. *J. Chem. Phys.* **1997**, *107*, 9629–9636.
[227] Dellago, C.; Bolhuis, P.G.; Csajka, F.S.; Chandler, D. *J. Chem. Phys.* **1998**, *108*, 1964–1977.
[228] Bolhuis, P.G.; Dellago, C.; Geissler, P.L.; Chandler, D. *J. Phys.: Condens. Matter* **2000**, *12*, A147–A152.
[229] Geissler, P.L.; Dellago, C.; Chandler, D. *J. Phys. Chem. B* **1999**, *103*, 3706–3710.
[230] Geissler, P.L.; Dellago, C.; Chandler, D. *Phys. Chem. Chem. Phys.* **1999**, *1*, 1317–1322.
[231] Geissler, P.L.; Dellago, C.; Chandler, D.; Hutter, J.; Parrinello, M. *Chem. Phys. Lett.* **2000**, *321*, 225–230.
[232] Bolhuis, P.G.; Dellago, C.; Chandler, D. *Faraday Discuss.* **1998**, *110*, 421–436.
[233] Bolhuis, P.G.; Dellago, C.; Chandler, D. *Proceedings of the National Academy of Sciences* **2000**, *97*, 5877–5882.
[234] Dellago, C.; Bolhuis, P.G.; Chandler, D. *J. Chem. Phys.* **1999**, *110*, 6617–6625.
[235] Pratt, L.R *J. Chem. Phys.* **1986**, *9*, 5045–5048.
[236] Note that this is not possible when a weight-function $W(\lambda(x_t), i)$ is used because then the weight of a path is an explicit function of the endpoint of the path (see, for example, equation 6.11).
[237] Geyer, C.J.; Thompson, E.A. *J. Am. Stat. Assoc.* **1995**, *90*, 909–920.
[238] Tuckerman, M.; Berne, B.J.; Martyna, G.J. *J. Chem. Phys.* **1992**, *97*, 1990–2001.
[239] Do not underestimate the power of detailed balance.
[240] Levesque, D.; Verlet, L. *J. Stat. Phys.* **1993**, *72*, 519–537.
[241] Bandyopadhyay, S.; Yashonath, S. *J. Phys. Chem.* **1995**, *99*, 4286–4292.
[242] Kärger, J. *J. Phys. Chem.* **1991**, *95*, 5558–5560.
[243] Jousse, F.; Auerbach, S.M.; Vercauteren, D.P. *J. Chem. Phys.* **2000**, *112*, 1531–1540.
[244] Coppens, M.O.; Bell, A.T.; Chakraborty, A.K. *Chem. Eng. Sci.* **1998**, *53*, 2053–2061.
[245] Paschek, D.; Krishna, R. *Phys. Chem. Chem. Phys.* **2000**, *2*, 2389–2394.
[246] Hufton, J.R.; Danner, R.P. *AIChE Journal* **1993**, *39*, 962–974.
[247] Shah, D.B.; Chokchai-acha, S.; Hayhurst, D.T. *J. Chem. Soc. Faraday Trans.* **1991**, *89*, 3161–3167.
[248] Nijhuis, T.A.; Broeke, L.J.P. van den; Linders, M.J.G.; Graaf, J.M. van de; Kapteijn, F.; Makkee, M.; Moulijn, J.A. *Chem. Eng. Sci.* **1999**, *54*, 4423–4436.
[249] Bakker, W.J.W.; Broeke, L.J.P. van den; Kapteijn, F.; Moulijn, J.A. *A.I.Ch.E.J.* **1997**, *43*, 2203–2214.
[250] Millot, B.; Méthivier, A.; Jobic, H.; Moueddeb, H.; Bée, M. *J. Phys. Chem. B* **1999**, *103*, 1096–1101.
[251] Ruiz-Montero, M.J.; Frenkel, D.; Brey, J.J. *Mol. Phys.* **1997**, *90*, 925–941.
[252] Yan, Q.L.; Pablo, J.J.de *J. Chem. Phys.* **1999**, *111*, 9509–9516.
[253] Moller, M.A.; Tildesley, D.J.; Kim, K.S.; Quirke, N. *J. Chem. Phys.* **1991**, *94*, 8390–8401.
[254] Ryckaert, J.P.; McDonald, I.R.; Klein, M.L. *Mol. Phys.* **1989**, *67*, 957–979.
[255] Polson, J.M.; Frenkel, D. *J. Chem. Phys.* **1999**, *111*, 1501–1510.
[256] Clark, L.A.; Snurr, R.Q. *Chem. Phys. Lett.* **1999**, *308*, 155–159.
[257] Manousiouthakis, V.I.; Deem, M.W. *J. Chem. Phys.* **1999**, *110*, 2753–2756.
[258] http://www.tue.nl
[259] http://www-its.chem.uva.nl

Summary

The subject of this thesis is the study of adsorption and diffusion of alkanes in zeolites by computer simulation.

In chapter 1, a short introduction to molecular simulations is presented, as well as an introduction to the structure and industrial applications of zeolites.

In chapter 2, we discuss several extensions of Configurational-Bias Monte Carlo (CBMC). CBMC is a Monte Carlo algorithm for the computation of thermodynamic properties of chain molecules. In this algorithm, a chain molecule is grown step by step. For the insertion of a new segment, several (k) trial positions are generated of which the energy u is calculated. One of these segments is selected with a probability proportional to its Boltzmann factor. A similar procedure is applied for the old configuration. Finally, it is decided at random to accept the new chain or not (the so-called acceptance / rejection rule).

In this algorithm, biased chains are grown instead of random chains. We can correct for this bias by a modification of the acceptance / rejection rule. As the calculation of the energy of a trial segment (u) is computationally expensive, it would be advantageous to select a trial segment in a different way. A possibility is to split u into short-range and long-range parts. When chains are constructed by using the short-range part only, one is able to save much CPU time because the calculation of the long-range part is much more expensive. To correct for the bias, we have to compute the long-range interactions only for the selected configuration and not for every trial segment. For a typical simulation, a speed-up of a factor 2 to 5 can be achieved. Another possibility to speed-up CBMC simulations is to use a parallel computer. As the growth of a chain is a sequential process, it is very difficult to parallelize this task using a large number of processors. Therefore, we have studied an algorithm in which many (g) chains are grown using only short-range interactions. This task can be parallelized efficiently. When many chains are grown simultaneously, it is more likely that one of the chains is grown in a favorable configuration. One of the g chains is chosen with a probability proportional to its Rosenbluth weight and only for this chain we have to compute the long-range interactions to correct for the bias. This algorithm is more efficient than one would expect based on the individual algorithms.

Finally, we investigate the growth of branched molecules using CBMC. Due to the presence of bond-bending potentials, one has to grow all segments connected to a branched atom of an alkane molecule simultaneously.

In chapter 3, we discuss an alternative for CBMC (Recoil Growth, RG). One of the main disadvantages of CBMC is that when all trial segments have unfavorable energies, the growth of the chain will be terminated. In RG, two new concepts are introduced to solve this problem:

- a binary parameter b, which indicates whether a trial segment is considered as open or closed. b is a stochastic variable which depends on the energy of the trial position only. When a trial segment is considered as closed, it cannot be part of the chain.

- the recoil length l, which is the number of segments that the chain is allowed to retract.

For the growth of a chain, one generates a possible trial segment. When it is decided that the trial segment is open, we continue growing the chain. Otherwise, another trial segment is generated up to a maximum of k trial segments. When all k trial segments are closed, the chain retracts by one segment. The chain is allowed to retract to segment $(l_{max} - l + 1)$, in which l_{max} is the maximum length that was obtained during the construction of the chain. When the chain is not allowed to retract anymore the chain is discarded. A similar procedure is applied to the old configuration. Finally, the new chain is accepted or rejected with a certain probability. In this chapter, we have derived the correct acceptance/rejection rule for this algorithm. For long chains and high densities, RG is more than one order of magnitude more efficient than CBMC. However, RG is less suitable for parallelization using a multiple chain algorithm (which is described in chapter 2).

In chapter 4, we discuss the adsorption of linear and branched alkanes in the zeolite Silicalite. We have used the simulation techniques described in the previous chapters for this. Silicalite has a three dimensional channel structure which consists of straight and zigzag channels that cross at the intersections (see figures 1.1 en 4.1). To compute the adsorption behavior, we have fitted a force field which is able to reproduce the Henry coefficient (adsorption isotherm at low pressure) and the heat of adsorption. From CBMC simulations it turns out that linear alkanes can occupy all channels of Silicalite. For n-C_6 en n-C_7, the length of the molecule is almost identical to the length of the zigzag channel. In literature, this process is called "commensurate freezing" and causes an inflection in the adsorption isotherm of these molecules. This effect has also been observed experimentally.

The adsorption behavior of branched alkanes in Silicalite is completely different from linear alkanes. Branched alkanes are preferentially adsorbed at the intersections of Silicalite, which is due to larger available space for the branch at the intersections. At a loading of 4 molecules per unit cell Silicalite, all intersections are occupied. Additional molecules will have to reside in the channel interiors. As this is energetically unfavorable, an additional driving force is needed to force the molecules into the channel interiors. This is the cause of the inflection in the isotherm, which has also been obtained experimentally for Silicalite. All isotherms can be described well using a dual-site Langmuir isotherm.

Chapter 5 describes the adsorption of 50%-50% mixtures of linear and branched alkanes on Silicalite. We find that at low pressures, both linear as well as branched molecules are adsorbed. At high pressures, there will be a competition between these molecules because the space in the zeolite is limited. At these pressures, linear alkanes are adsorbed anywhere in the zeolite while branched alkanes are only adsorbed at the intersections. Branched alkanes disturb the structure of the linear ones. Therefore, the system can gain entropy when the branched molecules are completely squeezed out of the zeolite. This process occurs for 50%-50% mixtures of i-C_5-n-C_5, i-C_6-n-C_6 en i-C_7-n-C_7. These mixture isotherms are well described by a dual-site binary Langmuir isotherm.

As the Fick diffusion coefficient is directly related to the adsorption isotherm and the Maxwell-Stefan diffusion coefficient using the thermodynamic matrix Γ, we can describe the diffusion of alkane mixture using the Maxwell-Stefan theory. For this, we have assumed that the Maxwell-Stefan diffusivity is independent of the loading of the zeolite. This suggests a possible industrial application for the separation of linear and branched alkanes using a zeolite membrane.

In chapter 6, we study the diffusion of isobutane in Silicalite. At low pressures, isobutane is preferentially adsorbed at the intersections of Silicalite. As there is a large free energy barrier between two intersections, the jump of an isobutane molecule to a nearby intersection will be a rare event. Therefore, we cannot use conventional Molecular Dynamics (MD) to compute the jump rate (and therefore also the diffusion coefficient). To compute the diffusion coefficient, we have used transition path sampling. In these simulations, we generate an ensemble of MD tra-

jectories that connects two nearby intersections. This allows us to compute not only the jump rate but also the transition state. For isobutane, the calculated diffusivity is much lower than the experimental obtained value. Possible explanations for this are that we have neglected the flexibility of the zeolite (to save CPU time) and the large Lennard-Jones size parameter describing the alkane-zeolite interactions. The simulations show that not only the position but also the orientation of isobutane is important to localize transition states.

Samenvatting (Summary in Dutch)

Dit proefschrift gaat over computersimulaties van adsorptie en diffusie van alkanen in zeolieten.

In hoofdstuk 1 worden enkele basisbegrippen van moleculaire simulaties geïntroduceerd. Tevens wordt een korte inleiding over de structuur en industriële toepassingen van zeolieten gegeven.

In hoofdstuk 2 worden enkele uitbreidingen van Configurational-Bias Monte Carlo (CBMC) besproken. CBMC is een Monte Carlo algoritme dat gebruikt kan worden voor de berekening van thermodynamische grootheden van ketenmoleculen. In dit algoritme wordt een ketenmolecuul segment voor segment opgebouwd. Voor de insertie van een nieuw segment worden enkele (k) trial-segmenten gegenereerd en van deze trial-segmenten wordt de energie u uitgerekend. Eén van deze trial-segmenten wordt geselecteerd met een kans die evenredig is met zijn Boltzmann factor. In de praktijk betekent dit, dat het segment met de gunstigste energie wordt gekozen. Tevens wordt een soortgelijke procedure toegepast op de oude keten. Vervolgens wordt met een bepaalde kans besloten of de nieuwe keten wordt geaccepteerd of dat de oude keten behouden blijft (de zogenaamde acceptatieregel).

Ondanks dat in dit algoritme in plaats van random ketens, ketens met een bepaalde voorkeursrichting (bias) worden geconstrueerd, kan voor deze bias exact worden gecorrigeerd in de acceptatieregel. Aangezien de berekening van de energie van een trial-segment (u) een rekenintensieve operatie is, is het wenselijk een trial-segment op een andere manier te selecteren. Eén van de mogelijkheden is het splitsen van u in een potentiaal met een korte-dracht en een lange-dracht. Wanneer ketens worden geconstrueerd met uitsluitend het korte-dracht deel van u wordt veel rekentijd bespaard, aangezien de berekening van het lange-dracht deel van u verreweg de meeste rekentijd vraagt. De aanpassing van de acceptatieregels vereist de berekening van het lange-dracht deel van u alleen voor de geselecteerde configuratie en niet voor alle trial-segmenten van de gehele keten. Voor een typische simulatie levert dit een versnelling op van een factor 2 tot 5. Een andere mogelijkheid om CBMC simulaties te versnellen is het overgaan op een parallel algoritme. Dit vereist een computer met meerdere processoren. Aangezien het groeien van een keten van nature een sequentieel proces is, is dit lastig te parallelliseren over een groot aantal processoren. Daarom is gekozen voor een algoritme waarbij een groot aantal ketens (g) wordt opgebouwd met het korte-dracht deel van u. Deze taak kan gemakkelijk worden geparallelliseerd. De gedachte is, dat door meerdere ketens simultaan te construeren, de kans dat een keten in een gunstige conformatie terecht komt, wordt vergroot. Uit deze g ketens wordt de meest gunstige keten gekozen en voor deze keten wordt het lange-dracht deel van u berekend om te corrigeren voor de door dit algoritme geïntroduceerde voorkeur voor de geselecteerde configuratie. Het blijkt dat dit een bijzonder effectief algoritme oplevert.

Tevens worden de problemen die gepaard gaan bij de extensie van CBMC naar vertakte ketens in kaart gebracht. Het blijkt dat bij een vertakt alkaan, door de aanwezigheid van bond-bending potentialen, alle segmenten aan een vertakking simultaan neergezet moeten worden.

In hoofdstuk 3 wordt een alternatief voor CBMC besproken, Recoil Growth (RG). Eén van de belangrijkste nadelen van CBMC is, dat op een bepaald moment alle trial-segmenten ongunstig

kunnen zijn. Hierdoor kan de constructie van een keten vastlopen. In RG worden twee nieuwe concepten geïntroduceerd om dit te verbeteren:

- een binaire parameter b die aangeeft of een segment open of gesloten is. De kans op een bepaalde waarde van b is een functie van de energie u van dit segment. Wanneer wordt bepaald dat een segment gesloten is, kan dit segment nooit deel uitmaken van de geselecteerde keten.
- de recoil lengte l, dit is de lengte waarover een keten kan teruggroeien.

Voor het opbouwen van een keten wordt telkens een trial-segment gegenereerd. Wanneer dit segment open is, wordt verder gegaan met het volgende segment. Wanneer dit segment gesloten is, wordt een ander trial-segment gegenereerd tot een maximum van k segmenten. Zijn alle k segmenten gesloten, dan kan de keten een stap teruggroeien tot een maximum van $(l_{max} - l + 1)$ segmenten, waarin l_{max} de maximale lengte is die bereikt is tijdens de constructie van de keten. Wanneer verder teruggroeien niet meer mogelijk is, wordt de nieuwe keten verworpen. Een soortgelijke procedure wordt toegepast op de oude keten. Vervolgens wordt met een bepaalde kans de nieuwe keten aangenomen of verworpen. Hiervoor zijn in dit hoofdstuk de correcte acceptatieregels afgeleid. Het blijkt dat RG voor lange ketens en systemen met een hoge dichtheid een orde grootte efficiënter is dan CBMC. Echter, RG blijkt minder geschikt voor parallellisatie met het algoritme dat in hoofdstuk 2 is beschreven.

Hoofdstuk 4 beschrijft uitgebreid het adsorptiegedrag van lineaire en vertakte alkanen in het zeoliet Silicalite. Hiervoor zijn de simulatietechnieken uit de vorige hoofdstukken gebruikt. Silicalite heeft een driedimensionale kanaalstructuur bestaande uit lineaire kanalen en zigzag kanalen die elkaar kruisen op de intersecties (zie figuren 1.1 en 4.1). Om dit adsorptiegedrag te kunnen berekenen is een krachtveld opgesteld om de interacties tussen alkanen en het zeoliet te kunnen berekenen. Dit krachtveld is zodanig gefit dat experimentele waardes van de Henry coëfficiënt (adsorptie isotherm bij lage druk) en adsorptiewarmte gereproduceerd kunnen worden. Uit de CBMC simulaties blijkt dat lineaire alkanen zich vrij kunnen bewegen over alle kanalen van Silicalite. Voor n-C_6 en n-C_7 is de lengte van het alkaan molecuul vrijwel identiek aan de lengte van het zigzag kanaal. Dit proces staat in de litteratuur bekend onder de naam “commensurate freezing” en veroorzaakt een inflectie in de adsorptie isotherm. Dit effect wordt ook experimenteel waargenomen.

Het adsorptiegedrag van vertakte alkanen in Silicalite is compleet verschillend van lineaire alkanen. Vertakte alkanen zijn preferentieel op de intersecties van Silicalite geadsorbeerd. Dit komt omdat op de intersecties meer ruimte is voor de vertakking. Bij een belading van 4 moleculen per eenheidscel Silicalite zijn alle intersecties bezet en zullen extra moleculen in de kanalen moeten gaan zitten. Aangezien plaatsing in de kanalen energetisch ongunstig is, zullen deze extra moleculen in de rechte en zigzag kanalen moeten worden geduwd. Dit veroorzaakt een inflectie in de isotherm. Deze inflectie is ook experimenteel gemeten voor isobutaan. Alle isothermen blijken goed te beschrijven met een zogenaamd dual-site Langmuir isotherm.

Hoofdstuk 5 beschrijft resultaten van simulaties voor de adsorptie van 50%-50% mengsels van lineaire en vertakte alkanen in Silicalite. Het blijkt dat bij lage drukken zowel lineaire als vertakte moleculen adsorberen. Bij hogere drukken vindt er echter een competitie plaats tussen de lineaire en vertakte alkanen. De lineaire alkanen kunnen overal in het zeoliet adsorberen terwijl de vertakte alkanen met kun vertakking op de intersecties plaats willen nemen. Verder blijkt dat de aanwezigheid van vertakte alkanen de pakking van de lineaire alkanen dusdanig verstoort dat het systeem entropie kan winnen wanneer de vertakte alkanen uit het zeoliet worden verdreven. Dit proces vind plaats voor 50%-50% mengsels van i-C_5-n-C_5, i-C_6-n-C_6 en i-C_7-n-C_7. Deze mengsel isothermen blijken goed te kunnen worden beschreven met een dual-site binaire Langmuir isotherm.

Omdat de Fick diffusiecoëfficiënt rechtstreeks gerelateerd is aan de adsorptie isotherm via de thermodynamische matrix Γ, kan met behulp van de berekende isothermen de diffusie van alkaanmengsels worden beschreven met behulp van de Maxwell-Stefan theorie. Hierbij wordt aangenomen dat de Maxwell-Stefan diffusiecoëfficiënt niet afhangt van de concentratie. Dit levert een mogelijke industriële toepassing op voor de scheiding van lineaire en vertakte alkanen met behulp van een zeolietmembraan.

In hoofdstuk 6 wordt de diffusie van isobutane in Silicalite bestudeerd. Doordat isobutane bij lage druk preferentieel op de intersecties van Silicalite is gesitueerd en er tussen twee intersecties een hoge vrije energie barrière is, zal het verspringen van een isobutaan molecuul naar een naburige intersectie een infrequent proces zijn. Hierdoor is conventionele moleculaire dynamica (MD) niet geschikt om deze hopping rate (en dus ook diffusiecoëfficiënt) uit te rekenen. Om deze hopping rate toch te kunnen uitrekenen is gebruik gemaakt van transition path sampling. In deze techniek wordt een ensemble van MD trajecten gegenereerd die twee intersecties met elkaar verbinden. Hierdoor kan niet alleen de hopping rate worden uitgerekend maar ook kan de zogenaamde transition state worden gelocaliseerd. Voor isobutaan blijkt de berekende diffusiecoëfficiënt veel te laag vergeleken met experimentele resultaten. De verklaring hiervoor moet worden gezocht in het niet meenemen van de flexibiliteit van het zeoliet (vanwege de beperkte hoeveelheid beschikbare rekenkracht) en de nogal grote Lennard-Jones size parameter voor de beschrijving van alkaan-zeoliet interacties. Uit deze simulaties blijkt tevens dat niet alleen de positie maar ook de oriëntatie een belangrijke rol speelt bij de identificatie van transition states.

Curriculum Vitae

The author of this thesis was born on April 3 1974 in Geleen, The Netherlands. After high school (1992), he studied Chemical Engineering at the Eindhoven University of Technology (Eindhoven, The Netherlands [258]), from which he graduated in May 1997. He then moved to the University of Amsterdam, Department of Chemical Engineering (Amsterdam, The Netherlands [259]) to start working on his Ph.D. project with thesis advisors Prof. B. Smit and Prof. R. Krishna.

Published work

- Yamamoto, S., Coumans, W.J., and Vlugt, T.J.H. (1997). "Determining concentration dependent diffusivity in food materials", *Proc. 7th Int. Congress on Engineering and Food (ICEF 7), Brighton, May 1997, editor Ronald Jowitt, part 1*, A164–A167.

- van de Ven-Lucassen, I.M.J.J., Vlugt, T.J.H., van der Zanden, A.J.J., and Kerkhof, P.J.A.M. (1998). "Using molecular dynamics to obtain Maxwell-Stefan diffusion coefficients in liquid systems", *Mol. Phys.*, **94**, 495–503.

- Vlugt, T.J.H., Martin, M.G., Smit, B., Siepmann, J.I., and Krishna, R. (1998). "Improving the efficiency of the CBMC algorithm", *Mol. Phys.*, **94**, 727–733.

- Vlugt, T.J.H., Zhu, W., Kapteijn, F., Moulijn, J.A., Smit, B., and Krishna, R. (1998). "Adsorption of linear and branched alkanes in the zeolite silicalite-1", *J. Am. Chem. Soc.*, **120**, 5599–5600.

- Du, Z., Vlugt, T.J.H., Smit, B., and Manos, G. (1998). "Molecular Simulation of Adsorption of Short Linear Alkanes in Silicalite; Single Components and Binary Mixtures", *AICHE Journal*, **44**, 1756–1764.

- Willemsen, S., Vlugt, T.J.H., Hoefsloot, H.C.J., and Smit, B. (1998). "Combining Dissipative Particle Dynamics and Monte Carlo techniques", *J. Comp. Phys.*, **147**, 507–517.

- Maris, T., Vlugt, T.J.H., and Smit, B. (1998). "Simulation of alkane adsorption in the aluminophosohate molecular sieve $AlPO_4$–5", *J. Phys. Chem. B*, **102**, 7183–7189.

- Krishna, R., Smit, B., and Vlugt, T.J.H. (1998). "Sorption-Induced Diffusion- Selective Separation of Hydrocarbon Isomers using Silicalite", *J. Phys. Chem. A*, **102**, 7727–7730.

- Vlugt, T.J.H., Krishna, R., and Smit, B. (1999). "Molecular Simulations of Adsorption Isotherms for Linear and Branched Alkanes and their Mixtures in Silicalite", *J. Phys. Chem. B*, **103**, 1102–1118.

- Krishna, R., Vlugt, T.J.H., and Smit, B. (1999). "Influence of isotherm inflection on diffusion in Silicalite", *Chem. Eng. Sci.*, **54**, 1751–1757.

- Vlugt, T.J.H., Smit, B., and Krishna, R. (1999). "Adsorption of Linear and Branched Alkanes in Ferrierite: A Computational Study", *Proceedings of the 12th International Zeolite Conference, Treacy, M.M.J., Marcus, B.K., Bisher, M.E., and Higgins, J.B. (eds)*, Materials Research Society, Vol 1, 325-332 Warrendale, PA (1999).

- Maesen, Th.L.M., Schenk, M., Vlugt, T.J.H., de Jonge, J.P., and Smit, B. (1999). "The Shape Selectivity of Paraffin Hydroconversion on TON-, MTT- and AEL-type Sieves", *J. Catal.*, **188**, 403–412.

- Consta, S., Vlugt, T.J.H., Wichers Hoeth, J., Smit, B., and Frenkel, D. (1999). “Recoil Growth Algorithm for Chain Molecules with Continuous Potentials”, *Mol. Phys.*, **97**, 1243–1254.

- Vlugt, T.J.H. (1999). “Efficiency of parallel CBMC simulations”, *Mol. Sim.*, **23**, 63–78.

- van de Ven-Lucassen, I.M.J.J., Otten, A.M.V.J., Vlugt, T.J.H., and Kerkhof, P.J.A.M. (1999), Molecular dynamics simulation of the Maxwell-Stefan diffusion coefficients in Lennard-Jones liquid mixtures, *Mol. Sim.*, **23**, 43–54.

- van de Ven-Lucassen, I.M.J.J., Vlugt, T.J.H., van der Zanden, A.J.J., and Kerkhof, P.J.A.M. (1999), Molecular dynamics simulation of self-diffusion and Maxwell-Stefan diffusion coefficients in liquid mixtures of methanol and water, *Mol. Sim.*, **23**, 79–94.

- Vlugt, T.J.H., and Smit, B. (2000). “Advanced CBMC techniques”, In: *Proceedings of the Workshop “Molecular Dynamics on Parallel Computers”, 8-10 February 1999, Jülich, Germany, Editors: R. Esser, P. Grassberger, J. Grotendorst, M. Lewerenz*, World Scientific, 2000.

Acknowledgements

- First of all, I would like to thank my thesis advisors Prof. B. Smit and Prof. R. Krishna for their contributions to this thesis. I enjoyed working in your groups very much, both from a professional as a personal point of view.

- Second, I would like to thank all people with whom I have collaborated; most of them will have a contribution to this thesis (in random order): my thesis advisors, Daan Frenkel (Recoil Growth), my former undergraduate student and present colleague (soon to be former colleague) Merijn Schenk, Irma van de Ven-Lucassen and everyone else in Eindhoven, Marcus G. Martin and J. Ilja Siepmann (Dual cut-off CBMC), Richard Schumacher and Willy van Well (TUE), Simon Bates, Weidong Zhu and Freek Kapteijn (TEOM experiments, DD3R), Thierry Maris, Sander Willemsen (DPD), Jochem Wichers Hoeth and Stella Consta (Recoil Growth), Theo Maesen, Silvia Lopez Vidal, Christoph Dellago (Transition Path Sampling and the huge amount of CPU time on “max” [103, 104]), JC / Catherine and everyone else at EPCC, Eric Lobenstine and Patrick (Beowulf cluster, U or R), and Zhimei Du. By the way, if somebody who has performed biased Monte Carlo simulations uses the words: “in random order”, you should really worry !

- Third, I would like to thank all present and former colleagues of ITS for the very nice time I had in Amsterdam. Special thanks to those colleagues doing computer simulations (Berend’s group). Thanks to Marieke Kranenburg for a critical reading of this manuscript.

- Finally, I would like to thank my family and friends that are not related to my research for the support during the last few years; especially my parents. I would like to thank my mum for finding a lot of typos in the first version of this manuscript.